DETECTION, LOCALIZATION AND SIZING OF A STRUCTURAL FLAW IN A BEAM BASED ON VIBRATION MEASUREMENTS

A Thesis Submitted in

Partial Fulfillment of the Requirements

for the Degree of

DOCTOR OF PHILOSOPHY

By

M. Karthikeyan

(Roll No. 03610303)

DEPARTMENT OF MECHANICAL ENGINEERING

INDIAN INSTITUTE OF TECHNOLOGY GUWAHATI

APRIL, 2007

CERTIFICATE

It is certified that the work contained in this thesis entitled **Detection, Localization and Sizing of a Structural Flaw in a Beam Based on Vibration Measurements** by **M. Karthikeyan (Roll no. 03610303)** has been carried out under our supervision and that the work has not been submitted elsewhere for a degree.

Dr. Rajiv Tiwari
Professor
Department of Mechanical Engineering
Indian Institute of Technology Guwahati
Guwahati - 781 039, INDIA

Dr. Sudip Talukdar
Professor
Department of Civil Engineering
Indian Institute of Technology Guwahati
Guwahati - 781 039, INDIA

Dedicated to

My Father Late Thiru K. Marappan

ACKNOWLEDGEMENTS

I am deeply indebted to my thesis supervisors Prof. Rajiv Tiwari and Prof. Sudip Talukdar who are an endless source of guidance and encouragement. I thank them for introducing me to such a challengeable area of research and always providing rational, realistic views and thoughts, making it possible for me to freely explore different avenues of research. I specially thank to other members of my doctoral committee, Prof. Uday S. Dixit, Dr. Santosha K. Dwivedy, and Prof. Anjan Dutta for their insightful comments, creative discussions, and guidance.

I would like to express my gratitude to other faculties of the department especially to them whose courses I attended for the course work part. I also thank to Mr. D. J. Bordolai for his cooperation in conducting experiments, Mr. Amal Kalita, for his assistance in CAD laboratory, and all technical staffs of Central Workshop for carrying out the fabrication works well in time. My special thanks goes to all research scholars of the department, all my friends for sharing their healthy moments, and all others in the Institute who helped me directly/indirectly.

I would like to express my deepest gratitude to my family, for their patience and love which enabled me to overcome obstacles and complete my research. Finally, I am always thankful to my guru Shri Vethathiri Maharishi for his divine blessings to my life.

M. Karthikeyan

ABSTRACT

An identification algorithm is developed in order to detect, locate and quantify a structural flaw in a beam based on vibration measurements. The algorithm gives the flaw flexibility and damping as a by-product and has potential to detect no flaw condition. The Timoshenko beam theory is used in modeling of the beam, which represent the Euler-Bernoulli beam as a special case. The finite element method is used for free and forced vibration analysis of the beam with flaw. In the present study, a flaw is modeled through standard five flaw flexibility coefficients, by considering only bending effects i.e., for transverse loading conditions. Rayleigh's damping is assumed to simulate the damping effect of the beam. The algorithm is developed, refined and implemented in four stages; considering various practical difficulties of vibration measurements. The algorithm is iterative in nature and starts with presumption that a flaw is present in the beam. Further iterations are carried out until the estimated and assumed flaw depth ratios (as well as its location) become close enough, up to the desired accuracy. The Tikhonov regularization technique has been adopted for the estimation of bounded flexibility coefficients.

Development of the algorithm is initially attempted using the free-response measurements, such as natural frequencies and corresponding mode shapes. The applicability of the algorithm has been tested through numerical examples and is found to be robust even in the presence of the measurement noise in mode shapes and measurement errors in natural frequencies. The practical difficulty of accurate measurement of mode shapes especially near the flaw is the main limitation of this method. In order to overcome the limitation of the first method, the identification

algorithm is improved by using forced-response measurements. A harmonic force of known amplitude and frequency is used to dynamically excite the beam with the help of an independent exciting unit. The method has been illustrated through numerical examples. The prediction of the flaw location and size are in good agreement even in the presence of the measurement error and noise. However, in this method, measurements of rotational degrees of freedom (DOFs) are required. Accurate measurement of rotational DOFs is still a challenging problem.

A further development of the algorithm has been achieved by implementing novel condensation schemes into the identification algorithm to eliminate all rotational DOFs, so that it can be applied in practical situation. A harmonic force of known amplitude with a sine-sweep frequency is used to dynamically excite the beam, up to few flexible modes, which could be provided with the help of an exciter. With the numerically simulated forced responses, which have the noise contamination and the error in the natural frequency measurements, the estimated flaw parameters (i.e. the flaw location and size) are in good agreement.

Finally, the algorithm has been applied to an experimentally obtained vibration data, in order to justify the practicability of the proposed method. Estimates of flaw parameters are quite close with the actual parameters of the flaw in the test rig.

CONTENTS

List of Figures **xvii - xix**

List of Tables **xxi - xxii**

Nomenclatures **xxiii - xxvii**

Abbreviations **xxix**

Chapter 1 Introduction **1 - 55**

1.1 Introduction....1

1.2 Literature survey....5

1.3 Present work....52

1.4 Organization of the thesis....54

Chapter 2 Flaw Identification Using Free Vibration Techniques **57 - 91**

2.1 Introduction....57

2.2 System modeling.... 58 - 65

2.2.1 Assumptions....58

2.2.2 Flaw model....58

2.2.3 System equations of motion....61

2.2.4 Damped free vibrations....64

2.3 Flaw localization and sizing algorithms.... 65 - 74

2.3.1 Identification algorithm for the flaw sizing....65

2.3.2 Regularization method of estimating flexibility coefficients....70

2.3.3 Flaw localization and sizing procedures....71

2.4 Numerical examples.... 75 - 90

2.4.1 Simply supported beams.... 75 - 84

2.4.1.1 Numerical experiment for modal parameters 75
2.4.1.2 Identification of flaw parameters 78
2.4.2 Cantilever beams ..... 85 - 90
2.4.2.1 Numerical experiment for modal parameters 85
2.4.2.2 Identification of flaw parameters 85
2.5 Conclusions.....91

Chapter 3 Flaw Identification Using the Free and Forced Vibration Techniques 93 - 116

3.1 Introduction.....93
3.2 System modeling..... 94 - 98
3.2.1 Assumptions 94
3.2.2 System equations of motion 94
3.2.3 Forced vibrations.....97
3.3 Flaw localization and sizing algorithms..... 98 - 101
3.3.1 Identification algorithm for the flaw sizing 99
3.3.2 Detection, localization and sizing algorithms 101
3.4 Numerical examples..... 102 - 115
3.4.1 Simply supported beams ..... 103 - 110
3.4.1.1 Numerical experiment for the response generation 103
3.4.1.2 Identification of flaw parameters 107
3.4.2 Cantilever beams ..... 111 - 115
3.4.2.1 Numerical experiment for the response generation 111

3.4.2.2 Identification of flaw parameters 113

3.5 Conclusions.....116

Chapter 4 Flaw Identification Using Forced Vibration Techniques 117 - 146

4.1 Introduction.....117

4.2 System modeling.....118

4.3 Flaw localization and sizing algorithms..... 119 - 128

4.3.1 Implementation of condensation schemes ..... 119 - 125

4.3.1.1 Dynamic condensation 121

4.3.1.2 Hybrid condensation 123

4.3.2 Estimation of flaw flexibility coefficients 125

4.3.3 Detection, localization and sizing algorithms 129

4.4 Numerical examples..... 129 - 144

4.4.1 Simply supported beams ..... 131 - 139

4.4.1.1 Numerical experiment for the response generation 131

4.4.1.2 Identification of flaw parameters 136

4.4.2 Cantilever beams ..... 140 - 144

4.4.2.1 Numerical experiment for the response generation 140

4.4.2.2 Identification of flaw parameters 142

4.5 Conclusions.....145

Chapter 5 Experimental Investigation 147 - 190

5.1 Introduction.....147

5.2 Model descriptions and support conditions 148

5.3 Experimental setup and instrumentations ..... 150 - 167

5.3.1 Experimental setup 151

5.3.2 Excitation unit ..... 152 - 160

5.3.2.1 Attachment to the structure 158

5.3.3 Signal generator and power amplifier ..... 160 - 162

5.3.3.1 Signal generator module 160

5.3.3.2 Power amplifier 162

5.3.4 Force transducer and signal conditioning amplifier ..... 162 - 164

5.3.4.1 Force transducers 162

5.3.4.2 Signal conditioning amplifier 163

5.3.5 Proximity sensors and proximitor unit 164

5.3.6 Pulse analyzer and time capture module ..... 166 - 167

5.3.6.1 Time capture module 167

5.4 Test procedure ..... 168 - 172

5.4.1 Slow-sine sweep testing 168

5.5 Results and discussion ..... 172 - 189

5.5.1 Estimation of damping of the beam 172

5.5.2 Updated finite element model 175

5.5.3 Detection, localization and sizing of the flaw ..... 179 - 189

5.5.3.1 Beam 1 with flaw 179

5.5.3.2 Beam 2 with flaw 186

5.6 Conclusions 190

Chapter 6 Conclusions and Future Works 191 - 198

6.1 Conclusions....191

6.2 Limitations....196

6.3 Scopes for future work....198

Appendix A Flexibility Coefficients of an Open Crack 199 - 200

Appendix B Rayleigh Damping 201

Appendix C Tikhonov's Regularization Method 203 - 204

Appendix D Mass and Stiffness Matrices and Displacement Vectors of the Timoshenko Beam Element 205 - 208

D.1 Elemental mass and stiffness matrices for transverse vibrations....205

D.2 Elemental displacement vector for transverse vibrations....208

Appendix E Dynamic and Hybrid Condensations 209 - 211

E.1 Dynamic condensation....209

E.2 Hybrid condensation....210

Appendix F Intermediate Steps in the Proposed Algorithm 213 - 224

F.1 Intermediate Steps of the Algorithm in Chapter 2....213

F.2 Intermediate Steps of the Algorithm in Chapter 3....217

F.3 Intermediate Steps of the Algorithm in Chapter 4....220

Appendix G Classical Solution of Natural Frequencies For A Simply Supported Timoshenko Beam 225

Bibliography **227 - 245**

List of Publication **247 - 248**

LIST OF FIGURES

2.1 A beam element with flaw subjected to a general loading 59

2.2 A geometry of a beam section with a simple flaw 60

2.3 Finite element discretization of a beam with a flaw 61

2.4 A flow chart for the flaw localization and sizing algorithm ..... 73 - 74

2.5 The first mode shape of beams without and with flaw for simply supported boundary conditions 79

2.6 The second mode shape of beams without and with flaw for simply supported boundary conditions 79

2.7 Variation of first natural frequency ratios versus flaw positions for different flaw depth ratios in the case of the simply supported beam 80

2.8 A procedure for the location of the flaw using the experimental and computational first natural frequencies 81

2.9 The first mode shape of beams without and with flaw for cantilever boundary conditions 86

2.10 The second mode shape of beams without and with flaw for cantilever boundary conditions 86

2.11 Variation of first natural frequency ratios versus flaw positions for different flaw depth ratios for the cantilever beam 88

2.12 A procedure for the location of the flaw using the experimental and computational first natural frequencies for cantilever boundary conditions 88

3.1 Variation of displacement (a) amplitudes and (b) phases with excitation frequencies in vertical plane (without damping) in a simply supported beam 105

3.2 Variation of displacement (a) amplitudes and (b) phases with excitation frequencies in vertical plane (with damping) in a simply supported beam..... 106

3.3 Variation of first natural frequency ratios versus flaw positions for different flaw depth ratios in the case of the simply supported beam..... 108

3.4 Variation of displacement (a) amplitudes and (b) phases with excitation frequencies in vertical plane (with damping) in a cantilevered beam..... 112

3.5 Variation of first natural frequency ratios versus flaw positions for different flaw depth ratios for the cantilever beam 114

4.1 Variation of displacement (a) amplitudes and (b) phases with excitation frequencies in vertical plane (without damping) in a simply supported beam 133

4.2 Variation of displacement (a) amplitudes and (b) phases with excitation frequencies in horizontal plane (without damping) in a simply supported beam 134

4.3 Variation of displacement (a) amplitudes and (b) phases with excitation frequencies in vertical plane (with damping) in a simply supported beam..... 135

4.4 Variation of displacement (a) amplitudes and (b) phases with excitation frequencies in vertical plane (with damping) in a cantilever beam..... 141

5.1 An experimental setup of a beam with flaw 148

5.2 Close view of a beam supported on rolling bearings 149

5.3 Close view of a flaw on the beam 150

5.4 An overall view of the experimental setup and instrumentations 151

5.5 A schematic diagram of the experimental setup with instrumentations 153

5.6 Close view of a vibration exciter assembly 158

5.7 Close view of a stinger and a force transducer 159

5.8 A signal generator module with a power amplifier 161

5.9 Proximity sensors and its mountings 165

5.10 A proximitor with a signal conditioning amplifier 165

5.11 The Pulse analyzer hardware and software 166

5.12 Free vibration of the test beam for the estimation of damping 174

5.13 Comparison of FRFs for beam 1 with flaw 177

5.14 Comparison of FRFs for beam 2 with flaw 178

5.15 Frequency response function in vertical plane for beam 1 with flaw 181

5.16 Frequency response function in horizontal plane for beam 1 with flaw 182

5.17 Frequency response function in vertical plane for beam 2 with flaw 187

5.18 Frequency response function in horizontal plane for beam 2 with flaw 188

LIST OF TABLES

2.1 Parameters used in numerical experiments 76

2.2 Natural frequencies of beams without and with flaw for the simply supported and cantilever boundary conditions 77

2.3 Iteration details for a numerical example 82

2.4 Comparison of theoretical and estimated flaw flexibility coefficients for the simply supported beam 83

2.5 The assumed and estimated flaw parameters for the simply supported beam 84

2.6 Comparison of theoretical and estimated flaw flexibility coefficients cantilever beam 89

2.7 The assumed and estimated flaw parameters for the cantilever beam 90

3.1 Natural frequencies of beams without and with flaw for the simply supported and cantilever boundary conditions 104

3.2 Iteration details for a numerical example 109

3.3 The assumed and estimated flaw parameters for the simply supported beam 110

3.4 The assumed and estimated flaw parameters for the cantilevered beam 115

4.1 Resonance frequencies of beams without and with flaw for the simply supported and cantilever boundary conditions 130

4.2 Iteration details for the numerical example (simply supported end conditions) 137

4.3 The assumed and estimated flaw parameters for the simply supported beam 139

4.4 The assumed and estimated flaw parameters for the cantilever beam 144

5.1 Parameters of the beam for the experimental setup..... 149

5.2 Comparison of the first resonance frequency..... 176

5.3 Iteration details for beam 1 with flaw..... 184

5.4 Actual and estimated flaw parameters for beam 1 with flaw..... 185

5.5 Iteration details for beam 2 with flaw..... 186

5.6 Actual and estimated flaw parameters for beam 2 with flaw..... 189

NOMENCLATURES

a	Flaw depth
a_0 and a_1	Rayleigh damping factors
$\bar{a}$	Flaw depth ratio
$\bar{a}_e$	Equivalent flaw depth ratio
$\bar{a}_{ig}$	Initial guess for the flaw depth ratio
A	Cross sectional area of the beam
b	Half width of the flaw elemental strip
$C_{22}, C_{33}, C_{44}, C_{45}, \text{and } C_{55}$	Flexibility coefficients of the flaw
$[C]^{(e)}$	Total flexibility matrix of the beam with flaw
$[C_o]^{(e)}$	Flexibility matrix of the beam element without flaw
$[C_f]^{(e)}$	Flexibility matrix of the flaw
$\{C^{th}\}$	Vector of theoretical flaw flexibility coefficients
D	Diameter of the circular beam
$[D]$	Assembled damping matrix
$[D_f]^{(e)}$	Element damping matrix of a beam with flaw
$[D_{wf}]^{(e)}$	Element damping matrix of a beam without flaw
$[\bar{D}]$	Reduced assembled damping matrix
E	Young's modulus of the beam material
EI	Flexural rigidity of the beam cross section
$\{f(t)\}^{(e)}$	Element external force vector

$\{F(t)\}$	Assembled external force vector
$\{\bar{F}^d\}$	Condensed force vector with the dynamic condensation scheme
$\{\bar{F}^h\}$	Condensed force vector with the hybrid condensation scheme
G	Modulus of rigidity of the beam material
h	Height of assumed flaw elemental strip
$\{h_0\}$	Mode shapes
j	$\sqrt{-1}$
k_{sc}	Shear correction factor
k_{xx}	Direct stiffness coefficients of the rolling bearing in horizontal plane
k_{yy}	Direct stiffness coefficients of the rolling bearing in vertical plane
$[K]$	Assembled stiffness matrix
$[K_f]^{(e)}$	Element stiffness matrix with flaw
$[K_{wf}]^{(e)}$	Element stiffness matrix with flaw
$[\bar{K}]$	Reduced assembled stiffness matrix
$[\bar{K}^d]$	Condensed stiffness matrix with the dynamic condensation scheme
$[\bar{K}^h]$	Condensed stiffness matrix with the hybrid condensation scheme
l	Beam element length
L	Beam span
$[M]$	Assembled mass matrix

$[M]^{(e)}$	Element mass matrix
$[\bar{M}]$	Reduced assembled mass matrix
$[\bar{M}^d]$	Condensed mass matrix with the dynamic condensation scheme
$[\bar{M}^h]$	Condensed mass matrix with the hybrid condensation scheme
n	Element number
N	Number of beam elements
p	Number of complete cycles of free vibration amplitude
P_1	Axial force
P_2 and P_3	Shearing forces
P_4 and P_5	Bending moments
P_6	Torque
$\{q(t)\}$	Assembled vector of nodal DOFs
$\{q(t)\}^{(e)}$	Beam element vector of nodal DOFs
$\{q_f(t)\}^{(e)}$	Beam (with flaw) element vector of nodal DOFs
$\{\bar{Q}_m\}$	Condensed response vector with the dynamic condensation scheme
$\{\bar{Q}_m^h\}$	Condensed response vector with the hybrid condensation scheme
R	Radius of a beam with the circular cross section
$[T]$	Transformation matrix
$[T^d]$	Dynamic condensation transformation matrix

$[T^h]$	Hybrid condensation transformation matrix
v_1	Linear DOFs at element node 1
v_2	Linear DOFs at element node 2
x	Flaw location
x_p	Amplitude of vibration at p^{th} cycle
$\bar{x}$	Flaw location ratio (= x/L)
X-Y-Z	Rectilinear coordinate system

Greek

$\{\gamma\}$	Regularized solution
δ	Logarithmic decrement
η	Regularization parameter
λ	Damped natural frequency
ν	Poisson's ratio
θ_1	Rotational DOFs at element node 1
θ_2	Rotational DOFs at element node 2
ρ	Mass density of the beam material
ω	Excitation frequency
$\omega_{n_{in}}$	Fundamental natural frequency of a beam without flaw
ω_{nf}	Fundamental natural frequency of a beam with flaw
ζ	Damping ratio

Subscripts

f	With flaw
m	Master DOFs
s	Slave DOFs
wf	Without flaw

Superscripts

d	Dynamic condensation
(*e*)	Element
h	Hybrid condensation
id	Estimated (identified)
th	Theoretical

ABBREVIATIONS

AMB	Active magnetic bearing
CWT	Continuous wavelet transform
dFRF	Directional frequency response function
DOFs	Degrees of freedom
FEM	Finite element method
FFT	Fast Fourier transform
FRF	Frequency response function
IRS	Improved reduction system
SEREP	System equivalent reduction expansion process
SIF	Stress intensity factor
SVD	Singular value decomposition

CHAPTER 1

INTRODUCTION

Detection of damage in a structure or machine parts in earlier stage is very crucial for their safety, operation, and maintenance. The cause, effects, and methodology for the damage detection vary widely depending on the situation; and same are discussed in the present chapter. Historical background of the research works in the area of damage identification and reviews of the earlier works have been presented. Inadequacies of the earlier works have been pointed out. The scope of the present investigation has been stated. An outline of the thesis has been given with brief description on the contents of each chapter.

1.1 Introduction

The present day structures and machineries are designed based on optimizing multi-objective functions involving the maximum strength and life, minimum weight, cost, etc. Hence they are made flexible and allowed to counteract high level of fatigue stresses especially in rotating machineries. This can lead to the development of mechanical flaws in their elements. Extreme operating conditions and variations in working atmosphere between the low and high temperatures would cause to develop thermal flaws in their components. Power supply variations due to unexpected voltage drop would create electrical flaws in electrical machines. Corrosion arising from chemical reactions also causes flaws in chemical handling machine components. The

structural flaws reduce service life, increase maintenance cost and is of concern in various engineering applications. The present study deals with the mechanical flaws occurring in rotating machineries due to stress variations and these are referenced as 'crack'.

In high-speed rotating machinery, high torsional and radial loads, together with a complex pattern of rotor motion, can create severe mechanical stress condition and may eventually lead to the development of rotor crack. Among the various faults like unbalance in the rotor, reciprocating unbalance, misalignment, mechanical looseness, asymmetric shaft, run-out, faults in gears, rolling element bearing faults, rubs, etc., the rotor crack is considered as one of the most serious faults. A crack that forms in a rotor produces a change in geometry that alters the stiffness characteristics of that component. Depending on the size and location of the crack and the loads applied to the system, the adverse effects of this flaw can be either immediate or may take some time before they alter the system's performance severely.

High level of fatigue stresses lead to development of the micro and macro-cracks along with inherent structural flaws such as mechanical stress raisers - sharp keyways, irregular changes in geometries - notches, slits, etc. Apart from these, metallurgical faults like forging flaws, small voids, and matrix porosity may also cause crack initiation. Initiated cracks may propagate due to operating faults, the presence of residual stresses, thermal stress, metallurgical and environmental conditions. In terms of length scales, crack begins at the material level and then under appropriate loading, it progresses to component and system with level of damage at various rates. In terms of time scales, crack can accumulate incrementally over long

periods of time such as that associated with the fatigue or corrosion damage accumulation. Failure occurs very rapidly once the crack(s) reaches a critical size. These cracks can be classified as the transverse, longitudinal, slant, breathing, gaping and surface cracks, based on their geometries.

The presence of such cracks (or flaws) may lead to gradual or sudden failure. These failures may lead to plant shutdown, associated various losses, and some times accident. A cracked rotor must be replaced or repaired to prevent equipment from possible damages and losses. Hence, the detection and the diagnostic (i.e., its localization and sizing) of such flaws is required to take corrective action well before they grow critical. If a crack is detected and localized at an early stage, the rotor may be repaired at a relatively low cost and within a short period of time. Various non-destructive testing methods such as the liquid penetrant testing, radiographic testing, ultrasonic inspection, visual and optical testing, electromagnetic testing, eddy-current testing, acoustic emission testing, infrared and thermal testing, laser testing etc., can be used for the detection of flaws (Shull, 2002). However these methods usually require that the system under investigation be taken out of service for inspection at pre-set time intervals. The inspection procedure can be very expensive and time consuming, especially when it involves components at inaccessible locations. This has led to the development and continued research on vibration based methods that examine changes in the free and forced vibration characteristics of complex structures. These methods can be applied to in-service structures, reducing maintenance costs, ensuring safety and improving system performance. With the development of non-contact sensors, the method finds useful application in case of moving parts of the machine.

Available vibration based methods can be grouped as the signal based, model based, modal testing, and methods which use non-traditional tools like neural networks, fuzzy logic, borescope (optical device) inspection, and sophisticated signal processing techniques, e.g. the wavelet and Wigner-Ville transforms, etc. Doebling et al. (1998) classified the vibration based methods into various categories. The methods are broadly based on the linear and nonlinear effects of damage of structures. Another classification system given by Rytter (1993) for damage-identification methods defined four levels of damage identification, as follows:

- Level 1: Determination of the presence of damage in the structure
- Level 2: Level 1 plus determination of the geometric location of the damage
- Level 3: Level 2 plus quantification of the severity of the damage
- Level 4: Level 3 plus prediction of the remaining service life of the structure

Vibration-based damage identification methods that do not make use of some structural model primarily provide Level 1 and Level 2 damage identification. When vibration-based methods were coupled with a structural model, Level 3 damage identification could be obtained in some cases. Level 4 prediction was generally associated with the fields of fracture mechanics, fatigue-life analysis, or structural design assessment.

According to the above classification, present work has been carried out up to Level 3 i.e., detection, localization and sizing of a flaw based on the both numerical and experimental vibration measurements.

1.2 Literature Survey

There are many kinds of damage detection methods available including the nondestructive testing. Visual inspection by experienced team of engineers may often produce valuable information on the existing state of structures and future assessment of load carrying capacity. However, if the cracks or flaws remain inside the structure, visual inspection cannot reveal the actual state of the structure.

The shortcomings of visual inspection methods have been overcome by means of non-destructive evaluation (NDE). The basic principle of NDE is to determine the quality or integrity of an item nondestructively. The advantages of non-destructive testing (NDT) include i) testing can be performed on the actual structure rather than on a companion (representative) sample of it, ii) tests can be conducted at many locations, and iii) tests can be conducted at multiple times. However, most of the NDT techniques are able to yield qualitative information without giving precise location and extent of damage. Several NDTs (Shull, 2002), that are commonly applied for assessment of structural health are – i) Liquid penetrant test, ii) Ultrasound pulse velocity test, iii) Magnetic particle testing, iv) Eddy current testing, v) Acoustic emission, and vi) Radiology technique . Nevertheless, there are other NDTs and the existing ones are continuously in the process of upgradation to have more reliable information. A brief description of some common NDTs are given below:

Liquid penetrant testing

Penetrant testing (PT) is a rapid, simple, inexpensive, and sensitive NDT method. It allows the inspection of a large variety of materials, component parts, and

systems for discontinuities that are open to the surface; these discontinuities may be inherent in the original materials, result from some fabrication process, or develop from usage and/or attack by the environment. PT's greatest advantage is its wide applicability. Even some porous materials can be inspected using a special penetrant system. The major disadvantage of PT is that it can detect only defects that are open to the surface of a specimen.

Ultrasound technique

The propagation of ultrasonic waves through the structure and its interaction with the medium can reveal valuable information about the state of the structure. The velocity of wave propagation can be expressed as a function of material density and elastic constant. In ultrasonic tests, two transducers one 'transmitter' and other 'receiver' are used. The transmitter introduces the wave pulse into the specimen whereas the receiver senses the arrival of wave by measuring the time taken by the pulses. Abnormal low velocity through the known medium gives indication of damage inside. However, this method fails to exactly locate and quantify damage. The test is very simple with portable instrument and gives an overall assessment of structure.

Magnetic particle inspection

Magnetic particle inspection (MPI) is one of the most economical and simple NDE methods to use. It magnetizes the sample, and simultaneously flows (i.e., the magnetic field) finely divided ferromagnetic particles over the surface. Any defect in the material will affect the magnetic field in the sample, and thus can attract magnetic particles to the edges of the defects. This means that magnetic particles can outline

surface and near surface defects, and therefore can be used as an indicator for such defects.

It is generally the best and most reliable method for finding surface cracks, especially very fine and shallow ones. The greatest disadvantages of MPI are that it can be used only on ferromagnetic parts and that it can detect only surface and near-surface cracks.

Eddy current method

Eddy current (EC) methods interrogate conductive materials through the magnetic induction. The probe itself is similar to an AC transformer. EC readily inspects metals and is non-contacting. Unlike penetrants and most magnetic-particle methods, EC does not require surface preparation. EC is the low cost system, portable and one of the few methods used for high-temperature applications.

EC inspection suffers from a number of drawbacks. The most troublesome is that the interrogated material must be a conductor. The EC probe responds not only to the intended material characteristic but also to unintended signals such as liftoff and to all of the unwanted material properties related to conductivity and/or magnetic permeability. Separating the response signals, or reducing unwanted signals, requires significant operator training and/or sophisticated algorithms.

Acoustic emission monitoring

Among the various NDE techniques, acoustic emission (AE) monitoring is based on the simplest physical concepts, but is one of the most difficult techniques to

practically implement. That is the release of transient elastic waves produced by a rapid redistribution of stress in a material. AE testing is further complicated in comparison to the ultrasonic testing by the fact that the characteristics of the 'input' or emitted signal are relatively unknown. The emitted acoustic signal is dependent on the characteristics of the source, which is located inside the material. Different AE sources may produce vastly different AE waveforms.

Radiology

Radiography is one of the few NDE methods that can examine the interior of the object and the only NDE method that works on all materials. Analyzing and interpreting the images requires skill and experience but the casual user of radiation imaging services can easily recognize the item being imaged (scanned) and can often recognize discontinuities without expert interpretation. Despite their advantages, radiation methods create serious safety concern. Not only the radiation is dangerous, but the high voltage needed to generate most X-rays can be dangerous as well as the difficulty in using heavy shielding materials. Also, radiography is limited in utility for detecting cracks. Finally X-ray machines, especially computer tomography systems, are very expensive and time consuming and require the use of highly trained safety conscious persons.

Apart from these methods, many other methods are also available such as the active thermography, microwave, optical methods, etc. All NDE methods require a certain level of physical competence, such as the visual acuity and the manual ability. Even though a qualified inspector must possess these competencies, they can be diminished or subverted by fatigue, unreliable vision, adaptation to light and general

distractions from the inspections. Nonetheless many external pressures, such as production schedules, costs fatigue, and temporary personal issues; can subvert an operator's integrity. The working environment also plays a significant role in both the sensitivity and reliability of traditional NDE methods. Vibration based damage detection method is one of the non-destructive evaluation techniques that find growing importance in the health monitoring of structure and other machine components. Degradation of the structure in the reduction of stiffness can be easily recognized by measuring the parameters associated with free vibration. Because of its immense practical significance, various studies based on theoretical modeling and experimentations have been initiated by number of researches with varying degree of success.

Flaw models

The presence of transverse flaw in a structural member introduces local flexibility, which can be described by a local flexibility matrix, and the dimension of the flexibility matrix depends on number of DOFs considered. There is plenty of literature that deal with the flaw (or the crack) modeling using the finite element and continuous beam theories.

Dimarogonas and Massouros (1981) evaluated the local flexibility of a shaft in torsion due to a crack from analytical expressions relating the strain energy release function (and consequently the stress intensity factor) to the crack depth.

Dimarogonas and Paipetis (1983) introduced a matrix for beams of the rectangular cross section with the transverse surface crack. They showed a beam with a transverse crack, in general, could be modeled in the vicinity of the crack by way of a local flexibility (compliance) matrix, connecting the longitudinal, bending, and shear forces, and corresponding displacements. If torsion is also added, a 6×6 compliance matrix may result and it has off-diagonal terms that indicate coupling of the respective forces and displacements, and therefore the coupling of respective motions. This matrix is a diagonal matrix in absence of the crack.

Papadopoulous and Dimarogonas (1987) investigated the coupling of the longitudinal and bending vibrations of a rotating shaft, due to an open transverse surface crack. They assumed the open crack leads to a system with behaviour similar to that of a rotor with dissimilar moments of inertia along two perpendicular directions and represented the local flexibility due to the presence of the crack by a matrix of size 6×6 for six DOFs in the shaft crack element. This matrix has off diagonal terms, which cause the coupling along the bending in two transverse directions and the extension along the longitudinal direction, which gives the stiffness matrix of the size of 3×3 with coupling terms. The undamped free and forced vibrations were considered. The existence of the coupling due to the crack was used for the crack identification in rotating shafts together with the sub-critical resonance.

Gounaris and Dimarogonas (1988) used the FEM to model the structure and developed a finite element for the cracked prismatic beam. The element was used to evaluate the dynamic response of a cracked cantilever beam to the harmonic force

excitation. They showed that resonant frequencies and vibration amplitudes were considerably affected by the existence of moderate crack.

Papadopoulous and Dimarogonas (1988) described the coupling of the bending and the longitudinal vibration of stationary cracked shaft with an open crack. A 2×2 local flexibility matrix with coupling terms modeled the crack. The elements of this matrix were obtained analytically. The free vibration and the influence of the crack on the vibrational behaviour of the shaft were studied. The applicability of the method as a crack identification tool was demonstrated.

Qian et al. (1990) derived the elemental stiffness matrix of a beam with a crack from the integration of stress intensity factors and then established the finite element model of a cracked beam.

Shen and Pierre (1990) presented an approximate Galerkin solution to the one-dimensional cracked beam theory developed by Christides and Barr (1984) for the free transverse motion of beams with pairs of symmetric cracks. To validate the theoretical results, a two dimensional finite element approach was developed, which also allowed determining the parameter that controls the stress concentration profile near the crack tip in the theoretical formulation without requiring the use of experimental results.

Lee et al. (1992) proposed a switching crack model with two different stiffness states, depending upon whether the crack is open or close. The necessary conditions

for the crack opening and closing were analytically derived from the simple rotor with the switching crack.

Chondros et al. (1997) developed a consistent continuous cracked bar vibration theory. The stress and displacement fields about the crack were used to modify the stress and displacement fields throughout the bar. The reduction to one spatial dimension was achieved by integrating the stress and displacement fields throughout the bar cross-sections. The resulting linear differential equation with variable coefficients had the modified displacement field due to the crack imbedded in it.

Chondros et al. (1998) developed a continuous cracked beam vibration theory for the lateral vibration of cracked Euler-Bernoulli beams with single edge or double edge open cracks. They used the Hu-Washizu-Barr (1955, 1966) variational formulation to develop the differential equation and boundary conditions of the cracked beam as a one-dimensional continuum.

Sukumar et al. (2000) described a FEM based three-dimensional crack modeling. A discontinuous function and a two-dimensional asymptotic crack tip displacement field were added to the finite element approximation to account for the crack using the notion of partition of unity. They discussed computational geometry issues associated with the representation of the crack and presented stress intensity factors for planar three-dimensional cracks.

Carneiro and Inman (2002) proposed a continuous mathematical model of a cracked Timoshenko beam. The Hu-Washizu-Barr variational (1955, 1966) principle was used for the systematic derivation of continuous models and the stress concentration effects was represented by an exponential disturbance function acting both on the axial and shear stresses.

Chondros (2005) developed a variational formulation for the torsional vibration of a cylindrical shaft with a circumferential crack. The Hu-Washizu-Barr (1955, 1966) variational formulation was used to develop the differential equation and boundary conditions of the cracked rod. He reported independent evaluations of crack identification methods in rotating shafts and compared with methods using the continuous crack flexibility theory.

Di and Law (2006) provided different types of damage models of a frame element, whose elemental matrices were decomposed into their eigen value and eigen vector matrices. These eigen-parameters were included in a flexibility-based and sensitivity-based model-updating algorithm for the condition assessment of a plane frame structure.

Lei et al. (2007) proposed a finite element model for vibration analysis of a crankshaft with a slant crack in the crankpin and investigated the influence of the crack depth on the transient response of a cracked crankshaft.

In the flaw models developed by past researchers, the flexibility due to flaw was given by a 6×6 flaw flexibility matrix, which consists of the flexibility

coefficients. The flexibility coefficients were derived by using the linear fracture mechanics approach. The couplings between different plane motions such as torsion, longitudinal and bending were taken into consideration. The elemental stiffness matrix of a crack beam, a switching crack model, damage models of a frame element, and FE model with a slant crack were also discussed. In addition to these flaw models, the continuous cracked beam/bar vibration theories using variational formulations were derived. Longitudinal, bending and torsional vibrations of the beam/bar were considered.

Free and forced vibration analysis of the cracked beam/rotor

The development of flawed models and theories enhanced the study of vibration based techniques for the damage detection using the FEM. Both the free vibration analysis and forced vibration response studies have been carried out by several investigators. The behaviour of cracked rotor could be analyzed if the crack model parameters are known. The presence of a transverse crack in a structural member introduces local flexibility, which can be mathematically modeled by a local flexibility matrix. By using the linear fracture mechanics approach theoretically coefficients of the flexibility matrix are computed based on available expressions of the stress intensity factor and associated expressions of the strain energy density function. The works based on the free and forced vibration analyses of cracked beams are described subsequently.

Liebowitz et al. (1967, 1968), and Okamura (1969) studied the effects of the reduced rigidity on the load carrying capacity, deflection, and fracture load of a

slender column with a single edge crack based on the column theory together with the relationship between the compliance and the stress intensity factor of a cracked beam. This study indicated that the bending and compression stress intensity factors of the same mode could be superpositioned.

Mayes and Devies (1984) used the FEM to describe the flexural vibrational behaviour of a rotor with a transverse crack. They stipulated that the self-weight bending dominates on the crack opening and closing. The application of the method to some turbo generators was discussed.

Changhe et al. (1989) presented an analytical method for describing the crack breathing and obtained the shaft local stiffness change. A generalized nonlinear formulation using the FEM, which could be used for both the horizontal and vertical cracked shafts, was derived.

Rajab and Sabeeh (1991) investigated the vibration characteristics of a cracked Timoshenko shaft. Analytical expressions were obtained by modeling the crack as the bending and shear compliances of equivalent incremental strain energy by using the *J*-integral concept form fracture mechanics. It was shown that the knowledge of changes in the first three natural frequencies relative to the uncracked shaft was sufficient to estimate the crack depth and the crack location in the shaft. Each additional crack in the shaft requires the knowledge of the changes in the next two higher natural frequencies.

Papadopoulos and Dimarogonas (1993) used a 6×6 flexibility matrix, including off diagonal terms, to simulate a cracked shaft and study its dynamic behaviour. To examine couplings of various modes, resulting from 6×6 flexibility matrix, they studied the coupling between the bending and the torsion.

Huang et al. (1993) investigated the dynamic response of rotating shaft containing a transverse crack. The local flexibility due to the crack was first evaluated from the theory of fracture mechanics. The steady state response and the stability criteria were then obtained, and the effects of the crack depth, crack location, and the rotational speed were discussed. The results showed that the increase of the crack depth magnified the response amplitude.

Abraham et al. (1994) studied the stress concentration near the crack that induces a local flexibility and modifies the dynamic behaviour of cracked structures. They proved analytically that some of the double integrals commonly encountered in crack modeling diverge when the depth of crack equals the radius of the circular section of the shaft.

Sekhar and Prasad (1997) analyzed flexural vibrations of a rotor-bearing system by including a shaft having a slant crack that resulted from the fatigue of the shaft due to the torsional moment. At an interval, the frequency corresponding to the torsional frequency, the presence of sub-harmonic frequency components in the frequency spectrum of the steady state response was used for the crack detection.

Tsai and Wang (1997) presented the free vibrational analysis of multi- step and multi-cracked rotor having cracks of the opening mode of fracture. The transfer matrix method was used in the modeling of the rotor along with the Timoshenko beam theory.

Yokoyama and Chen (1998) investigated the vibration characteristics of a uniform Euler-Bernoulli beam with a single edge crack using a modified line-spring model. Natural frequencies and corresponding mode shapes were determined for uniform beams having edge cracks of different depths at different positions. It was also shown that the abrupt change in higher mode shapes of the vibration, for the cracked beam, made it possible to predict and monitor the crack location in the beam.

Kisa et al. (1998) analyzed the vibration characteristics of a cracked Timoshenko beam for general loading conditions. The study integrated the FEM and the component mode synthesis by dividing the beam into two components related by a flexibility matrix, which incorporates the interaction forces.

Shifrin and Ruotolo (1999) presented a method for evaluating natural frequencies of a beam with an arbitrary number of cracks. This method was based on the use of massless rotational springs in order to represent the cracks. It leads to a system of (n+2) linear equations for a beam with n cracks.

Meng and Gasch (2000) investigated the stability and its degree of a flexible cracked rotor supported on different kinds of journal bearings. Influences of the crack stiffness ratio, the fixed Sommerfeld number (which is the design parameter), the

gravity parameter (which represents the elasticity of the shaft), and the mass ratio were analyzed. They found that the position of the crack ridge and unstable zones depended on the speed, the stiffness change and mass ratios.

Murphy and Zhang (2000) investigated the vibration and stability characteristics of a cracked beam, which was modeled using the Hamilton's principle and elementary fracture mechanics.

Khiem and Lien (2001) developed a procedure based on the transfer matrix method for the natural frequency analysis of a multiple cracked beam based on the rotational spring model of the crack. Using this method the frequency equation for a beam with an arbitrary number of cracks was obtained by determinant calculation of 4×4 dimension matrix.

Saavedra and Cuitino (2001) presented a theoretical and experimental dynamic behavior of multi-beams systems containing a transverse crack. Nonlinear equations of motion were solved using a numerical integration method (Hilbert et al., 1977). It was shown that the crack caused noticeable changes in the frequency spectrum of the steady-state vibration, adding peaks at multiples or harmonics of the forcing frequency, especially the even harmonics. The limitation of the method was the difficulty of determining mode shapes especially when the crack has small effects for the moderate crack size.

Zhou et al. (2001) analyzed the nonlinear dynamic response of a Jeffcott rotor with small cracks, both theoretically and numerically. An acceleration scheme was suggested to reduce shocks to the rotor and diagnose the existence of cracks.

Zheng and Fan (2001) presented a method for computing natural frequencies of a Timoshenko beam with an arbitrary number of transverse open cracks with the use of modified Fourier series, which could approach a function with internal geometrical discontinuities.

Bamnios et al. (2002) investigated the effect of a transverse surface crack on the mechanical impedance of cracked beams under different boundary conditions, both analytically and experimentally. It was shown that, far from the expected changes in natural frequencies, the mechanical impedance changed substantially; and based on impedance measurements a prediction scheme for the crack location was proposed.

Fernandez-saez and Navarro (2002) presented an analytical approach to calculate the fundamental frequency of the cracked Euler-Bernoulli beams in bending vibrations. The flexibility influence functions (which was defined as the vertical displacement of a considered point due to a unit load applied at the point) were constructed and were used to solve an eigen value problem formulated in the integral form and the influence of the crack was represented by an elastic rotational spring connecting the two segments of the beam at the cracked section.

Pu et al. (2002) obtained a stable response of a cracked rotor-bearing system, when the condition of the weight control was available and the breathing of the crack was simulated by hinge mechanism with a flexible single-degree-of-freedom rotor supported on flexible bearings. The crack was transformed into an external disturbance. Bearing forces, interactions between a lumped-mass disc, and flexible shaft was represented by a series of trigonometric functions.

Dado and Abuzeid (2003) presented a modeling and analysis algorithm for cracked Euler–Bernoulli beams by considering the coupling between the bending and axial modes of the free vibration, under the effect of added mass and rotary inertia at the free end. It was shown that the coupling between the transverse and axial vibrations were weak for the first two modes for moderate values of the crack depth ratio and high crack depth ratios appear to increase the coupling effects.

Zhua et al. (2003) theoretically analyzed dynamic characteristics of a cracked rotor with an active magnetic bearing (AMB); and discussed effects of using optimal controller parameters on the dynamic characteristics of the cracked rotor; and the effect of a crack on the stability of the active control system. It was also shown that the dynamic characteristics of the cracked rotor with AMBs were clearly more complex than that of the traditional cracked rotor system.

Darpe et al. (2003a) analyzed the coupling of the lateral and longitudinal vibrations due to the presence of transverse surface crack in a rotor for the non-rotating and rotating conditions. The steady state unbalance response of a cracked rotor with a single centrally situated crack subjected to periodic axial impulses was

investigated experimentally. Darpe et al. (2003b) studied a simple Jeffcott rotor with two transverse surface cracks and the effect of the interaction of two cracks on the breathing behavior and on the unbalance response of the rotor. They noticed the significant changes in the dynamic response of the rotor when the angular orientation of one crack relative to the other was varied.

Ruotolo and Surace (2004) extended the method, proposed by Shifrin and Ruotolo (1999), for the calculation of longitudinal natural frequencies of a vibrating isotropic bar with an arbitrary finite number of symmetric transverse open cracks. The obtained natural frequencies were compared with that of the transfer matrix and FEM.

Darpe et al. (2004) studied the coupling between longitudinal, lateral and torsional vibrations together for a rotating cracked shaft with a response-dependent non-linear breathing crack model. Crack signatures were obtained by using external excitations and the excitation in one mode led to an interaction between all the modes, as the couplings were accounted. The co-existence of frequencies of other modes in the frequency spectra of a particular mode and the presence of sum and difference of frequencies around the excitation frequencies and its harmonics were used as the indicators for crack diagnosis.

Kishen and Kumar (2004) presented a finite element analysis of cracked beam-columns subjected to the axial and lateral loads. They observed that the presence of crack decreased the critical load of columns and this decrease was small for short cracks and long columns. It had no effect for columns with slenderness ratios

180 and above and makes the relation between the lateral load and the lateral deflection bi-linear in a beam-column subjected to the axial compressive load.

Yang and Suh (2004) presented a method called the empirical mode decomposition as an alternative to the Fourier-based methodologies for resolving the true physical features characteristic of a dynamic motion experiencing non-linearity and undergoing bifurcation. They demonstrated the developed method using a rotor model to display various stages of dynamic non-linear responses induced by the breathing of a transverse surface crack on the rotor.

Zheng and Kessissoglou (2004) obtained natural frequencies and mode shapes of a cracked beam using the FEM. An overall additional flexibility matrix, instead of the local additional flexibility matrix, was added to the flexibility matrix of the corresponding intact beam element to obtain the total flexibility matrix, and natural frequencies were obtained. A shape interpolation function was developed to compute the vibrational modes of a cracked beam.

Douka et al. (2004) investigated analytically and experimentally the influence of two transverse open cracks on anti-resonances of a cantilever beam. Cracks were modeled by an appropriate equivalent springs connecting segments of the beam. It was shown that the changes of natural frequencies and anti-resonances of the cracked beam followed definite trends depending upon the location of cracks and it provided the required information for the crack localization and their depths. The scheme was validated by using experiments on plexiglas beams.

Binici (2005) proposed a procedure to obtain eigen frequencies and mode shapes of beams containing multiple cracks and subjected to the axial force. Cracks were modeled as rotational springs, and the method was also used to predict the critical load of damaged structures based on eigen frequency measurements.

Sinou and Lees (2005) analyzed the influence of transverse cracks in a rotating shaft and addressed the issues of the changes in modal properties and the influence of the crack breathing on the dynamic response during the operation. They also investigated the evolution of the orbit of a cracked rotor near half of the first resonance frequency.

Zhou et al. (2005) investigated experimentally the nonlinear dynamic characteristics of rotor systems containing a single transverse fatigue crack. They observed that the appearance of a crack could reduce the first-order critical speed, when passing through the critical or one-half of the critical speed. While in the supercritical speed range the behavior of the shaft was similar to the effect of an increase in eccentricity.

Green and Casey (2005) analyzed theoretically the global and local asymmetry crack models to identify characteristics of the system response of a rotating shaft having a transverse crack. A 2× harmonic component of the system response was shown to be the primary response characteristic resulting from the introduction of a crack.

Wang et al. (2005) investigated the coupled bending and torsional vibrations of a fiber-reinforced composite cantilever with an edge surface crack. The crack was modeled with a local flexibility matrix such that the cantilever beam was replaced with two intact beams with the crack as the additional boundary condition. They found that for the unidirectional fiber-reinforced composite the changes in natural frequencies and corresponding mode shapes depend on not only the crack location and the depth, but also the material properties (fiber orientation, fiber volume fraction, etc.).

Kisa and Gurel (2006) presented a numerical approach to implement the free vibration analysis of the circular cross sectional beams containing multiple non-propagating open cracks. The component mode synthesis technique was combined with the FEM and a non-linear problem separated into linear subsystems. The effects of location and depth of cracks on natural frequencies and mode shapes of beams were numerically investigated.

Mei et al. (2006) studied the free and forced vibration analysis of an axially loaded cracked Timoshenko beam from wave standpoint, in which vibrations were described in terms of the wave propagation, transmission and reflection in waveguides. The transmission and reflection matrices for waves incident upon various discontinuities on the beam were derived.

Yoon and Son (2006) studied the effect of the open crack and a moving mass on the dynamic behavior of a simply supported pipe conveying fluid. The equation of motion was derived by using the Lagrange's equation and was analyzed by the

numerical method. The crack was modeled as a rotational spring. The influences of the crack severity and its position, the moving mass and its velocity, the velocity of the fluid; and the coupling of these factors on the vibration mode, frequency ratio, and mid-span displacement of the simply supported pipe were depicted.

Le (2006) gave insight into properties of the Wigner-Ville time-frequency power spectral analysis (Zou and Chen, 2004) and suggested a time-frequency power spectral tools to study cracks in rotors. He showed from simulation results that the Choi–Williams and hyperbolic distributions (Zou and Chen, 2004) could be effectively used for the crack detection in rotors.

Darpe et al. (2006) formulated equations of motion of the rotor with a transverse surface crack with a bow, and analyzed the steady state and the transient response of the rotor. They assessed the effect of the residual bow on the stiffness characteristic of the rotating cracked shaft and observed that the usual level of bow might not significantly influence the stiffness variation and the nonlinear nature of crack response was not significantly altered.

Mani et al. (2006) presented a health-monitoring scheme for rotor dynamic systems having breathing cracks (cracks that open when the affected part of the material is subjected to tensile stresses and close when the stress is reversed) in the shaft, which was supported by conventional bearings; and an AMB was used in a mid-shaft or outboard location as an actuator. At the resonance condition the spectral analysis of the damaged shaft vibration response contained a component at the critical frequency in addition to a component at the excitation frequency. The amplitude of

this component at the critical frequency was proportional to the magnitude of the time-dependent stiffness introduced by the breathing crack. This relationship was used to detect and quantify the presence of breathing cracks in rotating shafts subject to harmonic forcing applied by AMBs.

Benfratello et al. (2006) investigated numerically and experimentally the capability of the non-Gaussianity measures to detect the crack presence and its position. The Monte-Carlo method was applied to evaluate in time domain the higher order statistics of a cantilever beam modeled by the FEM. The skewness coefficient of the rotational DOFs was used for the identification of the nonlinear behaviour of the cracked beam.

Duffour et al. (2006) investigated sensitivity of the vibro-modulation technique on a set of mild steel beams with cracks of different sizes and shapes. They showed that the technique was sensitive to the initial state of opening and closing of the crack and to the setup due to the modulating effects of contacts between specimens and supports.

Bachschmid et al. (2006) studied the bending and torsion dynamic behaviors of a cracked shaft of a typical vertical axis centrifugal reactor-cooling pump of a nuclear power plant, by considering the effect of a breathing crack located close to the impeller. Differences in behaviour of an always-open crack with respect to the breathing crack were observed, and it was shown that measurements of torsional vibrations could improve the possibility of detecting cracks in this type of machines.

Szolc et al. (2006) performed the fatigue analysis and the life estimation of cracked rotor-shafts by means of the one- and three-dimensional dynamical models. It was shown from the computation results that normal stresses in the shaft cracked zone due to the bending and axial dynamic loads play a predominant role for the material fatigue life, whereas tangential stresses caused by torsional vibrations are of the secondary importance and a transverse crack could exist in the steel shaft in one position with respect to the bearing support or propagate very quickly in another position.

Bachschmid and Tanzi (2006) analysed the dynamical behaviour of rotors having deep transverse cracks with linear and nonlinear approaches, and evaluated the magnitude of the non-linear effects and the validity of the linear approach.

Loya et al. (2006) provided solutions for natural frequencies for bending vibrations of cracked Timoshenko beams. The beam was modeled as two segments connected by two massless springs (one extensional and another rotational) and differential equations were solved individually for each segment at the cracked section.

Chasalevris and Papadopoulos (2006b) studied the free bending vibration of a rotating shaft having a uniform circular cross-section with a transverse crack, and presented results of the change of the local compliance matrix. It was shown that change in the total stiffness in transverse directions depended on the change in the crack local compliance. The rotation of the transverse crack and the coupling of

vibrations in the vertical and horizontal planes affected the response and amplified higher harmonics of vibration due to the crack.

Kou and Burdekin (2006) carried out the finite element analysis to calculate the stress intensity factors (SIF) for circumferential cracks in tubular members under the axial tension. SIF were obtained for a wide range of deep surface cracks, partly through-wall cracks and fully through-wall cracks and used in the fatigue crack growth calculations.

Sinou and Lees (2007) demonstrated that the introduction of a deep breathing crack induced the 2× and 3× harmonic components of the primary response characteristic resulting from the changes in the non-linear dynamical behaviour of the rotor system.

The analyses of the beam/rotor with flaw using the free and forced vibrations are available from the literature as early as 1960s. The FEM was used in most of the subsequent works. The transfer matrix, component mode synthesis, and integration methods were also used in some of them. The massless rotational springs was assumed to represent the cracks, apart from the available flaw model. The influences of crack on rotor supported on different kinds of journal bearings and AMBs were discussed.

Analysis of various behaviour of beam/rotor with flaw forms basis and helps to proceed with the next stage of damage diagnostics i.e., the development of flaw

detection and identification methods. Reviews on the flaw detection and identification are presented subsequently.

Previous review works on the flaw detection and identification

The available review works are grouped pertaining to the field of dynamics of cracked rotor, stability behaviour of rotating shafts, dynamics response of cracked rotors/structures, natural frequencies changes based methods, modal properties of damaged structures and recent developments damage diagnosis area.

Wauer (1990) presented a review of literature in the field of dynamics of cracked rotors, including the modeling of the cracked part of structures and determination of different detection procedures to diagnose fracture damages. The review formed a basis for analyzing dynamics of cracked beams and columns (i.e., non-rotating, cracked structural elements which is relevant to the cracked rotor problems).

Gasch (1993) provided a survey of the stability behaviour of a rotating shaft with a crack and its forced vibrations due to unbalances. He established some possibilities for early crack detection using the Laval (or Jeffcott) rotor (a single disc on an elastic shaft) with a simple crack model.

Dimarogonas (1996) reviewed works, which were published from 1971 to 1994 on the dynamic response of rotors and other structures with cracks. There were three basic methods for dealing with the problem of crack modeling, such as the

equivalent reduced section, the local flexibility from fracture mechanics theory, and the cracked continuous bar or beam. The methods for the crack identification in rotating shafts and beams were the recognition of the vibration coupling due to cracks; the parametric vibration, and the bilinear and nonlinear effects; experimental investigations; expert systems utilizing the predicate logic, or the fuzzy logic; and artificial neural networks. Some of the future works were suggested such as development of a rigorous cracked beam vibration theory, further work on the effect of the closing cracks and propagating cracks, analytical formulation of the damping change due to the crack, and thermal effects due to cracks.

Salawu (1997) reviewed the vibration based condition assessment procedures of structures by the use of natural frequencies as a diagnostic parameter. The relationship between frequency changes and structural damages were discussed. Various methods proposed for detecting damages using natural frequencies were reviewed. Factors (e.g., choice of measuring points, effects of ambient conditions on dynamic responses, and consistency and reliability of testing procedures, etc.) that could limit successful application of the vibration monitoring for the damage detection and the structural assessment were also discussed.

Doebling et al. (1998) provided an overview of methods to detect, locate, and characterize damages in the structural and mechanical systems by examining changes in measured vibration responses. The scope of this paper was limited to methods that use changes in modal properties (i.e., modal frequencies, modal damping ratios, and mode shapes) to infer changes in mechanical properties. They suggested the issues for further developments of the existing damage detection methods such as the ability to

account for the effects of nonlinear structural response, constraints on the number and location of measurement sensors, level of sensitivity that modal parameters have to small flaws in a structure and the ability to discriminate between changes in the modal properties resulting from damage and those changes resulting from variations in the measurements. It was also opined that the literature in general needs to be more focused on the specific applications, and research should be focused more on testing of real structures in their operating environment, rather than laboratory tests of representative structures.

Sabnavis et al. (2004) reviewed literature published since 1990 with some classical works on the crack detection and estimation of severity of the crack in shafts. The review was based on three categories namely vibration-based methods, modal testing, and non-traditional methods. They also discussed the types and causes of rotor cracks and fundamentals of the crack propagation.

Alvandi and Cremona (2006) reviewed vibration-based damage identification techniques based on measured modal parameters and used them for the structural damage evaluation. It was concluded that among the available techniques, the strain energy method presented the best stability even with noisy signals. Methods based on the change in the mode shape curvature, the flexibility, and the flexibility curvature was less efficient in the case of complex and simultaneous damages.

The review works which are available up-to-date have been presented and covered the literature up to 2006. The researchers found that vibration techniques have the scope to a flexible, multidisciplinary and robust detection methodology for

different types of rotors, and this would go a long way to increase the overall reliability and safety of rotating machinery, in general.

Crack detection and identification based on modal parameters

Previous reviews showed the damage diagnosis based on changes in natural frequencies and mode shapes/modal parameters was the choice of vibration based methods, which is still in use.

Inagaki et al. (1981) used a procedure with eigen frequency measurements to find the size and location of the crack. The review works such as Salawu (1997) and Doebling et a. (1998) have extensive survey of literature on the crack detection and identification based on modal parameters since 1970s to 1990s. In present work, most of the review works has been concentrated on recent literature.

Sekhar and Prabhu (1992) considered the detection of cracks in shafts by measuring the changes in an adequate number of natural frequencies by using FEM. They observed that the changes in natural frequencies and a shift in node positions for higher modes due to a crack were appreciable in cases of shafts with the low slenderness ratio.

Narkis and Elmalah (1996) demonstrated the possibility of crack identification in cantilever beams under uncertain end-conditions using free vibrations. A method was developed for characterizing the effect of clamp rigidity and for calculation of the crack location. It was shown that when the clamp rigidity of an undamaged cantilever

beam changes, the corresponding relative frequency changes were equal for all bending modes and unequal changes in relative frequencies indicated the presence of cracks.

Ruotolo and Surace (1997) presented a method, which uses modal parameters of lower modes for the non-destructive detection and sizing of cracks in beams. The finite element model of the structure was used to calculate the dynamic behaviour of the system and an inverse problem in optimization was formulated and solved by employing the genetic algorithm.

Lee and Chung (2000) presented a method for identifying a crack in a one-dimensional beam-type structure using the lowest four natural frequencies. They found that predictions in the position of the crack were not as good as for other positions, when the crack is close to the clamped end of a cantilever beam.

Chinchalkar (2001) described a numerical method for determining the location of a crack in a beam of varying depth, when the lowest three natural frequencies of the cracked beam were known. The crack was modeled as a rotational spring.

Dilena and Morassi (2002) focused on detecting a single crack when damage-induced shifts in nodes of mode shapes of a beam in the bending vibration were known. It was shown analytically/experimentally how the direction by which nodal points shift could be used to estimate the location of the damage.

Patil and Maiti (2003) presented a method for modeling the transverse undamped free vibration of Euler-Bernoulli beams with multiple open cracks. The transfer matrix method with the rotational spring representation of a crack was used from the approach of Hu and Liang (1993) for detecting cracks. Simply supported beams, cantilever beams, beams on elastic foundation, and multiple pin supports were examined.

Kim and Stubbs (2003) presented a method to locate and estimate the size of a crack by using changes in natural frequencies of a structure and outlined a crack detection algorithm. They formulated a crack location model and a crack size model by relating fractional changes in the modal energy to changes in natural frequencies due to damages.

Khiem and Lien (2004) formulated a non-linear optimization problem for the multi-crack detection in a beam with the help of natural frequencies. The spring model of the crack was applied to establish the frequency equation based on the dynamic stiffness of the multiple cracked beam.

Dong et al. (2004) presented a continuous model for the vibration analysis and the parameter identification of a static (non-rotating) rotor with an open crack, which was based on two assumptions that the cracked rotor is an Euler-Bernoulli beam with the circular cross-section and that the cracked region was modeled as a local flexibility with fracture mechanics methods. They numerically analyzed effects of the location and depth of the crack on the changes in eigen frequencies and mode shapes

of the cracked rotor, and the ratios of the changes in the first two eigen frequencies for rotors with shallow cracks.

Suresh et al. (2004) studied the flexural vibration of a cantilever beam having a transverse surface crack. Modal frequencies were used to train a neural network to identify both the crack location and depth. They found that the sensitivity of modal frequencies to a crack was increased when the crack was near the root and was decreased as crack moves to the free end of the cantilever beam.

Patil and Maiti (2005) verified experimentally a method for the prediction of the location and the size of multiple cracks based on the measurement of natural frequencies for slender cantilever beams, with two and three normal edge cracks. The analysis was based on the energy method and the representation of a crack by a rotational spring.

Chang and Chen (2005) predicted the depths and positions of multi cracks in beams by proposing a technique for the structure damage detection based on the spatial wavelet analysis of modal parameters. The limitation of this method is that there are two peaks near the boundaries in the wavelet plot and the crack could not be detected when the crack is near the boundaries.

Dharmaraju and Sinha (2005) conducted a modal testing on free-free beams having no crack, one crack, and two cracks cases. The obtained frequency response functions at various test locations of beams were used to extract modal parameters by multi-degrees of curve fitting. The variation in four anti-resonances along the length

of the beam was compared and they observed that it was difficult to locate the actual crack locations.

Hadjileontiadis et al. (2005) presented a technique for the crack identification in beam structures based on the fractal dimension analysis. The fundamental vibration mode of a cracked cantilever beam was analyzed and the location of the crack was determined by the sudden changes in the spatial variation of the analyzed response, while the size of the crack was related to the fractal dimension measure. The technique was validated by experiments on cracked plexiglas beams.

Cai and Shin (2005) predicted the depth of an elliptical surface crack in a cylindrical rod by a normalized area-compliance method. The method involved a combination of the optical surface crack length measurement and the specimen compliance measurement.

Nahvi and Jabbari (2005) approached, analytically and experimentally, the crack detection in cantilever beams based on measured frequencies and mode shapes. The intersection of contours of the plots of non-dimensional frequency in terms of the non-dimensional crack depth and location with the constant modal natural frequency planes were used to relate the crack location and depth.

Chasalevris and Papadopoulos (2006a) studied the dynamic behaviour of a cracked beam with two transverse surface cracks. A local compliance matrix of two dofs, bending in the horizontal and vertical planes was used in modeling transverse crack in the rotating shaft. The wavelet transformation of a vibration mode or of the

vibration response of the structure was used to locate cracks and then depths and respective angles were determined.

Bouaanani (2006) examined the effect of damage location and size on the modal sensitivity of suspended cables by a numerical finite difference approach with sag-extensibility and bending stiffness were taken into account. It was shown that some trends could be identified, for the out-of-plane vibration despite the complexity of the relationship between the damage and dynamic properties of cables.

Yang and Liu (2006) presented a coupled method for the structural damage identification. The approximate change of the flexibility matrix was calculated using a few lower modes to obtain the damage localization criterion, which was used to localize the damage. The damage extent was obtained by the natural frequency sensitivity method.

Jaishia and Ren (2006) were carried out a sensitivity-based finite element model updating for the damage detection. They formulated the objective function consisting of the modal flexibility residual and its gradient, and used the optimization algorithm to minimize the objective function for the damage detection.

First few natural frequencies, usually up to first four modes, of the cracked structure were mostly used for the single/multi cracks detection in structures. It was observed that predictions of crack location were not good when the crack is close to the boundaries. This difficulty remains even with the use of anti-resonances for crack

detections. Hence, more supportive information like forced linear responses are needed along with the modal parameters of the cracked structures.

Crack detection and identification based on linear /nonlinear responses

As suggested in the review works, the level of sensitivity that modal parameters have to small flaws in a structure and the ability to discriminate between changes in the modal properties resulting from damage and those changes resulting from variations in the measurements should be improved. Flaw detection and identification methods based on linear/nonlinear responses could be the alternative for the methods based on modal parameters.

Imam et al. (1989) developed a 3D finite element crack model and a nonlinear rotor dynamic code to model a cracked rotor system. They developed variety of vibration signatures indicating a rotor crack. Both the analytical crack model and the crack signature analysis techniques were experimentally validated. This paper described steps of the development, starting from the technical concept to the commercial field applications.

Rizos et al. (1990) proposed a crack identification method for a cantilever beam with the rectangular cross-section based on flexural vibrations. The crack was assumed to be a transverse surface crack, extending uniformly along the width of the structure. The method could be used to locate the crack roughly and then one of the local methods (such as ultrasonic, radiography, etc.) could be used to determine the

crack characteristics more precisely. However, it could not distinguish symmetrically located crack locations in a simply supported beam.

Boltezar et al. (1998) developed a method for identifying the open transverse crack location of a uniform beam supported free-free by extending the approach from the axial (as discussed by Adams et al., 1978) to flexural vibrations. The crack was theoretically simulated by an equivalent linear spring.

Friswell et al. (1998) used a combined genetic algorithm and eigen sensitivity method to identify the location and magnitude of a damage from measured vibration data. The genetic algorithm was used to optimize the discrete damage location variables and to identify the damage location, and the eigen sensitivity was used to identify the extent of damage.

Sekhar (1999) carried out the finite element analysis of a rotor system for flexural vibrations by including two transverse open cracks. The eigen value and the stability analysis of rotor system including a shaft with two open cracks were carried out and the influence of one crack over the other for eigen frequencies, mode shapes, and for threshold speed limits were observed.

Lee and Kwon (2000) showed that the crack development in a rotor could be effectively detected by employing the complex modal testing method. In particular, the reverse directional frequency response function (dFRF) was defined between the rotation frequency modulated input and output. They showed that, the magnitude and

phase of the estimated reverse dFRF indicate the presence, severity, and circumferential location of a crack.

He et al. (2001) proposed a genetic algorithm based method for the shaft crack detection, which was formulated as an optimization problem by means of the FEM and was utilized genetic algorithms to search the solution.

Vyas and Satishkumar (2001) used a neural network simulator for the prediction of faults in the rotating machinery. A back-propagation learning algorithm and a multi-layer network were employed. The layers were constituted of nonlinear neurons and an input vector normalization scheme was built into the simulator.

Viola et al. (2001) proposed a procedure for identifying cracks in structures using the modal test data and developed the stiffness and consistent mass matrices for a two-node cracked Timoshenko beam element on the basis of Hamilton's principle.

Yang et al. (2001) developed an energy-based numerical model to investigate the influence of cracks on structural dynamic characteristics during the vibration of a beam with open cracks. The cracked beam was taken as a continuous system with varying moment of inertia and the intersection of contours from different modes was used to identify the crack location and depth.

Gounaris and Papadopoulos (2002) developed a method to identify the depth and the location of a transverse surface crack in rotating cracked shafts. In this method, a FEM was used to model a circular cross section shaft in bending, when an

open transverse surface crack was present. The effect of crack was introduced as a cracked node with the finite element of zero length and zero mass. When a crack exists in a structure, such as a beam, then the excitation in one-direction causes coupled vibration in other orthogonal directions, and this property was used to identify the crack.

Yang (2002) developed a wavelet based method for the detection and the characterization of nonlinear mechanical instability induced by a transverse crack in a rotary system. The method used the wavelet's property of simultaneous time-scale resolution to extract underlying features that characterize the system and applied as the detection and diagnosis tool.

Sinha et al. (2002) presented a method for the estimation of both the location and the depth of cracks in beam-type structures by the solution of an inverse vibration problem. The methodology used a baseline FE model along with the modal test data in a gradient-based model updating method. Three experimental examples were demonstrated and they observed that the estimation of the crack location was more accurate than the estimation of the crack depth.

Owolabi et al. (2003) attempted to detect the presence of a crack in beams, and to determine its location and size, based on experimental modal analysis. Experimental investigations of the effects of cracks on the first three modes of vibrating beams (i.e., the simply supported and fixed beams) were carried out. Changes in natural frequencies and frequency response function (FRF) amplitudes as

a function of crack depths and locations were used in the crack detection methodology.

Sekhar (2004) used the continuous wavelet transform (CWT) to extract sub-harmonics from the coast-down time domain vibration signal from journal locations of cracked rotors on fluid film bearings. The CWT of a time-varying function was defined as the sum over all time of the signal multiplied by the scaled shifted versions of the wavelet function. Characteristic sub-harmonic peaks, which could not be detected by the normal fast Fourier transform (FFT) due to the non-stationary nature of the signals, could be detected by CWT.

Dilena and Morassi (2004) concerned with the identification of a single open crack in a vibrating beam, either under the axial or bending vibration, from the knowledge of the damage-induced changes in natural frequencies and anti-resonant frequencies. The non-uniqueness of the damage location problem was avoided based on the anti-resonance data and it was also shown that in the solution of the inverse problem, the noise and the modeling errors on anti-resonances were amplified strongly.

Gómez-Mancilla et al. (2004) used the cracked Jeffcott-rotor with a crack at or near its shaft mid-span and having gyroscopic effects. They detected rotor cracks from the orbital revolution around 1/2 and 1/3 of the first resonance, even if the crack-unbalance orientation was unknown.

Sekhar et al. (2005) presented the detection and monitoring of a slant crack in the rotor system using the mechanical impedance. It was shown that the effect of slant crack parameters on the normalized impedance is the same as transverse cracks, but a transverse crack is highly sensitive to the mechanical impedance compared to a slant crack. They also observed that the changes in the rotor impedance due to cracks were significant as compared to that of natural frequencies of the rotor-bearing system.

Li et al. (2005) presented a methodology to detect the crack location and the size by wavelet FEM in the modal analysis for a cracked beam. Frequency response functions, which are function of the crack location and the size, were approximated by means of surface-fitting techniques and were used in the crack identifying process.

Law and Lu (2005) identified parameters of a crack in a structural member from the strain or displacement measurements. The crack was modeled as a discrete open crack represented mathematically by the Dirac delta function. Dynamic responses were calculated based on the modal superposition and the optimization technique coupled with the regularization on the solution was used to identify cracks.

Huynh et al. (2005) presented a method, called the damage location vector, for the structural damage detection using frequency response functions. Frequency response functions were obtained from non-destructive vibration tests.

Hun et al. (2005) proposed a damage detection index called the wavelet packet energy rate index for the damage detection of beam structures. Measured dynamic

signals were decomposed into the wavelet packet components, and the wavelet energy rate index was computed to indicate the structural damage.

Dilena and Morassi (2006) dealt with the identification of a single defect in a discrete spring-mass or beam-like system by measurements of damage-induced shifts in the resonance and anti-resonance frequencies.

Rucka and Wilde (2006) presented a method for the crack identification in a beam based on the wavelet technique, which was applied to the static deflection of the beam. The wavelet transforms of static deflection lines of the beam was determined and a peak in the spatial variation of the transformed response indicated the location of the crack. Experiments were conducted using optical based transducers and the response of a structure measured with a very high precision could guarantee efficiency of this method.

Solbeck and Ray (2006) investigated a coherence approach for locating the structural damage using modal frequencies. Transfer function parameters were identified from the input-output data using Observer/Kalman filter identification method on extraction of modal properties. Using the coherence approach, a damage parameter vector was hypothesized for each damage case, using either identified or analytic structural models.

Musil (2006) explained a procedure of localizing and quantifying a crack in a vibrating structure based on measured vibration amplitudes of the first and second harmonics in some locations of the structure and utilizing the mathematical model of

an undamaged system. The effect of the breathing crack was modeled by the nonlinear (bilinear) stiffness of the element with the crack.

Ngwangwa et al. (2006) presented a damage detection technique based on the operational response monitoring by utilizing the finite element and linear elastic fracture mechanics analyses. An inverse model was determined from a finite element model using time-domain based model inversion techniques (Raath, 1992). Then, the measured operational responses from the real structure were applied to the inverse model to calculate operational forces. These forces were applied to the model to identify the stress 'hot spots', whose locations on the real structure were considered to be the likely locations for the damage. Operational responses and remaining service life were predicted for each of the damage scenario.

Liu and Yang (2006) presented a decoupled damage identification algorithm, which was similar in concept to the minimum rank update theory (Zimmerman and Kaouk, 1994). The method approached the damage identification problem in three steps: determining the number of damaged elements, localizing the damaged elements, and quantifying the damage extents.

Henry et al. (2006) performed the numerical analysis on a cracked rotor model, which took into account several crack depth and crack circumferential extension. The detection used a detectability chart based on minimum shift amplitudes detected at bearings; however, axisymmetric cracks could not be detected with this method.

Stoisser et al. (2006) investigated the online identification of cracks in the rotating machinery. Experimental results showed that the torsional resonance shift monitoring could be used as a complementary method to identify cracks.

The crack signature analysis techniques with the feature based algorithm like wavelet transform, neural networks, genetic algorithm, fuzzy logic, surface fitting techniques etc. were predominantly used in crack detection and identification. These flaw detection and identification methods based on modal parameters and linear/nonlinear responses could be good enough for test specimen in laboratory. However, their utility remains doubtful in real life structures. This enforced the researchers to go for model based crack diagnosis methods, which are discussed in subsequent paragraphs in detailed manner.

Model based crack diagnostics

Model-based methods are relied on analytical or numerical models to simulate the behavior of cracked shafts during operation, and attempt to correlate the observed vibration signature with the presence of a crack at discrete locations on the shaft. Plethora of the flaw detection and diagnostic methods were discussed in literature on non-model based/feature extractions of mainly free (and occasionally forced) responses. These can be applied up to the detection of flaws and are too complicated to apply for identification (i.e., localization and quantification) of flaws. Model based methods can be applied for the detection, localization and quantification of flaws. Since model based method is based on the mathematical model of the structures, it requires comparatively less experimental measurements and is sensitive to slight

variations in the system such as changes in physical parameters, boundary conditions, contamination of noise in the measurements, measurement errors etc. The recent trend is to detect and diagnose flaws, based on more sophisticated identification of flaw parameters with the help of physics based mathematical models.

Bachschmid et al. (2002) presented a model-based identification method for multiple faults by a least-squares fitting approach in the frequency domain, by means of the minimization of a multi-dimensional residual between vibrations in some measuring planes on the machine and the calculated vibrations due to the acting faults. The method required the definition of the models of the elements that compose the system; i.e., the rotor, bearings and the foundation, as well as the models of the faults, which could be represented by harmonic components of the equivalent force or moment systems.

Jain and Kundra (2004) discussed a model-based technique for the online identification of malfunctions in rotor systems. Changes in the dynamic behavior of the system due to the presence of the fault were taken into account by equivalent loads (i.e., fictitious forces and moments) acting on the undamaged system model. The work focused on developing a fault model for a transverse fatigue crack in the shaft along with the identification of the unbalance.

Sekhar (2004a) applied the model-based method to identify the crack in a rotor at a steady speed. The presence of crack in time domain was identified through some equivalent loads acting at the nodes of cracked finite element together with the FFT.

Sekhar (2004b) proposed a model-based method for the on-line identification of two cracks in a rotor. The fault-induced change of the rotor system was taken into account by equivalent loads in the mathematical model. The cracks were identified for their depths and locations on the shaft using the FFT.

Dharmaraju et al. (2004) developed an algorithm for estimating crack flexibility coefficients and subsequently the estimation of the equivalent crack depth based on the forced response information. The algorithm used the Euler-Bernoulli beam theory in the beam model without considering the damping in the system and required the crack location and the force to the beam to be known. The standard static reduction scheme was incorporated in the identification algorithm to eliminate some of DOFs so as to overcome the problem of measurements of all dofs at all nodal locations. Since the static reduction scheme is suitable only for low frequency excitations, the same authors, Dharmaraju et al. (2005) used the standard dynamic reduction scheme in the identification algorithm. However, it had limitation in that it required the measurement of the rotational DOFs at least at the crack element nodes. Hence, they outlined a “high frequency” condensation scheme for eliminating the rotational DOFs at crack element nodes. However, this reduction scheme could be applied only for high frequency operations and this limitation was overcome by Tiwari and Dharmaraju (2006). They used a hybrid reduction scheme in the identification algorithm to eliminate all the rotational DOFs and retain some of the linear DOFs for which measurements could be available. The hybrid reduction scheme was suitable for low, moderate, and high frequency operations.

Pennacchi et al. (2006) investigated experimentally a model-based transverse crack identification method for industrial machines. Three types of cracks were analyzed: the first was a slot, the second was a small crack (14% of the diameter) and the third was a deep crack (47% of the diameter).

The literature on mode shape measurements and condensation schemes, which are supportive to the present work only, are discussed now.

Mode Shape Measurements

There is much literature, which deals with measurement of mode shapes (i.e., both the real and complex mode shapes) and use of it for the flaw detection and diagnostics. Maia and Silva (1997), Friswell and Mottershead (1995), and Ewins (2000) developed some of the standard monographs that dealt with the measurement of mode shapes.

Morassi (1993) derived an explicit expression of the sensitivity of a natural frequency to an open crack in a beam in the bending vibration for a simple spring-line model of a crack. He concluded that the sensitivity was proportional to the square of the curvature of the corresponding mode shape, evaluated for the undamaged beam at the damaged cross-section.

Stanbridge and Ewins (1999) described a method by using scanning laser Doppler vibrometer (SLDV) in order to measure continuous modes shapes. The SLDV beam was scanned over a harmonically vibrating surface at a uniform speed;

the laser Doppler vibrometer output signal was modulated, the envelope gave the operating deflection shape (ODS) as a function of time, and hence of distance along the scan line. The complex mode contains the real (in-phase) and imaginary (quadrature) components in different proportions at each measurement location. With heavily damped structures, the ODS might be markedly complex.

Adhikari (2000) discussed identification methods for the estimation of damping, which were applied experimentally to a beam in the bending vibration with a localized constrained layer damping. Since the identification method required complex modal data, a general method for identification of complex modes and complex frequencies from a set of measured transfer functions was developed.

Inman (2001) discussed the determination of mode shapes from experimentally measured transfer functions and phase information. This is one of the many methods available for extracting modal data from frequency response functions constructed from a test data.

Barbieri et al. (2004) utilized the complex modal parameters in the experimental identification of damping. Three mechanical systems were analyzed such as system of two DOFs (e.g. two bars in balancing), thin plate clamped in one extremity and free in the other, and electric transmission line cable subjected to an axial load.

Condensation Schemes

Online fault diagnostics methods demand less computational time and effort. Hence condensation schemes are important to apply in order to reduce the size of the matrices according to the practical requirements. Some of the works that dealt with condensation schemes are reported.

Guyan (1965) and Paz (1984) proposed, respectively, the static and dynamic condensation methods for structural problems. Kane and Torby (1991) extended the modal reduction method to handle the non-symmetric rotor dynamic problems by eliminating unimportant modes and DOFs from the analytical model.

O'Callahan (1989) introduced a technique known as the improved reduction system (IRS) that is an improvement on the static reduction method, and in fact provides a perturbation to the transformation from the static case by including the inertia term as pseudo static forces.

Friswell et al. (1994) gave an iterative IRS method that converges to the same transformation as the system equivalent reduction expansion process (SEREP) (O'Callahan *et al*. 1989). The SEREP uses the computed eigenvectors to produce the transformation between the master and slave coordinates.

Suarez and Singh (1992) proposed an iterative procedure for the dynamic condensation, while calculating eigen properties of structures. A perturbation method

based on the correction of transformation matrix was presented by Kim (1998) to improve the condensation solutions.

Kim and Choi (2000) presented an analytical method, for the selection of DOFs in condensation of eigen problems. The method was based on the energies associated with the DOFs in eigen modes of structural systems. The energy of the selected DOFs was used to predict the solution accuracy in each mode.

Section 1.2 provided the state of the art survey of literature which are available in the damage detection and identification field, right from the methods based on natural frequencies up to the model based methods. Having studied the various advantages of model based methods, and noting the limitations of free vibration and forced vibration method, the identification of flaw parameter based on combined free and forced vibration response has been addressed in the present work

1.3 Present Work

In present work, a model based algorithm has been developed in order to detect, localize and quantify a flaw in beams based on both the numerical and experimental vibration measurements. The work is briefed in subsequent paragraphs.

The development of the algorithm was started based on the free vibrations. The Timoshenko beam theory (which represent Euler-Bernoulli beam as a special case) is used in modeling of the beam and the FEM is used for free vibration analysis of the beam with flaw. The flaw is modeled through standard five crack flexibility

coefficients, by considering only the bending effects i.e., for transverse loading conditions. The damping effect of the beam model is obtained with Rayleigh's damping. Numerically simulated natural frequencies and corresponding mode shapes of the beam with flaw are used in the algorithm. As the algorithm is iterative in nature, initially the crack location is obtained for an assumed crack size (i.e., the equivalent crack depth ratio) and is used to estimate the updated crack size through estimation of crack flexibility coefficients. The unbounded nature of estimation of the coefficients has been handled with help of the Tikhonov regularization technique. The difference between the estimated and assumed crack depth ratios is minimized up to the desired accuracy through further iterations whereby converged crack location and size are obtained. The numerical examples showed the algorithm found to be robust even in the presence of the measurement noise in modes shapes and measurement errors in natural frequencies.

The developed algorithm is improved, to avoid the experimental difficulties in measurement of mode shapes, based on the free (natural frequencies) and force response measurements. The excitation for forced vibrations of the beam has been provided by a harmonic force of known amplitude and frequency. The algorithm followed the similar steps of procedure as discussed before. The method has been illustrated through numerical examples. The prediction of the crack location and size are in good agreement even in the presence of the measurement error and noise.

The practicability of the developed algorithm is improved by applying a novel condensation scheme along with conventional condensation schemes. A harmonic force of known amplitude with a sine-sweep frequency is used to dynamically excite

the beam. All rotational DOFs, except at the crack element, are eliminated by the dynamic condensation scheme and for elimination of rotational DOFs at the crack element a new condensation scheme has been implemented. The procedure adopted to detect, locate and quantify the flaw was similar as in previous stages of the algorithm. Numerical examples are given to justify the applicability of the algorithm in practice.

The experimental implementation of the proposed algorithm has been carried out. A harmonic force of known amplitude with sine-sweep frequency is used to dynamically excite the beams with flaw. The Pulse software (B&K) is used for both generating the force signal for the exciter and analyzing the measured response signals. Transverse linear responses are measured and the recorded data are exported to MATLAB environment. The extracted natural frequencies and the amplitude and phase changes of the response were fed into the developed algorithm to detect, locate and estimate the flaw parameters. The obtained results are in good agreement with actual counterpart.

1.4 Organization of the Thesis

Chapter 1 introduces the present work with the review of previous works in the field of vibration measurement based damage diagnostics. The brief discussion about the present work and arrangement of thesis are provided.

Chapter 2 provides development of the algorithm based on the free vibrations. Numerically simulated natural frequencies and corresponding mode shapes of the beam with flaw are used in the algorithm. The difficulties involved in experimental

measurement of mode shapes, and in place of which forced responses were suggested, are discussed.

In Chapter 3, the developed algorithm, based on mode shapes, is improved based on the free (natural frequencies) and force response measurements. The accurate measurement of rotational DOFs is also one of the practical difficulties of implementing the algorithm, and it was suggested to use various condensation schemes in order to eliminate the inaccessible DOFs.

In Chapter 4, the practical usability of the developed algorithm is improved by applying a novel condensation scheme along with the conventional condensation schemes. The improved algorithm could be applied to detect and identify the flaw parameters based on experimentally accessible DOFs.

Chapter 5 detailed the experimental implementation of the proposed algorithm as a final part of the work. The measured natural frequencies and the amplitude and phase information of the response were utilized in the developed algorithm.

Chapter 6 concluded the developed flaw detection, localization and sizing algorithms in a beam based on vibration measurements. The scope for future works is presented and discussed.

Appendix, bibliography, and list of publication are provided at the end of the thesis.

CHAPTER 2

FLAW IDENTIFICATION USING FREE VIBRATION TECHNIQUES

2.1 Introduction

A model-based identification algorithm has been developed, in order to detect, locate, and quantify the size of a flaw, based on free vibration measurements of a beam with flaw. Measured natural frequencies (at least two) and corresponding mode shapes of the beam with flaw are used in the identification algorithm. The Euler-Bernoulli beam theory is used to model the beam. The flaw of the beam is modeled through standard five flaw (crack) flexibility coefficients, by considering bending effects only. The damping in the beam is assumed to be Rayleigh's damping. The FEM is used in the simulation of the beam with flaw. The present identification algorithm is iterative in nature. Firstly, the size of flaw (i.e., the flaw depth ratio) is assumed; and with the help of measured and simulated natural frequencies, a possible flaw location is obtained. The obtained flaw location and measured mode shapes are used to estimate the updated flaw size through estimation of flaw flexibility coefficients. Further iterations are carried out until the estimated and assumed flaw depth ratios (as well as its location) become close, up to the desired accuracy. The applicability of the algorithm in the present chapter has been tested through numerical examples; and is found to be adequate even in the presence of the measurement noise in modes shapes and measurement errors in natural frequencies.

2.2 System Modeling

In the present subsection assumptions involved in the modeling the system under consideration have been stated. A brief description of the flaw model, which is considered for the development of an algorithm for the flaw localization and sizing, has been presented. System equations of motion have been presented for a beam with flaw and the eigen analysis for the damped free vibration is presented briefly.

2.2.1 Assumptions

The Euler-Bernoulli beam theory, which incorporates the bending deformations, is used for the analysis of transverse free vibrations of a beam. The effect of Rayleigh's damping (Clough, 1993) is included in the formulation of equations of motion of the beam. The FEM is used to develop the discretized model of the beam. The spinning of the beam is not considered. The flaw is assumed to be an open flaw in the present analysis, hence, the linear analysis has been performed (i.e., breathing behaviour of the flaw has not been considered). A single flaw has been considered in the beam with its location and size as unknown. It is assumed that the presence of a transverse surface flaw on a beam has effect on the local flexibility and the damping; however, the effect on the mass is negligible.

2.2.2 Flaw model

Figure 2.1 shows a beam element with flaw subjected to a general loading. Let P_1 is the axial force, P_2 and P_3 are shearing forces, P_4 and P_5 are bending moments,

and P_6 is the torque; l is the beam element length, a is the flaw depth, and X-Y-Z is a rectilinear coordinate system.

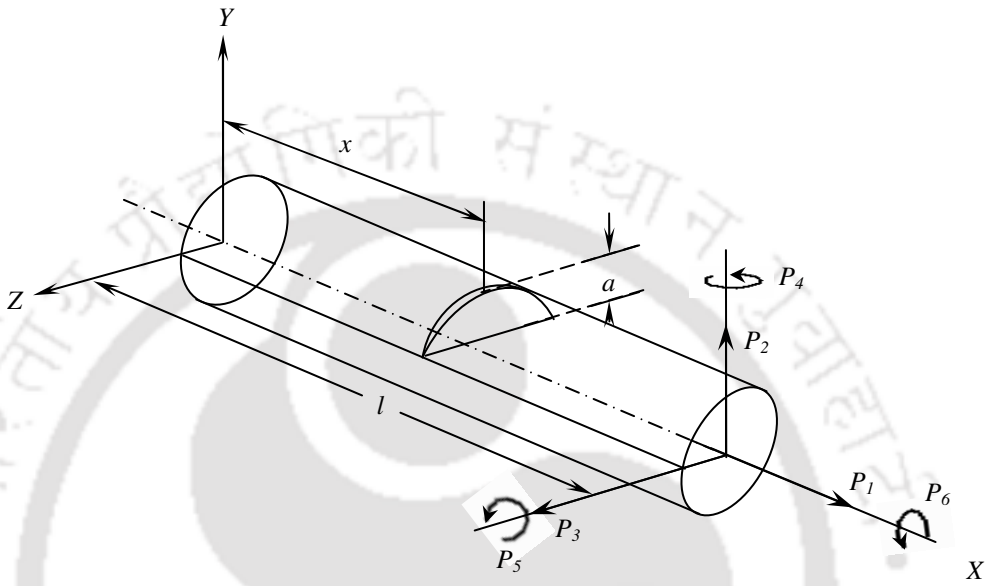

Figure 2.1 A beam element with flaw subjected to a general loading

For the transverse loading of the beam, neglecting the axial and torsional loadings, the flexibility matrix of the flaw can be expressed as (Papadopoulos and Dimarogonas, 1987),

$$\left[C_f\right]^{(e)} = \begin{bmatrix} C_{22} & 0 & 0 & 0 \\ 0 & C_{33} & 0 & 0 \\ 0 & 0 & C_{44} & C_{45} \\ 0 & 0 & C_{54} & C_{55} \end{bmatrix} \tag{2.1}$$

where $C_{22}, C_{33}, \cdots, C_{55}$ are the six non-zero flexibility coefficients of the flaw, in which four are direct coefficients and remaining two are cross-coupled coefficients.

Detailed expressions of flexibility coefficients, for a simple flaw with a straight flaw edge (see Figure 2.2) and negligible thickness, are given in Appendix A.

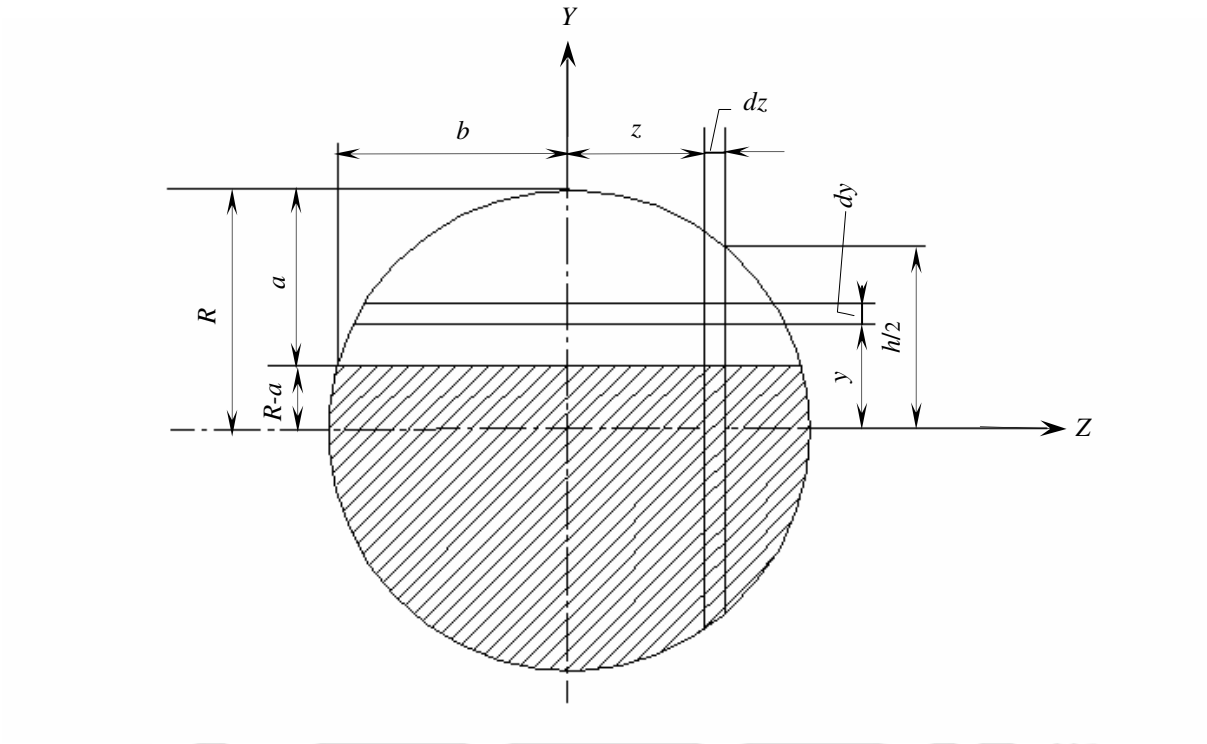

Figure 2.2 A geometry of a beam section with a simple flaw.

In Figure 2.2 the hatched part is the portion of the beam without flaw at the flaw location. Let R be the radius of the beam and b is the half-width of the beam. It is assumed that the form of equation (2.1) is still valid for a flaw with an irregular edge and a finite thickness, which is the case in the reality. Due to the symmetric property of the flexibility matrix, the off-diagonal flexibility coefficients could be written as

$$C_{45} = C_{54} \tag{2.2}$$

Hence, total five independent flexibility coefficients define the flaw model for the transverse loading.

2.2.3 System equations of motion

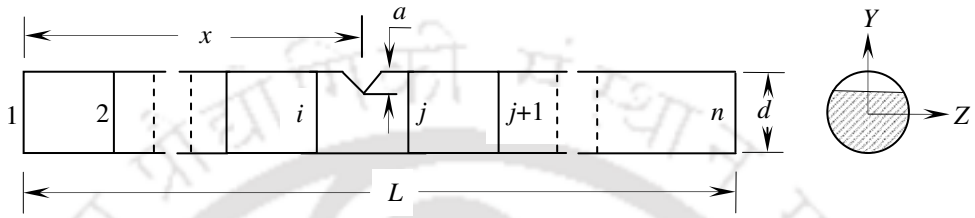

Figure 2.3 Finite element discretization of a beam with a flaw

A beam is discretized into finite elements as shown in Figure 2.3 (end conditions are not shown). The equation of motion in free vibration, for a beam element without flaw, can be written as

$$[M]^{(e)}\{\ddot{q}(t)\}^{(e)} + [D_{wf}]^{(e)}\{\dot{q}(t)\}^{(e)} + [K_{wf}]^{(e)}\{q(t)\}^{(e)} = \{0\} \tag{2.3}$$

where $[M]^{(e)}$ is the element mass matrix, $[D_{wf}]^{(e)}$ is the element damping matrix, $[K_{wf}]^{(e)}$ is the element stiffness matrix, and $\{q(t)\}^{(e)}$ is the element vector of nodal DOFs. Subscripts '*wf*' and '*e*' represent the *without flaw* and *element*, respectively. The damping matrix, $[D_{wf}]^{(e)}$, of the beam element without flaw can be expressed in terms of the element mass and stiffness matrices as

$$[D_{wf}]^{(e)} = a_0[M]^{(e)} + a_1[K_{wf}]^{(e)} \tag{2.4}$$

where a_0 and a_1 are Rayleigh damping factors (expressions for a_0 and a_1 are given in Appendix B). The equation of motion of a beam element with flaw can be expressed as

$$[M]^{(e)}\{\ddot{q}_f(t)\}^{(e)} + [D_f]^{(e)}\{\dot{q}_f(t)\}^{(e)} + [K_f]^{(e)}\{q_f(t)\}^{(e)} = \{0\} \tag{2.5}$$

where $\{q_f(t)\}^{(e)}$ is the nodal DOFs of the beam element with flaw, and the subscript '*f*' represents the *flaw*. $[K_f]^{(e)}$ is the stiffness matrix of the beam element with flaw, and it is given as

$$[K_f]^{(e)} = [T][C]^{(e)^{-1}}[T]^T \tag{2.6}$$

with

$$[C]^{(e)} = [C_o]^{(e)} + [C_f]^{(e)} \tag{2.7}$$

and

$$[C_o]^{(e)} = \begin{bmatrix} l^3/3EI & 0 & 0 & l^2/2EI \\ 0 & l^3/3EI & -l^2/2EI & 0 \\ 0 & -l^2/2EI & l/EI & 0 \\ l^2/2EI & 0 & 0 & l/EI \end{bmatrix} \tag{2.8}$$

where $[C_o]^{(e)}$ is the flexibility matrix of the beam element without flaw, $[C_f]^{(e)}$ is the flexibility matrix of the flaw and it is defined in equation (2.1), $[C]^{(e)}$ is the total flexibility matrix of the beam element with flaw, $[D_f]^{(e)}$ is the damping matrix of the beam element with flaw, EI is the flexural rigidity of the beam, and l is the element length. $[T]$ is the transformation matrix, and it can be expressed as (Papadopoulos and Dimarogonas, 1987)

$$[T]^T = \begin{bmatrix} -1 & 0 & 0 & -l & 1 & 0 & 0 & 0 \\ 0 & -1 & l & 0 & 0 & 1 & 0 & 0 \\ 0 & 0 & -1 & 0 & 0 & 0 & 1 & 0 \\ 0 & 0 & 0 & -1 & 0 & 0 & 0 & 1 \end{bmatrix} \tag{2.9}$$

The damping matrix of the beam element with flaw, $[D_f]^{(e)}$, can be expressed in terms of the beam elemental stiffness and mass matrices with flaw as

$$[D_f]^{(e)} = a_0[M]^{(e)} + a_1[K_f]^{(e)} \tag{2.10}$$

where Rayleigh damping factors a_0 and a_1 remain the same as defined in equation (2.4) and presented in Appendix B. It should be noted here that even damping factors are same for elements with flaw as well as without flaw; their damping matrices are different since changes in respective stiffness matrices. Equations of motion of the complete system can be obtained by assembling contributions of elemental equations of motion with and without flaw. Then, system equations of motion becomes

$$[M]\{\ddot{q}(t)\} + [D]\{\dot{q}(t)\} + [K]\{q(t)\} = \{0\} \tag{2.11}$$

with

$$[D] = a_0[M] + a_1[K] \tag{2.12}$$

where $[M]$ is the assembled mass matrix, $[D]$ is the assembled damping matrix, $[K]$ is the assembled stiffness matrix, and $\{q(t)\}$ is the assembled vector of nodal DOFs.

2.2.4 Damped free vibrations

The system governing equation (i.e. equation (2.11)) after application of boundary conditions can be modified as

$$[\bar{M}]\{\ddot{\bar{q}}(t)\} + [\bar{D}]\{\dot{\bar{q}}(t)\} + [\bar{K}]\{\bar{q}(t)\} = \{0\} \tag{2.13}$$

where $[\bar{M}]$, $[\bar{D}]$ and $[\bar{K}]$ are the reduced assembled mass, damping, and stiffness matrices. The solution for the standard eigen value problem of equation (2.13) can be sought as

$$\left(-\lambda[I] + [Z]\right)\{h_0\} = 0 \tag{2.14}$$

with

$$[Z] = \begin{bmatrix} [0] & [I] \\ -[M]^{-1}[K] & -[M]^{-1}[D] \end{bmatrix} \quad \text{and} \quad \{h_0\} = \begin{Bmatrix} \{\bar{q}_0\} \\ \{\dot{\bar{q}}_0\} \end{Bmatrix}$$

where λ is the eigen value and it appears as complex conjugate pairs. Imaginary part of the eigen value λ represents the damped natural frequency of the system. The vector $\{h_0\}$ represents the eigen vector, which can be obtained after substituting the eigen value in equation (2.14). More discussions on mode shapes have been included in Section 2.4.

2.3 Flaw Localization and Sizing Algorithms

The present section consists of three subsections: (a) a method has been developed to obtain the flaw flexibility coefficients and size, based on measured modal parameters when the location of the flaw is known (b) a procedure has been described for obtaining regularized flaw flexibility coefficients especially when the location of the flaw is not known a priori (c) an iterative procedure has been developed that estimates the flaw location and size, based on measured modal parameters.

2.3.1 Identification algorithm for the flaw sizing

In the present section, an identification algorithm has been developed based on the measured modal parameters for estimation of the flaw size, when flaw location is assumed to be known. In equation (2.11), the stiffness,$[K]$, and damping, $[D]$, matrices are split as

$$[K]=[K_{wf}]+[K_f] \tag{2.15}$$

and

$$[D]=[D_{wf}]+[D_f] \tag{2.16}$$

where $[K_{wf}]$ and $[K_f]$ are of the same size as that of the reduced assembled stiffness matrix $[K]$ in equation (2.13). The matrix $[K_f]$ contains contribution of DOFs only from the beam element with flaw, whereas the matrix $[K_{wf}]$ contains contribution of all other elements. Noting equations (2.12) and (2.15), equation (2.16) can be written as

$$[D]=a_0[M]+a_1[K_{wf}]+a_1[K_f] \tag{2.17}$$

The matrix $[K_f]$ contains non-zero terms only corresponding to the flaw nodal DOFs $\{Q_f\}^{(e)}$. Noting equations (2.15) and (2.17), equation (2.11) can be reduced to the following form

$$[K_f]^{(e)}\{Q_f\}^{(e)}=\{\hat{F}_f\} \tag{2.18}$$

with

$$\{\hat{F}_f\}=\frac{-1}{(1+\mathrm{j}\omega a_1)}\left(-\omega^2[M]+\mathrm{j}\omega\left(a_0[M]+a_1[K_{wf}]\right)+[K_{wf}]\right)\{Q_f\}^{(e)}$$

where $\{\hat{F}_f\}$ contains force vector elements only corresponding to the beam element with flaw nodal DOFs $\{Q_f\}^{(e)}$. Equation (2.18) can be used to obtain the unknown flexibility coefficients contained in matrix $[K_f]^{(e)}$, which in turn will be used to

obtain an equivalent flaw depth. The term equivalent flaw depth refers to the flaw depth, *a*, for a flaw with a straight edge flaw front and negligible thickness, as shown in Figure 2.2. In the present algorithm, the equivalent flaw depth is obtained from the estimated flaw flexibility coefficients. In case the flaw front has irregular geometry, the present algorithm would estimate the flexibility coefficient accordingly, however, it is difficult to get the actual shape of the flaw from the estimated flaw coefficients. Hence, to have an assessment of the severity of the irregular shaped flaw front, the equivalent flaw depth concept has been introduced. Since the damping of the beam element with flaw is considered proportional to the mass and stiffness matrices of the beam element with flaw (i.e., equation (2.12)); the damping matrix of the beam element with flaw will also be known as a by-product, once flexibility coefficients of the flaw are estimated. However, since the matrix $[K_f]^{(e)}$ contains the flexibility coefficient matrix $[C]^{(e)}$ in the form of its inverse, hence the resulting identification algorithm becomes a non-linear estimator and that has inherent problem of convergence along with the problem of obtaining the physically meaningful parameters. The non-linear estimator has been avoided with the following re-arrangement of equation (2.18). On post-multiplication of the response, $\{Q_f\}^{(e)}$, on both sides of equation (2.6), it yields

$$[K_f]^{(e)}\{Q_f\}^{(e)} = [T][C]^{(e)^{-1}}[T]^T\{Q_f\}^{(e)} \tag{2.19}$$

On equating equations (2.18) and (2.19), we get

$$[T][C]^{(e)^{-1}}[T]^T\{Q_f\}^{(e)} = \{\hat{F}_f\} \tag{2.20}$$

Equation (2.20) can be rearranged as

$$[C]^{(e)}\{A_1\} = \{B_1\} \tag{2.21}$$

with

$$\{A_1\} = \left([T]^T[T]\right)^{-1}[T]^T\{\hat{F}_f\} \tag{2.22}$$

and

$$\{B_1\} = [T]^T\{Q_f\}^{(e)}. \tag{2.23}$$

On substituting equation (2.7) into equation (2.21) and after some rearrangement, we get

$$[C_f]^{(e)}\{A_1\} = \{B_2\} \tag{2.24}$$

with

$$\{B_2\} = \{B_1\} - [C_0]^{(e)}\{A_1\}. \tag{2.25}$$

Noting equations (2.1) and (2.2), equation (2.24) can be written in the expanded form as

$$\begin{bmatrix} C_{22} & 0 & 0 & 0 \\ 0 & C_{33} & 0 & 0 \\ 0 & 0 & C_{44} & C_{45} \\ 0 & 0 & C_{45} & C_{55} \end{bmatrix} \begin{Bmatrix} A_{1_1} \\ A_{1_2} \\ A_{1_3} \\ A_{1_4} \end{Bmatrix} = \begin{Bmatrix} B_{2_1} \\ B_{2_2} \\ B_{2_3} \\ B_{2_4} \end{Bmatrix} \tag{2.26}$$

Equation (2.26) can be rearranged, in the standard linear regression equation, as

$$[S]\{C\} = \{B_2\} \tag{2.27}$$

with

$$[S] = \begin{bmatrix} A_{l_1} & 0 & 0 & 0 & 0 \\ 0 & A_{l_2} & 0 & 0 & 0 \\ 0 & 0 & A_{l_3} & A_{l_4} & 0 \\ 0 & 0 & 0 & A_{l_3} & A_{l_4} \end{bmatrix} \tag{2.28}$$

and

$$\{C\} = \{C_{22} \quad C_{33} \quad C_{44} \quad C_{45} \quad C_{55}\}^T \tag{2.29}$$

In equation (2.27), the vector, $\{C\}$, contains all unknown flaw flexibility coefficients as given in equation (2.29). The matrix, $[S]$, and the vector, $\{B_2\}$, contains all known information (i.e. the beam element model without flaw, natural frequencies and corresponding mode shapes) except the flaw location. For a known (or assumed) flaw location (a flaw localization and sizing procedure is presented in Subsection 2.3.3), equation (2.27) contains four equations with five unknown flaw flexibility coefficients; hence it is an underdetermined system of equations. Since flaw flexibility coefficients do not change with type of mode getting excited in the beam, hence, with minimum up to second modes, we can have eight equations to solve for five unknowns. Then, the system of equation will be an over-determined, which could be solved using the normal least squares method.

Theoretically, from the fracture mechanics approach flaw flexibility coefficients are expressed as a function of flaw depth ratio $\bar{a} = a / R$ (Papadopoulos

and Dimarogonas, 1987). The error function between the identified flexibility coefficients and the theoretical (superscript: *th*) flexibility coefficients can be defined as

$$\pi_{error} = \sum_{i=2}^{5} (C_{ii}^{th} - C_{ii})^2 + (C_{45}^{th} - C_{45})^2 \tag{2.30}$$

where C_{ij} is the flaw flexibility coefficient. Minimizing the error function with respect to the flaw depth ratio $\bar{a}$ in conjunction with the bi-section and Newton-Raphson methods, the equivalent flaw depth ratio ($\bar{a}_e$) can be obtained.

However, on careful inspection of equations (2.27)-(2.29), it can be observed that flexibility coefficients C_{22} and C_{33} are independent and uncoupled with other coefficients C_{44}, C_{55}, and C_{45}; which themselves are coupled. This condition sometimes leads to unbounded estimation of C_{22} and C_{33} in the presence of measurement noise due to ill-conditioning of the matrix [*S*], especially when the location of the flaw is not correct. In Subsection 2.3.2, a regularization technique is discussed which tackles this unbounded estimation of flexibility coefficients.

2.3.2 Regularization method of estimating flexibility coefficients

In order to improve the conditioning of the matrix [*S*], the Tikhonov regularization method (Tikhonov, 1977) is incorporated in the estimation procedure. The regularized solution for unknown flaw flexibility coefficients is obtained by minimizing the following function (noting equations (2.27) and (2.30))

$$\left\|[S]\{C\}-\{B_2\}\right\|^2+\eta^2\left\|\{C\}-\{C^{th}\}\right\|^2 \tag{2.31}$$

where $\|.\|$ represents the matrix 2-norm, η is the regularization parameter. The vector, $\{C^{th}\}$, contains the theoretical flaw flexibility coefficients (Papadopoulos and Dimarogonas, 1987), and it is given as

$$\{C^{th}\}=\{C_{22}^{th} \quad C_{33}^{th} \quad C_{44}^{th} \quad C_{45}^{th} \quad C_{55}^{th}\}^T \tag{2.32}$$

The Tikhonov regularization method has been described in Appendix C.

2.3.3 Flaw localization and sizing procedures

The identification algorithm for the flaw size, which has been described in Subsection 2.3.1, requires the flaw location to be known. In order to relax this constraint, a flaw localization procedure has been presented in this subsection based of the fundamental natural frequency. Then, it will be of more practical importance when the position of the flaw can also be identified along with the flaw size. Experimentally measured transverse natural frequencies and corresponding mode shapes would be used, to iteratively obtain the flaw location and size. Various steps involved in the proposed algorithm are as follows:

1. For a given beam with an unknown flaw location and its size, the fundamental transverse natural frequency (higher natural frequencies could be taken

without difficulty, however, possibility of the measurement error would be more and the excitation will be difficult) is obtained by standard modal testing methods (e.g. the impact test method; Ewins, 2000).

2. From the finite element model of the beam with flaw, the fundamental transverse natural frequency (as in Step 1, here also accordingly higher natural frequencies could be taken, however, with compromise in the numerical error) is obtained for a particular value of an assumed flaw depth and for different possible values of flaw locations.
3. The experimentally obtained transverse natural frequency is matched with the one obtained by the FEM, which gives possible flaw locations for the assumed flaw size.
4. The possible flaw location obtained in Step 3 is used to obtain an updated value of the assumed flaw depth ratio with the identification algorithm, which gives the equivalent flaw size when the flaw location is known from measured mode shapes.
5. With the new value of the flaw depth ratio obtained in Step 4, Steps 2 to 4 is repeated until the convergence of both the flaw location and size is achieved up to the desired level of accuracy.

Figure 2.4 gives a flow chart for more clarity of the flaw location and size identification algorithm as discussed above in accordance with the developed computer code for the present study. It should be noted that as a by-product the present identification algorithm gives flexibility coefficients of the flaw (i.e. equation (2.1)) and the damping matrix of the flaw beam (i.e. equation (2.11)).

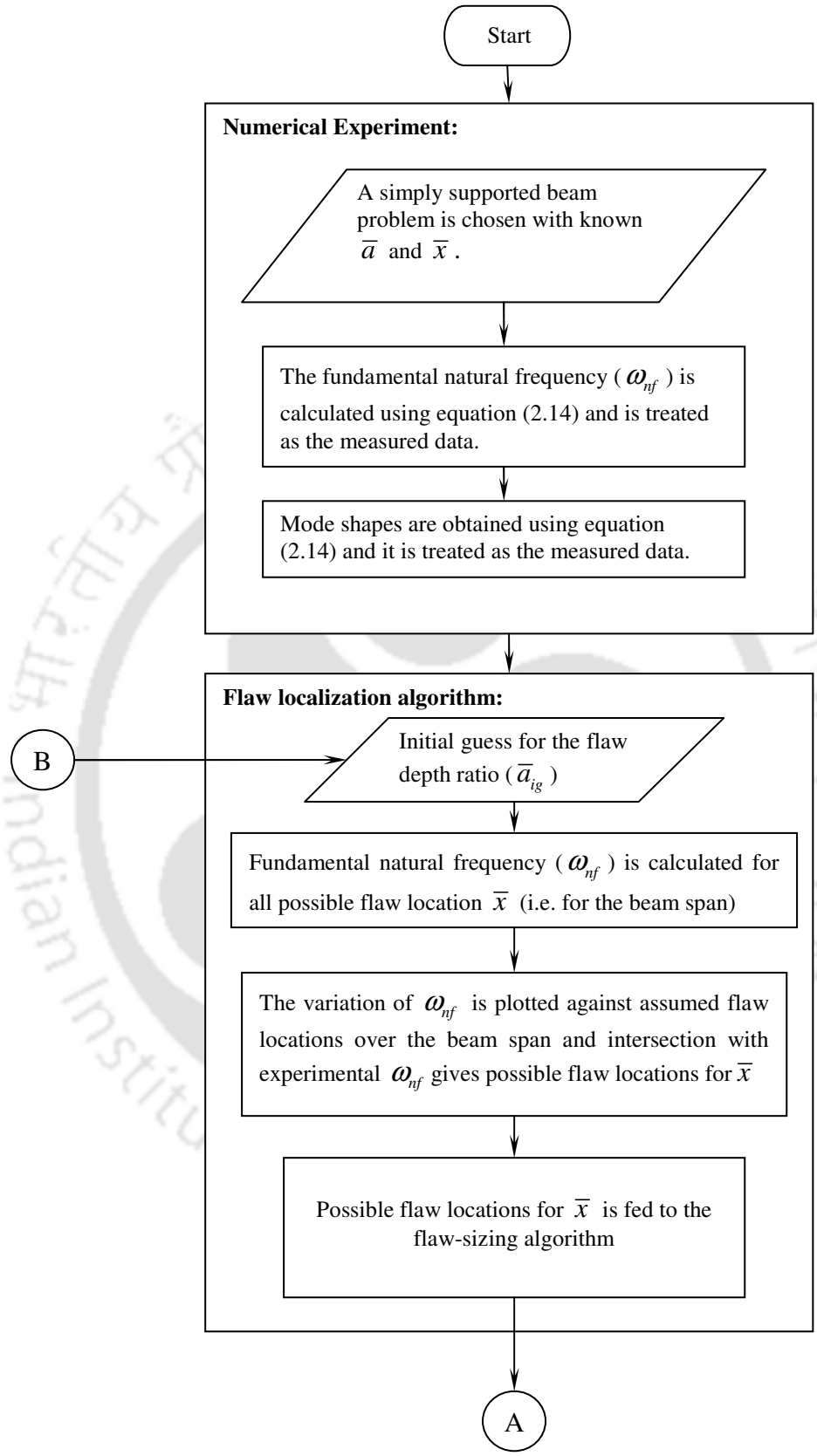

Figure 2.4 A flow chart for the flaw localization and sizing algorithm (continued)

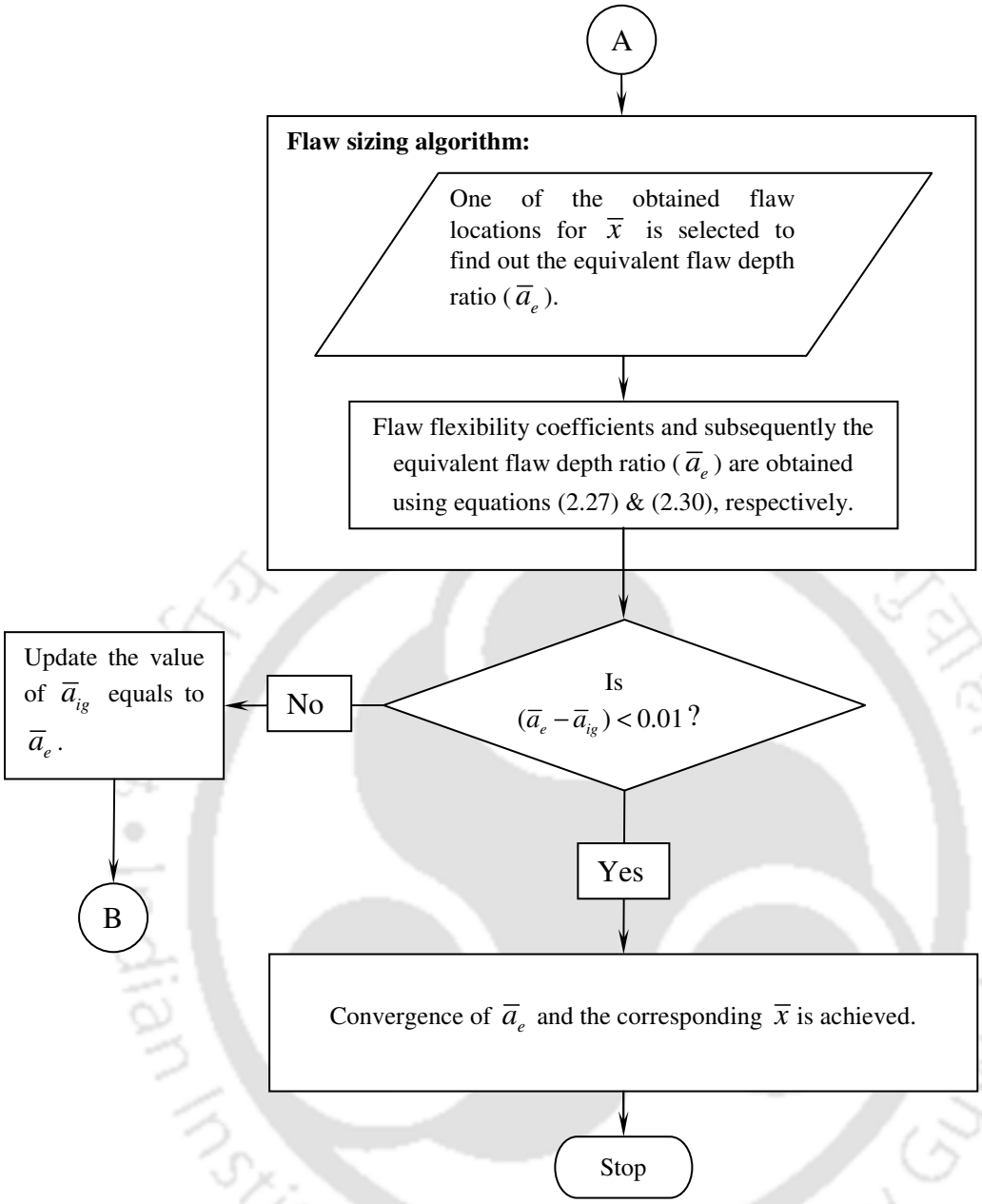

Figure 2.4 The flow chart for the flaw localization and sizing algorithm.

2.4 Numerical Examples

The flaw localization and size identification algorithm has been tested using numerical simulations for beams with the simply supported and cantilever boundary conditions. For numerical examples, beam parameters are given in Table 2.1.

The present identification algorithm needs the measurement of natural frequencies and corresponding mode shapes. To mimic the actual experimentation, a deliberate flaw is introduced in the numerical model of the beam with a known flaw location and size, for generating of natural frequencies and corresponding mode shapes. This numerically generated information is fed to the present identification algorithm, to extract back the location and the size of the flaw to test the developed algorithm. To check the robustness of the present algorithm, a biased measurement error is introduced in the natural frequency and a random measurement noise is introduced in mode shapes. Regularization technique described in Subsection 2.3.2 is used throughout in numerical examples.

2.4.1 Simply supported beams

2.4.1.1 Numerical experiment for modal parameters:

To generate experimental modal parameters, which are required for testing the developed identification algorithm for the estimation flaw location and its size, a numerical experimentation was performed.

Table 2.1 Parameters used in numerical experiments

Parameters	Values
Diameter of the circular beam, D	0.01 m
Beam length, L	1.0 m
Young's modulus of the beam material, E	2.06×10^{11} N/m^2
Density of the beam material, ρ	7800 kg/m^3
Number of beam elements, N	30
Damping ratio, ζ	0.01
Measurement error* in the natural frequency	5 %
Measurement noise in mode shapes	1 %

* Defined in terms of change in the natural frequency due to the flaw as compared to the intact beam.

For beam parameters as given in Table 2.1, the fundamental natural frequency of the intact simply supported beam is obtained by using equation (2.14), and is found to be 20.18 Hz. It should be noted that for the present analysis both orthogonal planes motion is considered, and for the intact beam the motion in these planes are uncoupled. Hence, natural frequencies corresponding to orthogonal planes are same. Now a flaw of the depth ratio $\bar{a} = a/R = 0.7$ is introduced at the flaw location ratio $\bar{x} = x/L = 0.4$ (i.e., at 12th element).

Each natural frequency of the intact beam (which has two same natural frequencies for the undamaged configuration in two orthogonal planes) splits into a pair of close frequencies, when the flaw is present. For the present example, the fundamental natural frequency (i.e., 20.18 Hz) is found to split into 19.96 Hz and

20.17 Hz. Natural frequencies up to the second natural frequency are summarised in Table 2.2 for beams without and with flaw.

Table 2.2 Natural frequencies of beams without and with flaw for the simply supported and cantilever boundary conditions

Mode no.	Resonance frequencies (Hz)			
	Simply supported boundary conditions		Cantilever boundary conditions	
	Intact beam	Beam with flaw	Intact beam	Beam with flaw
1	20.18	19.96	7.19	7.11
	20.18	20.17	7.19	7.19
2	80.73	80.42	45.06	44.86
	80.73	80.73	45.06	44.99

For the proposed flaw localization and sizing algorithm a more sensitive natural frequency (i.e., the minimum of two split frequencies) and corresponding mode shape has been considered. For the present case since the Rayleigh's damping has been considered, hence, even when eigen values are complex, eigen vectors (i.e. mode shapes) remain real (or at least they have 0^o or 180^o phase difference among various DOFs at a single natural frequency). Moreover, in the case of viscous or other kind of heavy damping, the solution of eigen problems result in eigen values and eigenvectors, which are complex and appear as conjugate (this is also true for the measurement of mode shapes of dynamic systems through the modal testing). In such cases, complex conjugate eigen values and corresponding mode shapes need to be considered for the identification procedure.

The physical interpretation of a complex mode is that each mode shapes describes the relative magnitude and phase of the motion of the DOF associated with a mode, when the system is excited at that mode only. The relative position of each mass can be out of phase by the amount indicated by the complex part of the mode shapes entry. In the undamped real-mode case, the mode-shape vector is real and indicates the relative position of each mass at any given instant of time at a single frequency. The present algorithm is capable of handling such complex mode shapes as input, while minimising the cost function (2.30). It should be noted that the reduction in natural frequency depends upon the flaw location and the vibration mode considered. In general, when the flaw is located at the nodal point the reduction in natural frequency due to presence of the flaw is minimum, however, its effect is maximum when the flaw is located at the anti-nodal point, irrespective of the vibration mode. Figures 2.5 and 2.6 show the first and second mode shapes, respectively, for beams without and with flaw. In the presence of flaw, the motion in orthogonal planes gets coupled due to cross-coupled flexibility coefficients (i.e., C_{45} in equation (2.1)) of the flaw.

2.4.1.2 Identification of flaw parameters:

The flaw localization and size estimation procedure is used iteratively, until the desired accuracy for $\bar{x}$ and $\bar{a}$ is achieved. The variation of the natural frequency ratio (i.e., ratio of natural frequencies of beams without and with flaw ($\omega_{n_f} / \omega_{n_{in}}$)) is obtained from the finite element analysis (i.e., equation (2.14)) of the experimental setup configuration with different possible flaw location (i.e., from element number 1

to 30, alternatively) for various chosen flaw depth ratios (i.e., 0.1 to 1.0 in steps of 0.1, alternatively).

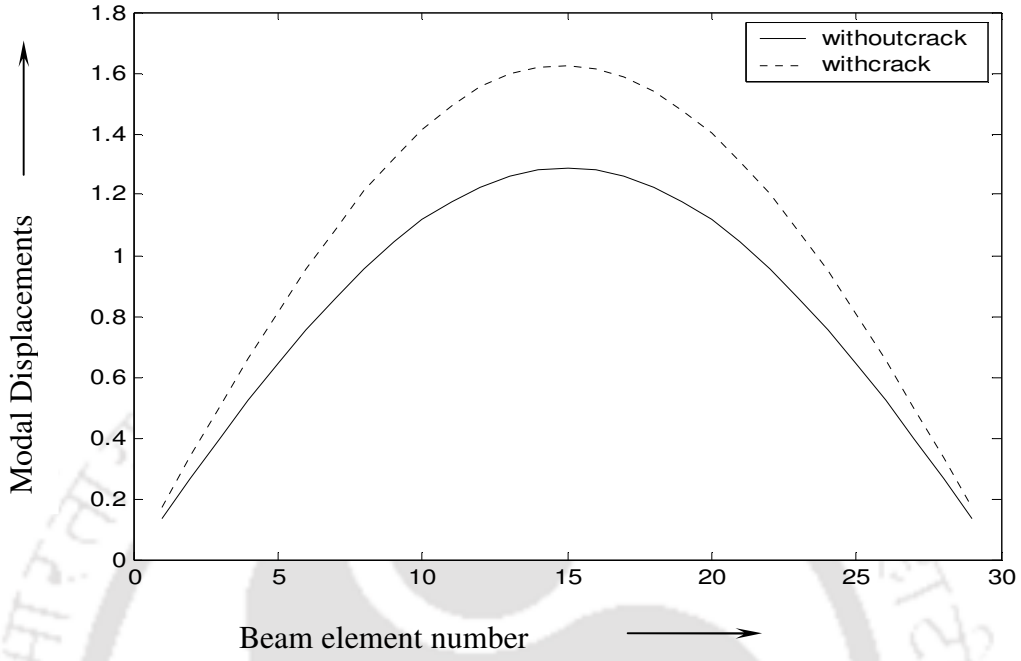

Figure 2.5 The first mode shape of beams without and with flaw for simply supported boundary conditions

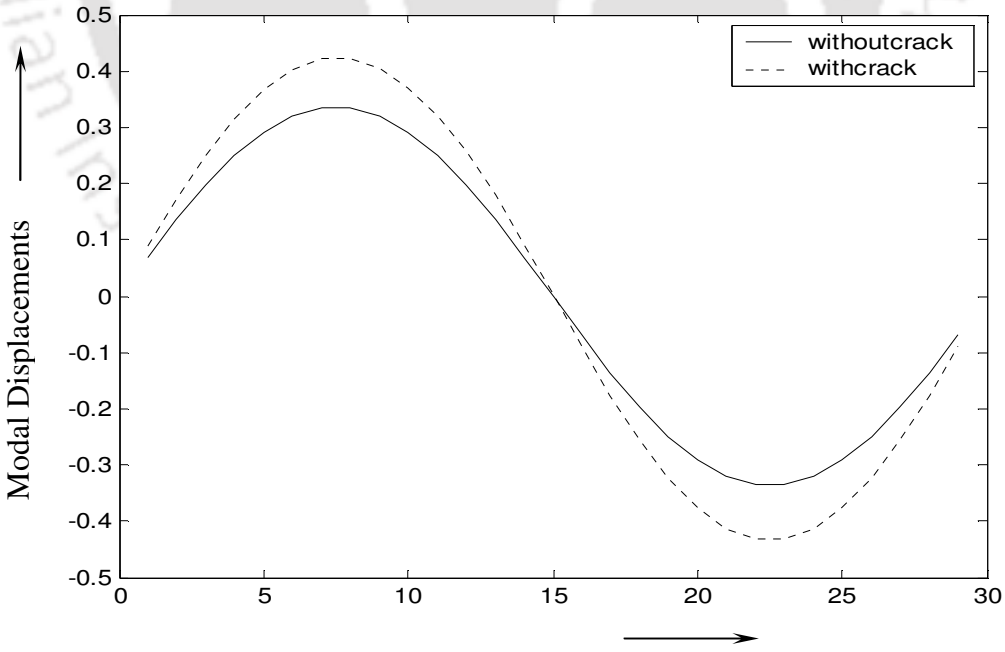

Figure 2.6 The second mode shape of beams without and with flaw for simply supported boundary conditions

Figure 2.7 shows such a variation of first natural frequencies with different possible flaw locations for different chosen flaw sizes. This could be used to obtain the flaw location with the help of experimentally measured natural frequency. Figure 2.8 shows the procedure of finding the flaw location. For the flaw localization procedure the flaw depth ratio is assumed initially between 0.9 and 1.0 (based on our simulation exercise, it is advisable to use a higher flaw depth ratio as the initial guess). For an initially assumed flaw depth ratio of $\bar{a}_{ig}$ = 0.9 and the measured natural frequency of 19.96 Hz, it gives initial flaw locations to be 0.23 (7th element) and 0.80 (24th element).

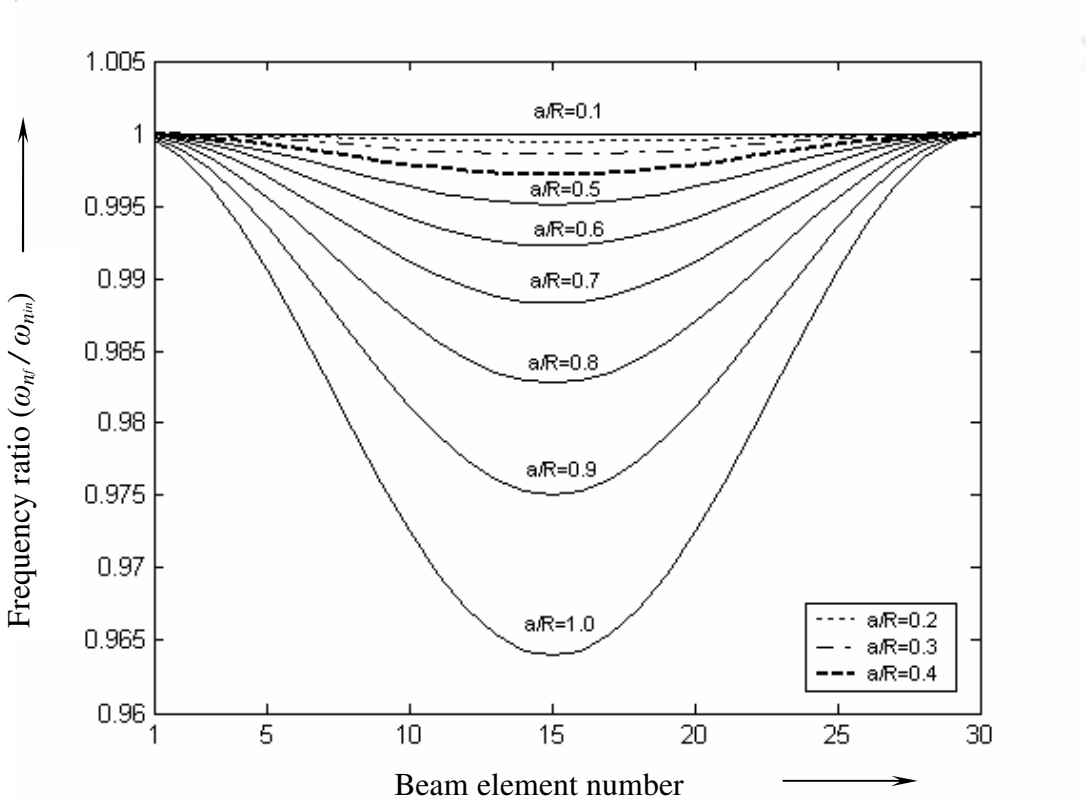

Figure 2.7 Variation of first natural frequency ratios versus flaw positions for different flaw depth ratios in the case of the simply supported beam

With one of this flaw location, flexibility coefficients of the flaw are obtained from estimation equation (2.27) and subsequently it gives the equivalent flaw depth from equation (2.30). The equivalent flaw depth is used as a new flaw depth and variations of natural frequencies are obtained by using equation (2.14) to get a new possible flaw location. The convergence criteria adopted here is that the difference between flaw depth ratios of two consecutive iterations should be less than 0.01. It is possible to get two or more intersection points (it depends upon boundary conditions), which corresponds to that many number of possible flaw locations, however, as described in the flow chart (i.e. Figure 2.4) and illustrated in Table 2.3 with the present algorithm the flaw location converges to actual flaw only (i.e. at $\bar{x}$ = 0.4)

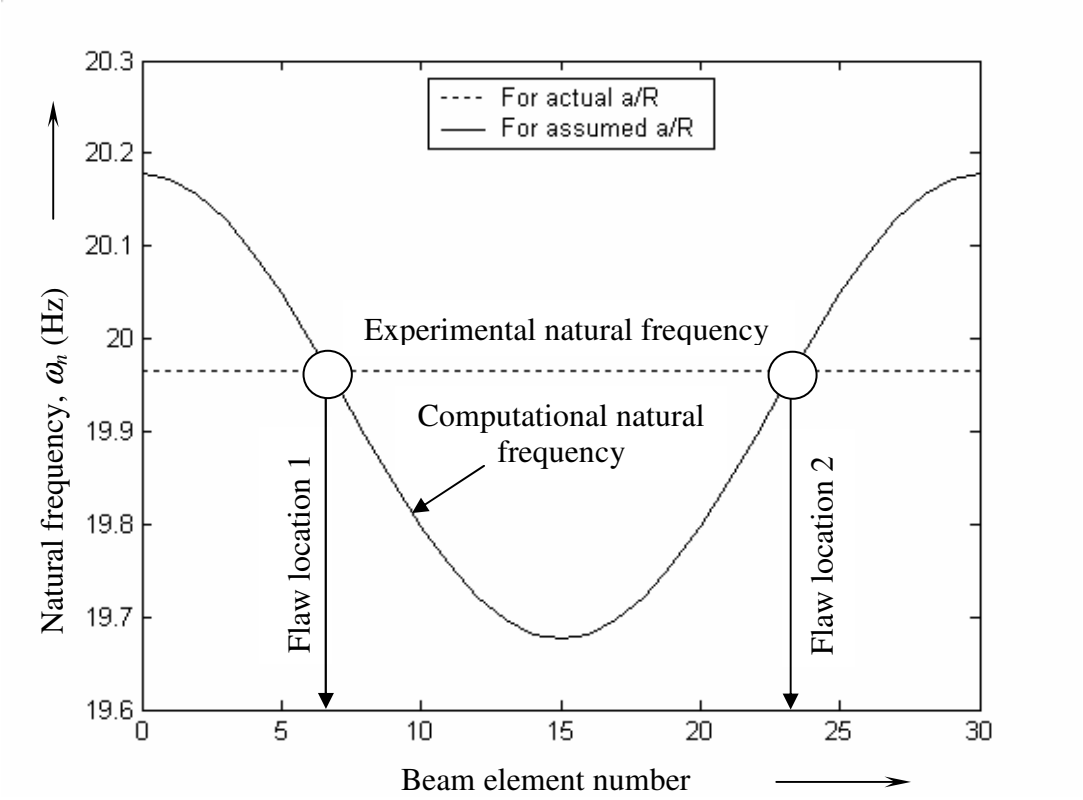

Figure 2.8 A procedure for the location of the flaw using the experimental and computational first natural frequencies

Table 2.3 Iteration details for the numerical example

Iteration no.	Initial guess for flaw depth ratio	Flaw location ratio (corresponding element no.)	Equivalent flaw depth ratio
1	0.90	0.23 (7)	0.71
2	0.71	0.40 (12)	0.71
3	0.71	0.40 (12)	0.71(converged)

The iteration is started uniformly from the first intersection of the flaw location for all cases considered in the example. The well-known fact that the detection of a flaw in a symmetric structure based on frequency measurements only is not unique. However, it is observed that the proposed algorithm is able to converge to the actual flaw location only. This result probably is a consequence of the simultaneous use the mode shape information in the second step of the procedure. Mode shapes do contain information regarding possible actual location of the flaw even in symmetrical structures in the form of distortion in mode shapes more towards the flaw location. Moreover, this is possible since our flaw localization and sizing algorithm is based on estimation of physical parameters (i.e. flaw flexibility coefficients) as against conventional methods, which uses either feature based (mode shapes, FFT, wavelets, etc.) or non-physical parameters (ARMA models, neural network etc.) based methods. The number of iterations for final convergence is very less (less than 10, however, 3 to 4 is very common). The regularization parameter η = 1100 (see equation (2.31)) is used for the above case. Table 2.4 gives comparison of theoretical and estimated flaw flexibility coefficients. Table 2.5 shows several case studies by changing the flaw location and its size in the numerical experiment.

In modeling of the flaw, the actual location of the flaw in the element is not defined from element edges; hence the flaw element number is also tabulated. For each case, the fundamental natural frequency and its percentage of reduction with that of the intact one are also provided.

To check the robustness of the present algorithm, a biased measurement error in the natural frequency and a random measurement noise in mode shapes are considered (see Tables 2.1 and 2.5), and for the case with and without damping. It could be seen that for most of the cases, the actual flaw location element number has been achieved. The flaw depth estimated from the present algorithm is quite good even with the damping, measurement error and noise effects. For undamped case, the flaw size convergences quite close to the actual size. The error in the measured natural frequency can be either positive or negative, however, in the present illustration consistently only negative error has been considered for brevity. Refer Appendix F for detailed intermediate steps involved in the proposed flaw localization and sizing algorithm.

Table 2.4 Comparison of theoretical and estimated flaw flexibility coefficients

Crack flexibility coefficients		
C's	Theoretical	Estimated
$C_{22}\,(mN^{-1})$	0.6195	0.5272
$C_{33}\,(mN^{-1})$	0.9268	0.9151
$C_{44}\,(mN^{-1})$	1.5384	1.5377
$C_{45}(=C_{54})(mN)^{-1}$	4.1109	4.1076
$C_{55}\,(mN)^{-1}$	9.0747	9.0709

Table 2.5 The assumed and estimated flaw parameters for the simply supported beam

For numerical experiment				Estimated flaw parameters from the present algorithm															
				With pure mode shapes (a)		With 1% noise in mode shapes (b)		With 5 % error in measured natural frequency (c)		With the effect of 1% damping (d)		(b) & (c)		(b) & (d)		(c) & (d)		(b), (c) and (d)	
Case	Assumed flaw parameters		ω_{nf} (Hz) and % of reduction with $\omega_{n_{in}}$	Flaw depth ratio (e)	Flaw location (beam element no.) (f)	(e)	(f)	(e)	(f)	(e)	(f)	(e)	(f)	(e)	(f)	(e)	(f)	(e)	(f)
	Flaw depth ratio	Flaw location ratio (element no.)																	
1	0.4	0.4 (12)	20.127 (0.26)	0.41	0.40 (12)	0.41	0.37 (11)	0.42	0.37 (11)	0.41	0.40 (12)	0.42	0.37 (11)	0.42	0.37 (11)	0.41	0.40 (12)	0.40	0.40 (12)
2	0.4	0.5 (15)	20.121 (0.29)	0.40	0.47 (14)	0.40	0.47 (14)	0.40	0.47 (14)	0.40	0.47 (14)	0.40	0.47 (14)	0.41	0.40 (12)	0.40	0.47 (14)	0.41	0.40 (12)
3	0.4	0.6 (18)	20.127 (0.26)	0.41	0.63 (19)	0.39	0.60 (18)	0.40	0.60 (18)	0.39	0.60 (18)	0.40	0.63 (19)	0.39	0.60 (18)	0.40	0.63 (19)	0.41	0.63 (18)
4	0.6	0.3 (9)	20.076 (0.51)	0.60	0.30 (9)	0.61	0.30 (9)	0.61	0.30 (9)	0.60	0.30 (9)	0.62	0.30 (9)	0.61	0.30 (9)	0.60	0.30 (9)	0.61	0.30 (9)
5	0.6	0.5 (15)	20.022 (0.78)	0.60	0.47 (14)	0.61	0.43 (13)	0.61	0.47 (14)	0.60	0.50 (15)	0.60	0.47 (14)	0.61	0.47 (14)	0.61	0.43 (13)	0.61	0.47 (14)
6	0.6	0.7 (21)	20.076 (0.51)	0.60	0.70 (21)	0.60	0.73 (22)	0.60	0.70 (21)	0.60	0.73 (22)	0.58	0.70 (21)	0.60	0.73 (22)	0.59	0.70 (21)	0.62	0.73 (22)
7	0.7	0.4 (12)	19.964 (1.1)	0.71	0.40 (12)	0.71	0.40 (12)	0.71	0.40 (12)	0.70	0.43 (13)	0.69	0.43 (13)	0.70	0.43 (13)	0.74	0.40 (12)	0.71	0.40 (12)
8	0.8	0.2 (6)	20.056 (0.61)	0.81	0.20 (6)	0.81	0.2 (6)	0.81	0.20 (6)	0.80	0.20 (6)	0.81	0.20 (6)	0.81	0.20 (6)	0.80	0.20 (6)	0.81	0.20 (6)
9	0.8	0.5 (15)	19.832 (1.72)	0.81	0.47 (14)	0.82	0.43 (13)	0.81	0.47 (14)	0.81	0.47 (14)	0.81	0.47 (14)	0.81	0.43 (13)	0.81	0.47 (14)	0.81	0.47 (14)
10	0.8	0.8 (24)	20.056 (0.61)	0.80	0.80 (24)	0.80	0.80 (24)	0.80	0.80 (24)	0.80	0.80 (24)	0.81	0.83 (25)	0.80	0.80 (24)	0.80	0.80 (24)	0.80	0.80 (24)

2.4.2 Cantilever beams

The free vibration study of the beam with the cantilever boundary condition has been studied. This example is provided to justify the versatility of the present algorithm to tackle different boundary conditions.

2.4.2.1 Numerical experiment for modal parameters:

Beam parameters are same as provided in Table 2.1. Now a flaw of the depth ratio $\bar{a} = 0.8$ is introduced at the flaw location ratio $\bar{x} = 0.3$ (i.e., at 9^{th} element). For these assumed parameters, the natural frequency of the cantilever beam is found to be 7.19 Hz for the case of intact beam. For the beam with flaw, the natural frequency is split into 7.11 Hz and 7.19 Hz for the flaw depth ratio, $\bar{a}$, and the flaw location, $\bar{x}$, of 0.8 and 0.3, respectively. Table 2.2 gives the splitting of natural frequencies up to second modes. Figures 2.9 and 2.10 show the first and second mode shapes, respectively, for beams without and with flaw.

2.4.2.2 Identification of flaw parameters:

The flaw localization and sizing procedure (Figure 2.4) is applied to the present example. Procedural steps similar to the previous example are not repeated here for brevity. However changes in procedural steps due to boundary conditions have been explained.

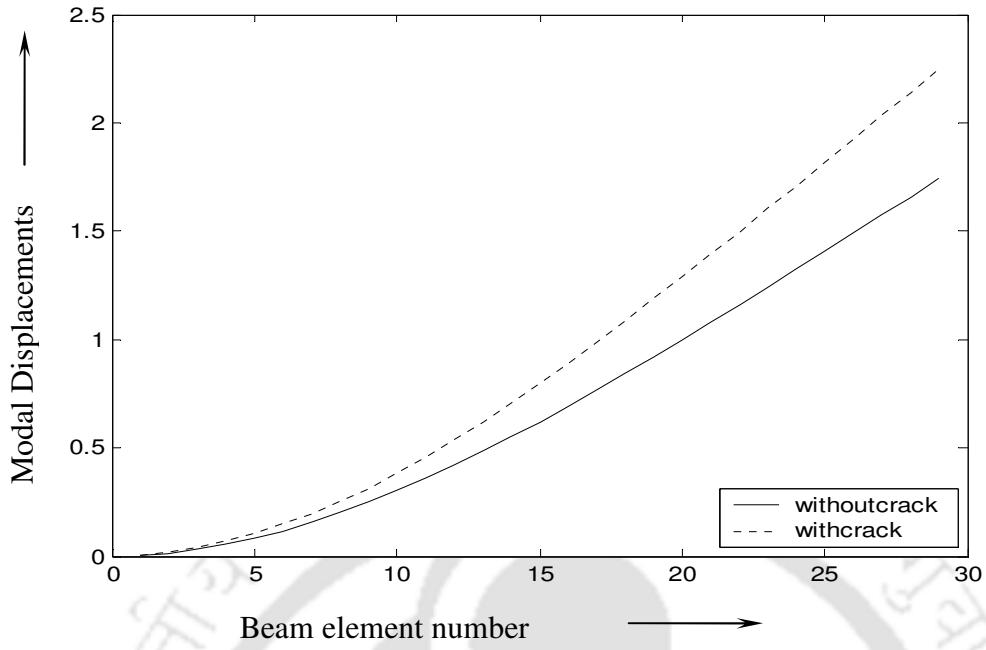

Figure 2.9 The first mode shape of beams without and with flaw for cantilever boundary conditions

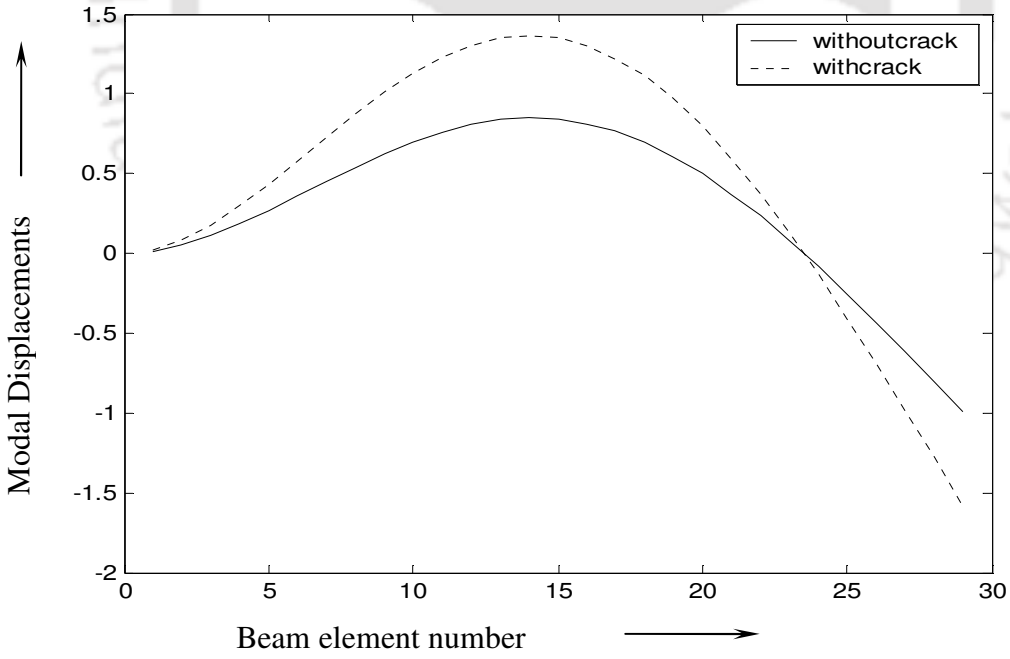

Figure 2.10 The second mode shape of beams without and with flaw for cantilever boundary conditions

Figure 2.11 shows the variation of fundamental natural frequency for different flaw depths and for various locations of the flaw for the cantilever beam. Unlike the simply supported beam with flaw, the reduction (in other words the effect of flaw) in fundamental natural frequency is more when the flaw is at the support. However, when the flaw is present at the free end, it is close to the intact case. An explicit expression of the sensitivity of a (square of a) natural frequency to an open flaw in a beam in bending vibration was derived by Morassi (1993) for a simple spring-line model of a flaw. It turns out that the sensitivity is proportional to the square of the curvature of the corresponding mode shape, evaluated for the undamaged beam at the damaged cross-section. This result explains (at least for small levels of damage) the trends found in Fig. 2.7 (i.e., the simply-supported beam) and in Fig. 2.11 (i.e., the cantilever beam). For an initially simply-supported uniform beam, the nodal points and anti-nodal points correspond to points of zero and maximum curvature, respectively.

Figure 2.12 shows the procedure of obtaining possible flaw location, from the measured and calculated natural frequencies. It can be seen that for this case only one possible flaw location is obtained for a given value of the experimental natural frequency. By applying the flaw localization and sizing procedure to the problem, the final converged flaw location and flaw size ratios are 0.30 and 0.79, respectively. The actual flaw location and flaw size ratio are 0.30 and 0.80, respectively. Table 2.6 gives the comparison of theoretical and estimated flaw flexibility coefficients. Table 2.7 shows the estimation of the flaw location and the flaw size for different cases. The flaw localization is found to be very effective and accurate in terms of the element number.

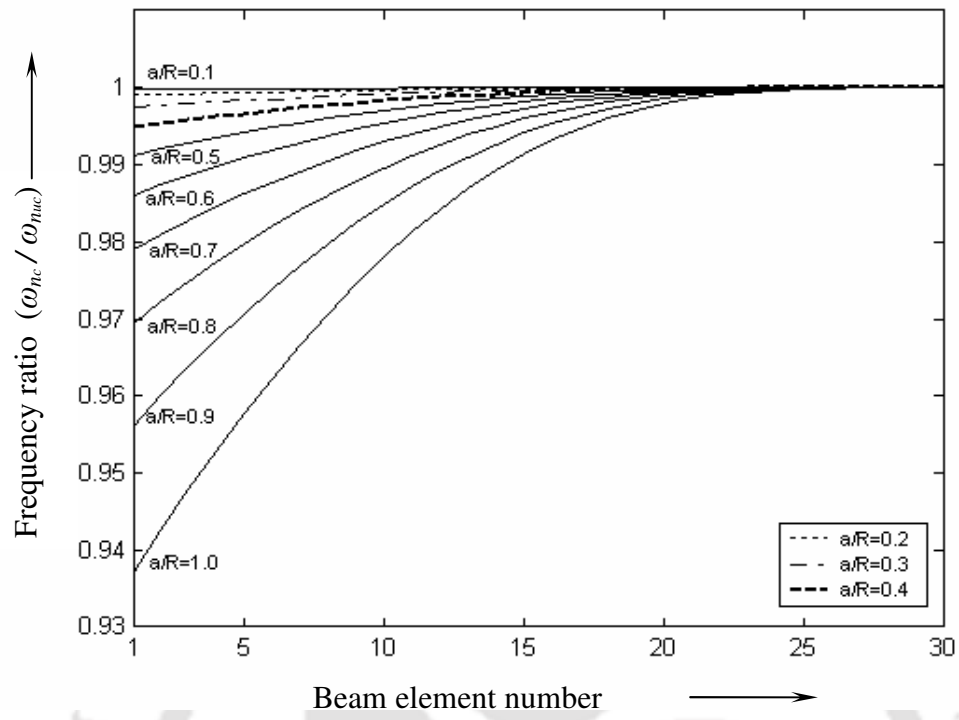

Figure 2.11 Variation of first natural frequency ratios versus flaw positions for different flaw depth ratios for the cantilever beam.

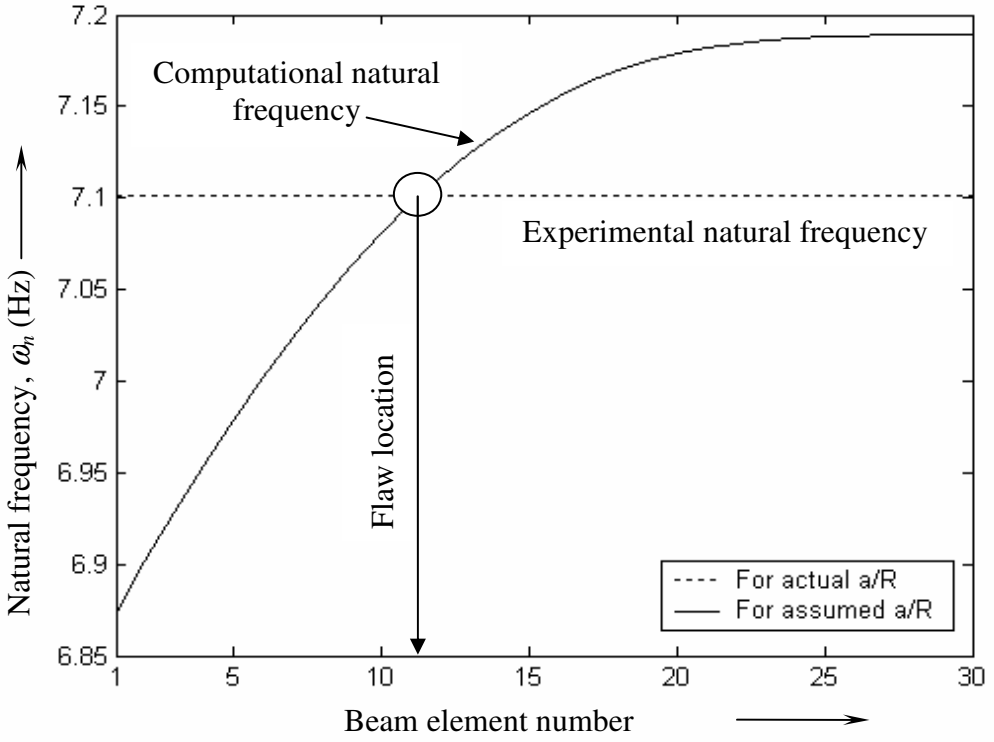

Figure 2.12 A procedure for the location of the flaw using the experimental and computational first natural frequencies for cantilever boundary conditions

Table 2.6 Comparison of theoretical and estimated flaw flexibility coefficients

Crack flexibility coefficients		
C's	Theoretical	Estimated
$C_{22}\,(mN^{-1})$	0.8375	0.8357
$C_{33}\,(mN^{-1})$	1.2536	1.2503
$C_{44}\,(mN^{-1})$	2.5950	2.5950
$C_{45}(=C_{54})(mN)^{-1}$	6.1877	6.1877
$C_{55}\,(mN)^{-1}$	12.4664	12.4664

The estimated flaw depth is found to be very good for the undamped case and fairly good with the damping effect. Table 2.7 summaries the estimation of the flaw location and the size with different measurement errors and noises also. If the beam does not have any flaw there will be no intersection of the measured natural frequency line and computational natural frequency curves as in Figure 2.8 or Figure 2.12. In this way the present algorithm distinguishes the flaw and no-flaw cases also. The required convergence is achieved even with 5 percent measurement error in the natural frequency (with respect to the change in the natural frequency due to presence of the flaw as against the intact case), and 1 percent noise in the free response with 1 percent damping effect present in the system. Higher mode natural frequency can also be used for the flaw location, however, number of possible flaw locations might be far more and the iteration time will be larger. The fundamental natural frequency suffices for the present identification method since its identification is up to the single flaw. Refer Appendix F for detailed intermediate steps involved in the proposed flaw localization and sizing algorithm.

Table 2.7 The assumed and estimated flaw parameters for the cantilever beam

For numerical experiment				Estimated flaw parameters from the present algorithm															
				With pure response (a)		With 1% noise in free response (b)		With 5 % error in $\omega_{n_{uc}}$ (c)		With the effect of 1% damping (d)		(b) & (c)		(b) & (d)		(c) & (d)		(b) , (c) and (d)	
Case	Assumed flaw parameters		ω_{nf} (Hz) and % of reduction with $\omega_{n_{in}}$	Flaw depth ratio (e)	Flaw location (element no.) (f)	(e)	(f)	(e)	(f)	(e)	(f)	(e)	(f)	(e)	(f)	(e)	(f)	(e)	(f)
	Flaw depth ratio	Flaw location ratio (element no.)																	
1	0.4	0.4 (12)	7.180 (0.140)	0.39	0.40 (12)	0.40	0.43 (13)	0.40	0.40 (12)	0.41	0.43 (13)	0.39	0.40 (12)	0.40	0.40 (12)	0.40	0.40 (12)	0.40	0.40 (12)
2	0.4	0.5 (15)	7.184 (0.084)	0.41	0.53 (16)	0.40	0.53 (16)	0.40	0.50 (15)	0.40	0.53(16)	0.40	0.50 (15)	0.40	0.50 (15)	0.42	0.53 (16)	0.39	0.50 (15)
3	0.4	0.6 (18)	7.187 (0.042)	0.40	0.60 (18)	0.39	0.60 (18)	0.40	0.60 (18)	0.41	0.63 (19)	0.40	0.60 (18)	0.40	0.60 (18)	0.39	0.60 (18)	0.39	0.60 (18)
4	0.6	0.3 (9)	7.150 (0.560)	0.59	0.30 (9)	0.60	0.30 (9)	0.60	0.30 (9)	0.60	0.30 (9)	0.59	0.30 (9)	0.60	0.33 (10)	0.60	0.30 (9)	0.60	0.30 (9)
5	0.6	0.5 (15)	7.176 (0.195)	0.59	0.50 (15)	0.59	0.50 (15)	0.60	0.50 (15)	0.60	0.50 (15)	0.60	0.50 (15)	0.60	0.50 (15)	0.59	0.50 (15)	0.61	0.53 (16)
6	0.6	0.7 (21)	7.187 (0.042)	0.59	0.70 (21)	0.60	0.70 (21)	0.60	0.73 (22)	0.60	0.70 (21)	0.61	0.73 (22)	0.59	0.70 (21)	0.61	0.73 (22)	0.60	0.70 (21)
7	0.8	0.2 (6)	7.060 (1.81)	0.80	0.20 (6)	0.80	0.20 (6)	0.80	0.20 (6)	0.80	0.20 (6)	0.80	0.23 (7)	0.79	0.20 (6)	0.80	0.20 (6)	0.80	0.20 (6)
8	0.8	0.3 (9)	7.102 (1.21)	0.79	0.30 (9)	0.80	0.33 (10)	0.78	0.30 (9)	0.79	0.30 (9)	0.80	0.30 (9)	0.79	0.30 (9)	0.80	0.33 (10)	0.80	0.30 (9)
9	0.8	0.5 (15)	7.160 (0.417)	0.80	0.50 (15)	0.80	0.50 (15)	0.78	0.50 (15)	0.79	0.50 (15)	0.82	0.50 (15)	0.80	0.50 (15)	0.80	0.50 (15)	0.81	0.53 (16)
10	0.8	0.8 (24)	7.188 (0.029)	0.79	0.80 (24)	0.80	0.80 (24)	0.80	0.80 (24)	0.80	0.83 (25)	0.80	0.80 (24)	0.80	0.80 (24)	0.80	0.80 (24)	0.79	0.80 (24)

2.5 Conclusions

A procedure for the flaw detection and localization along with the flaw parameter identification algorithm has been presented based on free vibrations. The beam has been modeled by the Euler-Bernoulli beam theory, which can be a special case of Timoshenko beam theory, for transverse loading conditions with damping effects. Regularization procedure has been incorporated in the identification algorithm for estimation of bounded flexibility coefficients. The location and the size of the flaw have been found from the measurement of natural frequencies and corresponding mode shapes. The proposed identification algorithm is an iterative procedure and has fast convergence.

Since the proposed procedure utilized FEM, it has flexibility in that; it can be utilized for the system model having general case of loadings and constraints. Numerical examples for beams with the flaw for the simply supported and cantilever boundary conditions illustrate the procedure. The procedure has been tested for robustness by introducing the random measurement noise contamination in mode shapes and the biased measurement error in natural frequencies. The present method is capable of identifying no flaw condition also, which is difficult in feature-based and non-physical parameters based identification methods.

The experimental verification of the proposed method could be a difficult task since the accurate measurement of mode shapes is difficult in practice especially near the flaw, the location of which is not known a priori. In order to avoid these difficulties, the algorithm has been modified to opt for force response measurements, which is comparatively realistic to measure and is discussed in Chapter 3.

Chapter 3

Flaw Identification Using Free and Forced Vibration Techniques

3.1 Introduction

In the present chapter, the developed algorithm for the flaw detection, localization, and sizing based on mode shapes has been improved, by using free (natural frequencies) and forced response measurements. The Timoshenko beam theory is used in the beam modeling for transverse vibrations. The FEM is used for the free and forced vibration analyses of a beam with flaw. An open transverse surface flaw is considered for the flaw model. The effect of the proportionate damping has been included. A harmonic force of known amplitude and frequency is used to dynamically excite the beam with the help of an independent exciting unit. The flaw localization and sizing algorithm is iterative in nature. The iteration starts with an initial guess for the flaw depth ratio and iteratively estimates the flaw location and depth until the desired level of convergence is achieved; for both the flaw location and depth. For estimation of bounded flexibility coefficients a regularization technique has been adopted. The method has been illustrated through numerical examples. The prediction of the flaw location and size are in good agreement even in the presence of the measurement error and noise.

3.2 System Modeling

In the present section the assumptions involved in system modeling, which is considered for development of the flaw localization and its sizing, have been presented. System equations of motion have been developed for a beam with flaw.

3.2.1 Assumptions

The Timoshenko beam theory is used for the transverse vibrations that incorporate the bending, rotary and shear deformations. In Chapter 2, the Euler-Bernoulli beam theory is used for simplicity since the focus was more towards the development of the identification method. The other assumptions in modeling the system remain same as in Subsection 2.2.1.

3.2.2 System equations of motion

The flaw model that has been discussed in Subsection 2.2.2 is used in the present section also. A beam is discretized into finite beam elements as shown in Figure 2.3 in Chapter 2. The equation of motion for the intact beam element can be written as

$$[M]^{(e)}\{\ddot{q}(t)\}^{(e)} + [D_{wf}]^{(e)}\{\dot{q}(t)\}^{(e)} + [K_{wf}]^{(e)}\{q(t)\}^{(e)} = \{f(t)\}^{(e)} \tag{3.1}$$

where $[M]^{(e)}$ is the element mass matrix, $[D_{wf}]^{(e)}$ is the element damping matrix, $[K_{wf}]^{(e)}$ is the element stiffness matrix, $\{f(t)\}^{(e)}$ is the element external force vector

and $\{q(t)\}^{(e)}$ is the element vector of nodal DOFs. Subscripts '*wf*' and '*e*' represent 'without flaw' and 'element', respectively. Details of the mass and stiffness matrices for the Timoshenko beam are given in Appendix D. The system damping has been considered as proportional (i.e., Rayleigh's) damping; hence, the damping matrix $[D_{wf}]^{(e)}$ of the intact beam element can be expressed in terms of the element mass and stiffness matrices as

$$[D_{wf}]^{(e)} = a_0[M]^{(e)} + a_1[K_{wf}]^{(e)} \tag{3.2}$$

where a_0 and a_1 are Rayleigh damping factors (expression for a_0 and a_1 are same as used in Subsection 2.2.3). The element equation of motion of a beam with flaw can be expressed as

$$[M]^{(e)}\{\ddot{q}_f(t)\}^{(e)} + [D_f]^{(e)}\{\dot{q}_f(t)\}^{(e)} + [K_f]^{(e)}\{q_f(t)\}^{(e)} = \{f(t)\}^{(e)} \tag{3.3}$$

where $\{q_f(t)\}^{(e)}$ is the nodal DOFs of the flaw element, the subscript *f* represents the *flaw*, and $[K_f]^{(e)}$ is the stiffness matrix of the beam element with flaw and it is given as

$$[K_f]^{(e)} = [T][C]^{(e)^{-1}}[T]^T \tag{3.4}$$

with

$$[C]^{(e)} = [C_o]^{(e)} + [C_f]^{(e)} \tag{3.5}$$

$$[C_o]^{(e)} = \begin{bmatrix} \frac{l}{3EI}+\frac{l}{k_{sc}AG} & 0 & 0 & \frac{l^2}{2EI} \\ 0 & \frac{l}{3EI}+\frac{l}{k_{sc}AG} & -\frac{l^2}{2EI} & 0 \\ 0 & -\frac{l^2}{2EI} & \frac{l}{EI} & 0 \\ \frac{l^2}{2EI} & 0 & 0 & \frac{l}{EI} \end{bmatrix} \tag{3.6}$$

where $[C_f]^{(e)}$ is the flexibility matrix of the flaw and it is expressed as equation (2.1), $[C]^{(e)}$ is the total flexibility matrix of the beam element with flaw, $[D_f]^{(e)}$ is the damping matrix of the beam element with flaw, $[T]$ is the transformation matrix, $[C_o]^{(e)}$ is the flexibility matrix of the intact beam element, EI is the flexural rigidity of the beam, l is the element length, A is the cross sectional area of the beam, G is the modulus of rigidity of the beam material and k_{sc} is the shear correction factor (for the present case the cross section of the beam is taken as circular). The expression for k_{sc} is given in Appendix D.

It should be noted that in the elemental mass and stiffness matrices in equation (3.3), two orthogonal plane motions (x-y and x-z) are considered. However, the corresponding expressions, which are given in Appendix C, are for one plane motion only. Hence, in equation (3.3) matrix $[K]$ must to be of dimension (8×8), accordingly equation (2.1) is expanded by employing the transformation matrix $[T]$, which is given in equation (2.9). The elemental damping matrix of beam with flaw, $[D_f]^{(e)}$, can be expressed in terms of the beam stiffness and mass element matrices with flaw, as

$$[D_f]^{(e)} = a_0[M]^{(e)} + a_1[K_f]^{(e)} \tag{3.7}$$

where Rayleigh damping factors a_0 and a_1 remain the same as in equation (3.2). It should be noted here that even damping factors are same for the beam element without and with flaw, their damping matrices are different since changes in respective stiffness matrices. Equations of motion of the complete system can be obtained by assembling contributions of elemental equations of motion without and with flaw. Then system equations of motion becomes

$$[M]\{\ddot{q}(t)\} + [D]\{\dot{q}(t)\} + [K]\{q(t)\} = \{f(t)\} \tag{3.8}$$

with

$$[D] = a_0[M] + a_1[K] \tag{3.9}$$

where $[M]$ is the assembled mass matrix, $[D]$ is the assembled damping matrix, $[K]$ is the assembled stiffness matrix, $\{F(t)\}$ is the assembled external force vector, and $\{q(t)\}$ is the assembled vector of nodal DOFs.

3.2.3 Forced vibrations

Since the harmonic excitation is considered on the beam, let the force vector be defined as

$$\{f(t)\} = \{F\}e^{j\omega t} \tag{3.10}$$

where ω is the forcing frequency, $\{F\}$ is the complex force vector (elements of which are complex quantities and contain both the amplitude and phase information) and $j = \sqrt{-1}$. Thus, the response vector can be assumed as

$$\{q(t)\} = \{Q\}e^{j\omega t} \tag{3.11}$$

where $\{Q\}$ is the complex response vector, whose elements are complex quantities. On substitution of equations (3.10) and (3.11) into equation (3.8) and applying boundary conditions, the reduced system of equations of motion become

$$\left(-\omega^2[M] + j\omega[D] + [K]\right)\{Q\} = \{F\} \tag{3.12}$$

For given system properties (i.e. $[M]$, $[D]$ and $[K]$, which includes the beam element model without and with flaw, the flaw location and its size) the response $\{Q\}$ in frequency domain can be simulated from equation (3.12) corresponding to a given force $\{F\}$. Equation (3.12) will be used in the numerical experiment for the generation of forced responses.

3.3 Flaw Localization and Sizing Algorithms

In this section the identification algorithm for the flaw sizing based on forced response measurements has been developed. The flaw detection, localization and

sizing procedure based on the free and forced response measurements have been explained.

3.3.1 Identification algorithm for the flaw sizing

The identification of flaw parameters for a known location of the flaw was developed by Dharamaraju et al. (2004), using the Euler-Bernoulli beam theory without considering the effects of damping. In the present work, the algorithm has been further refined by using the Timoshenko beam theory with considering the damping effects also. The flaw parameters such as flaw flexibility coefficients and the equivalent flaw depth ratio have been estimated along with the flaw location.

On substituting equations (2.15) and (2.17) into equation (3.12) the resulting equation, after rearranging, becomes

$$[K_f]\{Q\} = \{\hat{F}\} \tag{3.13}$$

with

$$\left\{\hat{F}\right\} = \frac{1}{(1+\mathrm{j}\omega a_1)}\left[\{F\} - \left(-\omega^2[M] + \mathrm{j}\omega\left(a_o[M] + a_1[K_{wf}]\right) + [K_{wf}]\right)\{Q\}\right] \tag{3.14}$$

Since the matrix $[K_f]$ is of the same size as the reduced assembled stiffness matrix $[K]$ in equation (3.12) and it contains non-zero terms only corresponding to the flaw nodal DOFs $\left\{Q_f\right\}^{(e)}$. Thus, equation (3.13) can be reduced to the following form

$$[K_f]^{(e)}\{Q_f\}^{(e)} = \{\hat{F}_f\} \tag{3.15}$$

where $\{\hat{F}_f\}$ contains force vector elements only corresponding to beam element with flaw nodal DOFs $\{Q_f\}^{(e)}$ from the assembled force vector $\{F\}$ defined by equation (3.14). Equation (3.15) can be used to obtain the unknown flexibility coefficients contained in the matrix $[K_f]^{(e)}$, which in turn will be used to obtain the equivalent flaw depth. Since the beam element with flaw damping is considered proportional to the mass and stiffness matrices of the beam element with flaw (i.e., equation (3.9)), the damping matrix of the beam element with flaw will also be known as a by-product, once we estimate flexibility coefficients of the flaw.

By applying similar steps which has been described in Subsection 2.3.1, equation (3.15) can be rearranged in the standard regression equation as

$$[S]\{C\} = \{B_2\} \tag{3.16}$$

with

$$[S] = \begin{bmatrix} A_{l_1} & 0 & 0 & 0 & 0 \\ 0 & A_{l_2} & 0 & 0 & 0 \\ 0 & 0 & A_{l_3} & A_{l_4} & 0 \\ 0 & 0 & 0 & A_{l_3} & A_{l_4} \end{bmatrix} \tag{3.17}$$

and

$$\{C\} = \{C_{22} \quad C_{33} \quad C_{44} \quad C_{45} \quad C_{55}\}^T \tag{3.18}$$

In equation (3.16), the vector $\{C\}$ contains all unknown flaw flexibility coefficients as given in equation (3.18). The matrix $[S]$ and the vector $\{B_2\}$ contain all known information i.e. the intact beam model, the flaw location, the force and the corresponding response. Equation (3.16) contains four equations with five unknown flaw flexibility coefficients; hence it is an underdetermined system of equations. Since flaw flexibility coefficients do not change with the change in forcing frequency, by taking responses at minimum two different forcing frequencies we can have eight equations to solve for five unknowns. Then the system of equation will be an over determined which could be solved using the normal least squares method.

3.3.2 Detection, localization and sizing algorithms

The equivalent flaw depth ratio is obtained from equation (2.30), while the location of the flaw is known. However, in practice usually the location of the flaw will be unknown. Hence, it will be of more practical importance if the position of the flaw can also be identified along with the flaw size. For the localization and the sizing of the flaw based of the free and forced vibration data, an iterative algorithm has been applied similar to as described in Subsection 2.3.3. Experimentally measured transverse natural frequency and steady state forced response due to the harmonic excitation have been used to iteratively to obtain the flaw location and the size.

3.4 Numerical Examples

The present modified algorithm based on the fundamental natural frequency and forced responses for the flaw localization and the sizing has been tested using numerical simulations for beams with two types of boundary conditions, namely, the simply supported and the cantilevered. For numerical examples, parameters of the beam are taken same as given in Table 2.1 and forcing parameters are given as: the unbalance mass of 0.002 kg and the excitation frequency range of 0-90 Hz.

The present identification algorithm needs experimental measurements of the fundamental natural frequency and forced responses due to the sinusoidal force in the system. To mimic the actual experimentation a deliberate flaw is introduced in the numerical model of the beam with a known flaw location and size for generating the natural frequency and forced responses. This numerically generated information are fed to the flaw localization and sizing algorithm as discussed in Subsection 3.3.2 to extract back the location and the size of the flaw to test the developed algorithm. The measurement error is introduced in the natural frequency and the measurement noise is introduced in forced responses to check the robustness of the present algorithm. Regularization technique, which is described in Subsection 2.3.2, is used throughout the numerical examples.

3.4.1 Simply supported beams

3.4.1.1 Numerical experiment for the response generation:

To generate the experimentally measured free and forced responses, which is required for testing the developed identification algorithm to estimate the flaw location and its size, a numerical experimentation is performed.

For the given beam parameters, the fundamental natural frequency of the intact beam simply-supported is obtained by using standard eigen value formulation (i.e., equation (2.14) with matrices corresponding to the Timoshenko beam) and is found to be 20.18 Hz. It should be noted that for the present analysis both orthogonal plane motions is considered and for the intact beam the motion in these planes are uncoupled. Hence, natural frequencies corresponding to orthogonal planes are same. Now a flaw of the depth ratio $\bar{a} = 0.7$ is introduced at the flaw location ratio $\bar{x} = 0.4$ (i.e., 12^{th} element). The fundamental natural frequency is found to reduce to 19.96 Hz. In the presence of flaw, orthogonal plane motions get coupled due to cross-coupled flexibility coefficients (i.e., c_{45} in equation (2.1)) of the flaw. It will be shown in subsequent illustrations that in the presence of flaw, there is splitting of natural frequency and we have considered only the lowest natural frequency. This frequency is considered as experimentally measured natural frequency to be used in the identification algorithm for finding the location for the flaw.

For a known sinusoidal force and with the help of equations of motion in frequency domain (i.e., equation (3.12)) forced responses are generated, initially, for

undamped case. Figure 3.1 shows variation of the amplitude and phase responses versus excitation frequencies for the beam with flaw in the vertical plane without the effect of damping. This shows the splitting of natural frequencies (i.e., in the amplitude plot in the form of peaks and in the phase plot in the form of sudden change in phase of the order of 180^0) while a flaw is introduced in the beam. Figure 3.2 gives the similar variation with damping in the system; however, they do not have sharp peaks due to damping effects. Table 3.1 shows the first and second natural frequencies for beams without and with flaw. The undamped and damped forced responses will be treated as measured responses to be used in the identification algorithm.

Table 3.1 Natural frequencies of beams without and with flaw for the simply supported and cantilever boundary conditions

Mode no.	Resonance frequencies (Hz)			
	Simply supported boundary conditions		Cantilever boundary conditions	
	Intact beam	Beam with flaw	Intact beam	Beam with flaw
1	20.18	19.96	7.19	7.10
	20.18	20.18	7.19	7.19
2	80.68	80.36	45.04	44.88
	80.68	80.68	45.04	45.04

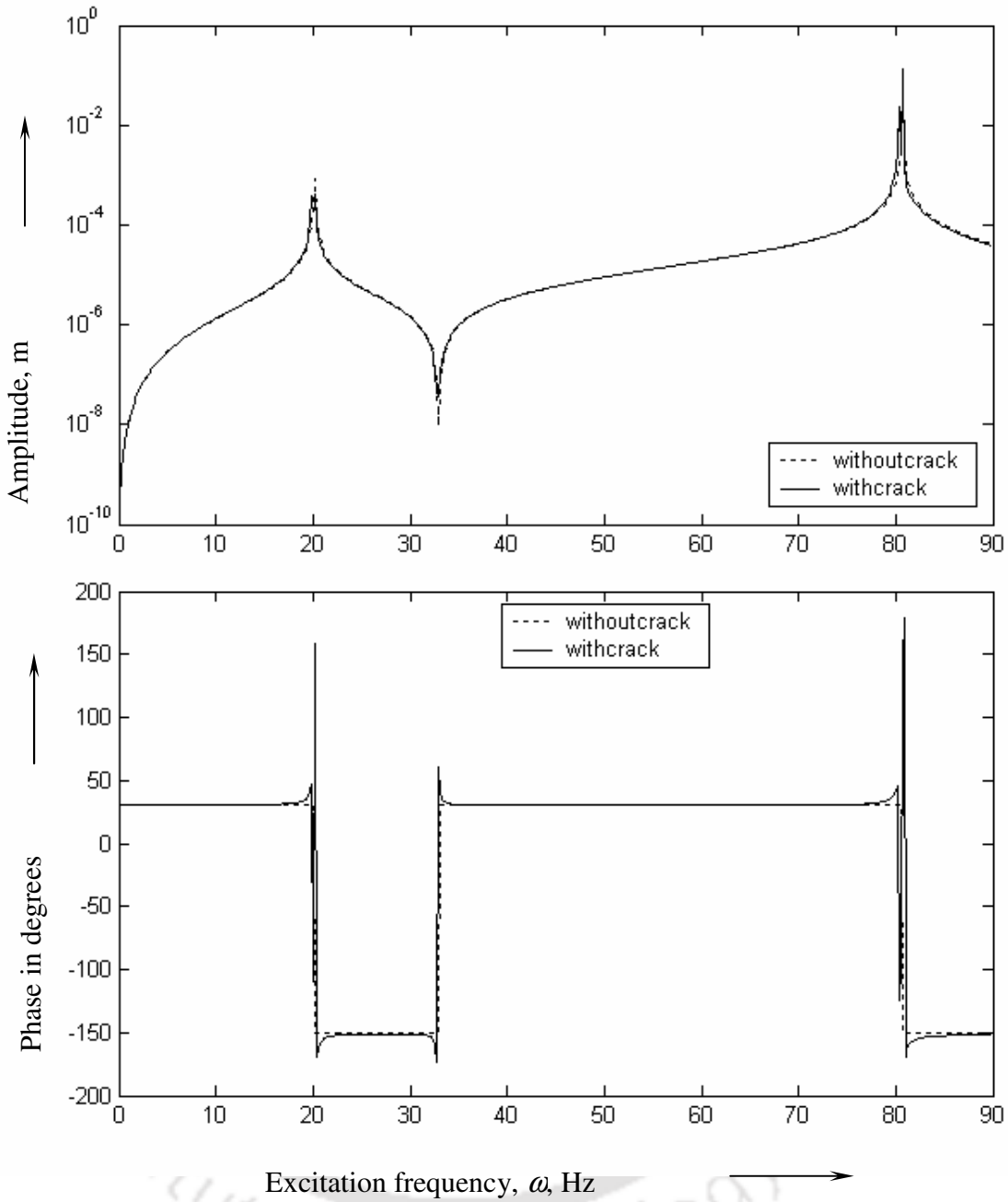

Figure 3.1 Variation of displacement (a) amplitudes and (b) phases with excitation frequencies in vertical plane (without damping) in a simply supported beam

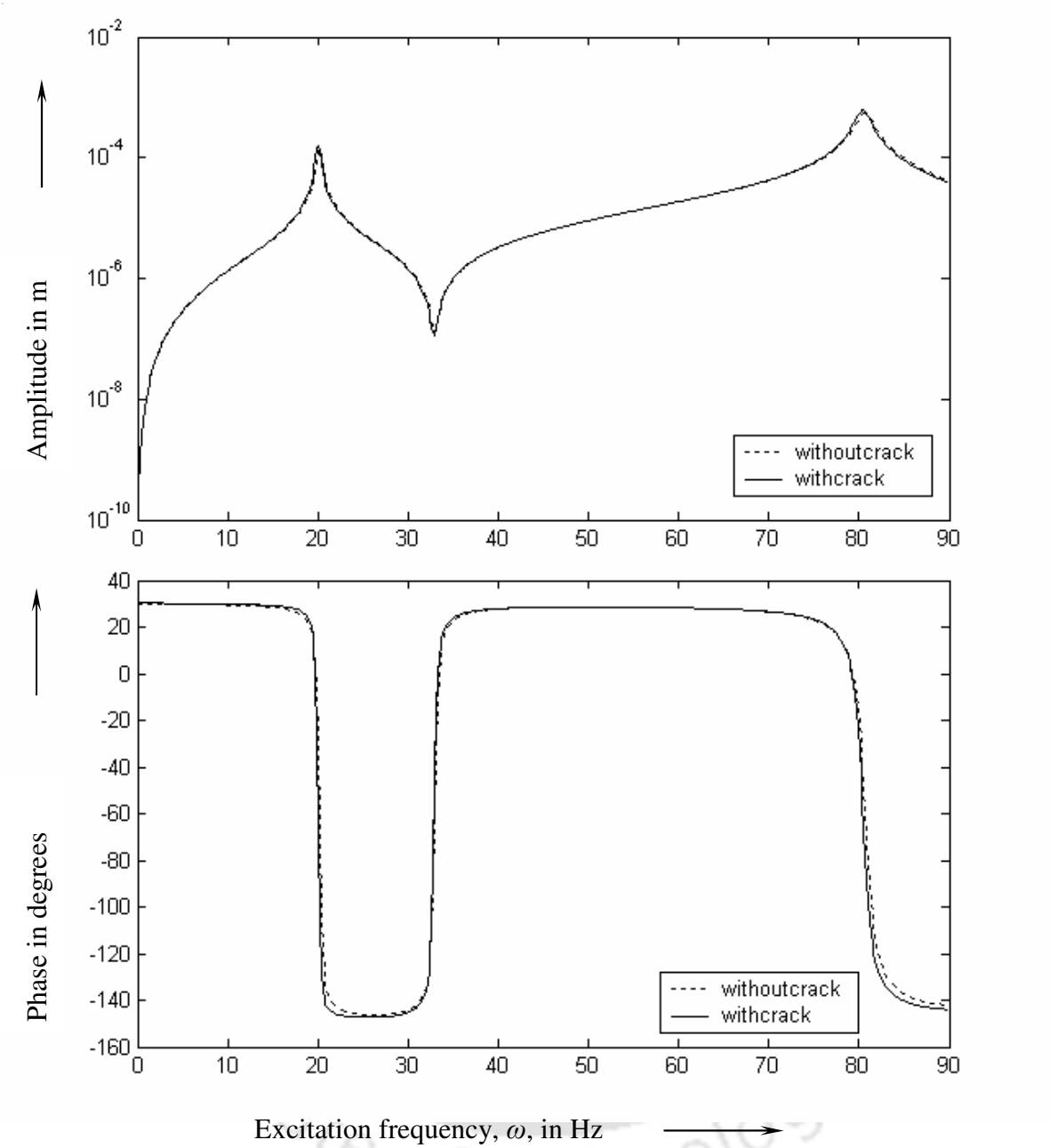

Figure 3.2 Variation of displacement (a) amplitudes and (b) phases with excitation frequencies in vertical plane (with damping) in a simply supported beam

3.4.1.2 Identification of flaw parameters:

The identification of the flaw has two basic parts, namely, first the flaw localization and secondly the flaw sizing, however, both has to be estimated iteratively for their convergence.

The variation of natural frequency ratio (i.e., ratio of beam natural frequencies with and without flaw, $\omega_{n_f} / \omega_{n_{in}}$) is obtained from the finite element analysis (i.e., of the form of equation (2.14)) of the experimental setup configuration with different possible flaw location (i.e., in element numbers 1 to 30, alternatively) for various chosen flaw depth ratio (0.1 to 1.0 in steps of 0.1). Figure 3.3 shows such a variation of natural frequencies with various possible flaw locations and for different chosen flaw sizes. It could be used to obtain the flaw location with the help of measured natural frequency.

The procedure shown in Figure 2.8 for finding the flaw location remains the same, however, it will be for the Timoshenko beam. The convergence criteria adopted here is that the difference between flaw depth ratios of two consecutive iterations should be less than 1×10^{-2}. Table 3.2 shows typical convergence steps for the present algorithm and it can be seen that the flaw location converges to the actual flaw (i.e., at $\bar{x}$ = 0.4). The number of iterations for final convergence is very less for the present case also (i.e., less than 10, however, 3 to 4 is very common). The regularization parameter η = 1 is used for the above case.

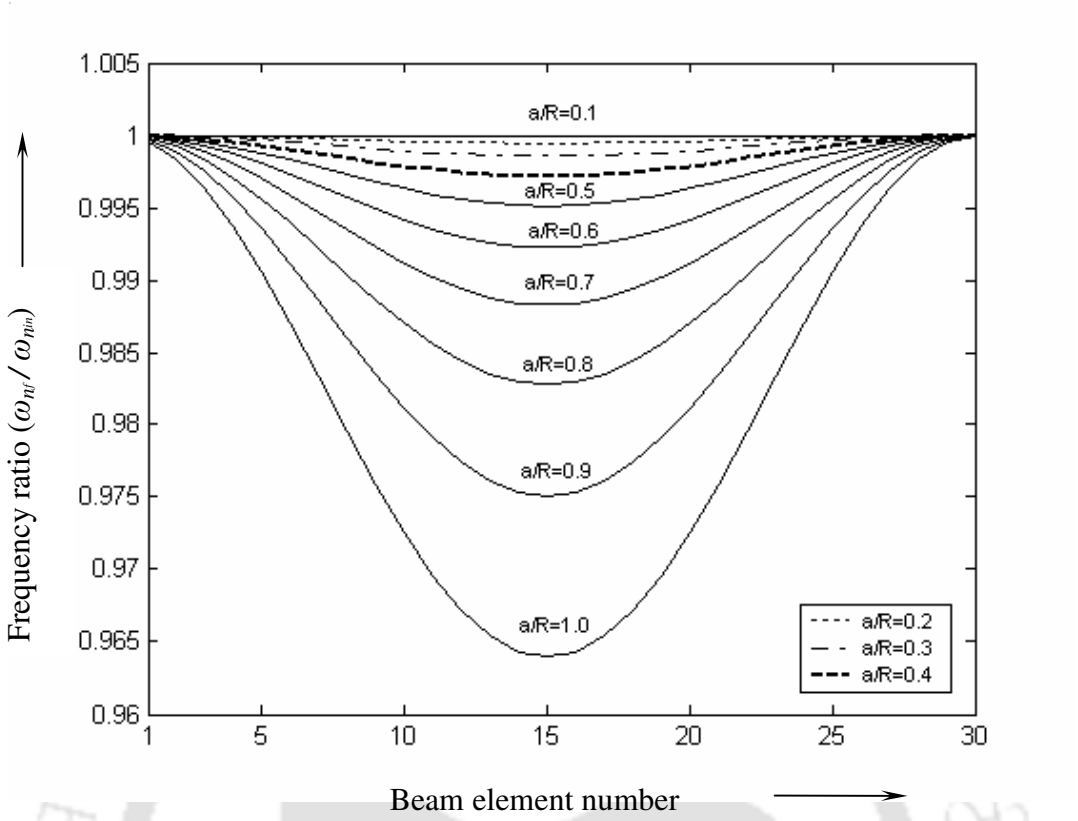

Figure 3.3 Variation of first natural frequency ratios versus flaw positions for different flaw depth ratios in the case of the simply supported beam

Table 3.3 shows several case studies by changing the flaw location and its size in the numerical experiment. In modeling of the flaw, the actual location of the flaw in the element is not defined from element edges; hence the flaw element number is also tabulated. For each case, the fundamental natural frequency and its percentage of reduction with that of the intact beam are also provided. To check the robustness of the present algorithm, the measurement error in the natural frequency and measurement noise in the forced responses are considered, without and with the damping. It can be seen that for most cases, the element number of the actual flaw location is achieved. The flaw depth estimated from the present algorithm is quite good even with the damping, measurement errors, and noise effects. For the undamped case, the flaw size convergence quite close to the actual size.

Table 3.2 Iteration details for a typical numerical example

Iteration no	Initial guess for flaw depth ratio	Flaw location ratio (element no.)	Equivalent flaw depth ratio
1	0.90	0.23 (7)	0.86
2	0.86	0.27 (8)	0.82
3	0.82	0.3 (9)	0.78
4	0.78	0.3 (9)	0.75
5	0.75	0.33 (10)	0.72
6	0.72	0.4 (12)	0.72
7	0.72	0.4 (12)	0.72 (converged)

Refer Appendix F for detailed intermediate steps involved in the proposed flaw localization and sizing algorithm.

Table 3.3 The assumed and estimated flaw parameters for the simply supported beam

For numerical experiment					Estimated flaw parameters from the present algorithm															
					With pure response (a)		With 1% noise in forced response (b)		With 5 % error in $\omega_{n_{uc}}$ (c)		With the effect of 1% damping (d)		(b) & (c)		(b) & (d)		(c) & (d)		(b), (c) and (d)	
Case	Assumed flaw parameters			ω_{nf} (Hz) and % of reduction with $\omega_{n_{in}}$	Flaw depth ratio (e)	Flaw location (element no.) (f)	(e)	(f)	(e)	(f)	(e)	(f)	(e)	(f)	(e)	(f)	(e)	(f)	(e)	(f)
	Flaw depth ratio	Flaw location ratio	Flaw element no.																	
1	0.4	0.4	12	20.127 (0.26)	0.41	0.40 (12)	0.40	0.40 (12)	0.41	0.40 (12)	0.40	0.40 (12)	0.46	0.33 (10)	0.40	0.40 (12)	0.42	0.37 (11)	0.42	0.40 (12)
2	0.4	0.5	15	20.121 (0.29)	0.40	0.50 (15)	0.40	0.47 (14)	0.41	0.50 (15)	0.40	0.50 (15)	0.40	0.47 (15)	0.40	0.50 (15)	0.41	0.47 (14)	0.41	0.47 (14)
3	0.4	0.6	18	20.127 (0.26)	0.40	0.60 (18)	0.39	0.60 (18)	0.40	0.60 (18)	0.41	0.60 (18)	0.41	0.63 (19)	0.40	0.60 (18)	0.42	0.63 (19)	0.40	0.6 (18)
4	0.6	0.3	9	20.076 (0.51)	0.62	0.30 (9)	0.61	0.30 (6)	0.61	0.30 (9)	0.62	0.30 (9)	0.62	0.30 (9)	0.61	0.30 (9)	0.62	0.30 (9)	0.62	0.30 (9)
5	0.6	0.5	15	20.022 (0.78)	0.60	0.50 (15)	0.60	0.5 (15)	0.60	0.47 (14)	0.60	0.50 (15)	0.61	0.47 (14)	0.60	0.50 (15)	0.61	0.47 (14)	0.61	0.47 (14)
6	0.6	0.7	21	20.076 (0.51)	0.60	0.70 (21)	0.59	0.7 (21)	0.60	0.70 (21)	0.61	0.70 (21)	0.62	0.73 (22)	0.59	0.70 (21)	0.64	0.73 (22)	0.60	0.7 (21)
7	0.7	0.4	12	19.964 (1.1)	0.72	0.40 (12)	0.71	0.40 (12)	0.74	0.37 (11)	0.74	0.37 (11)	0.70	0.43 (13)	0.71	0.40 (12)	0.74	0.37 (11)	0.71	0.40 (12)
8	0.8	0.2	6	20.056 (0.61)	0.82	0.20 (6)	0.80	0.2 (6)	0.82	0.20 (6)	0.81	0.20 (6)	0.80	0.20 (6)	0.80	0.20 (6)	0.81	0.20 (6)	0.83	0.20 (6)
9	0.8	0.5	15	19.832 (1.72)	0.80	0.50 (15)	0.80	0.50 (15)	0.81	0.50 (15)	0.80	0.50 (15)	0.82	0.43 (13)	0.80	0.50 (15)	0.81	0.47 (14)	0.81	0.50 (15)
10	0.8	0.8	24	20.056 (0.61)	0.82	0.80 (24)	0.80	0.80 (24)	0.80	0.80 (24)	0.87	0.83 (25)	0.80	0.80 (24)	0.81	0.83 (25)	0.87	0.83 (25)	0.85	0.83 (25)

3.4.2 Cantilever beams

Both the free and forced vibration studies of the beam with the cantilever boundary condition have been considered in numerical experiments. Based on the numerically generated vibration data the flaw identification algorithm has been illustrated.

3.4.2.1 Numerical experiment for the response generation:

The required beam parameters and other data are same as provided in Subsection 3.4.1.1. For the assumed parameters, the natural frequency of the intact cantilever beam is found to be 7.19 Hz. When compared to the results in Chapter 2, the change in natural frequency is not significant up to the second decimal, since the higher order effects of Timoshenko beam is not predominant because the beam is not thick for the present case. For the beam with flaw, the natural frequency is found to be 7.1 Hz; for the flaw depth ratio ($\bar{a}$) and the flaw location ratio ($\bar{x}$) of 0.8 and 0.3, respectively. Figure 3.4 shows the variation of the amplitude and phase of responses with respect to excitation frequencies with the damping of 1%. The effect of flaw can be observed from the splitting of resonance frequencies (i.e., natural frequencies) as given in Table 3.1, which is not present for the case of the intact beam.

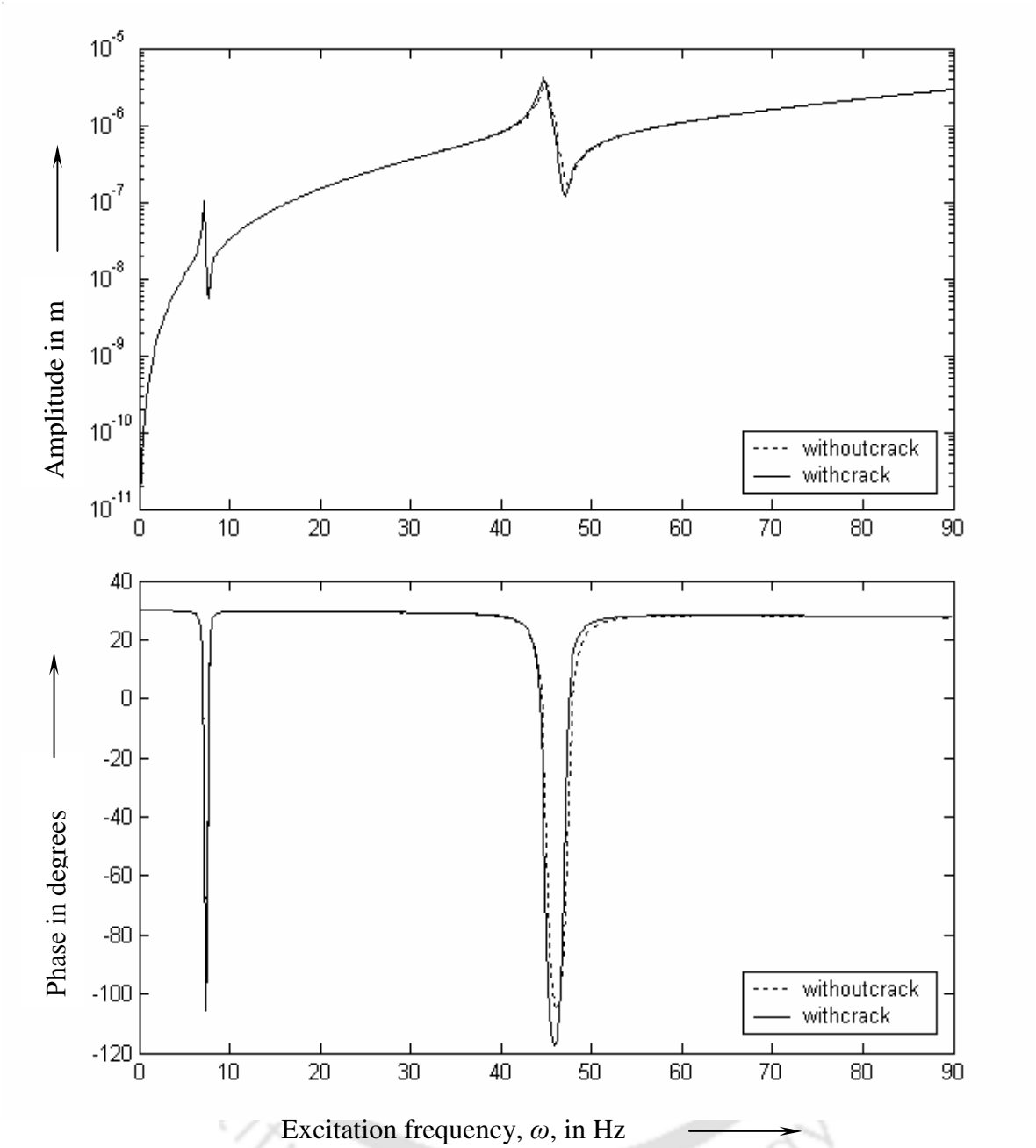

Figure 3.4 Variation of displacement (a) amplitudes and (b) phases with excitation frequencies in vertical plane (with damping) in a cantilevered beam

3.4.2.2 Identification of flaw parameters:

The flaw localization and sizing procedure (Figure 2.4) is applied to the cantilever beam as given in Subsection 3.4.1. The similar steps as described in the previous example (i.e., simply supported case) are not repeated here. However, changes due to boundary conditions have been explained. Figure 3.5 shows the variation of fundamental natural frequency for different flaw depths and for various locations of the flaw for the cantilevered beam with flaw.

Figure 2.12 shows the procedure of obtaining possible flaw location from the measured and calculated natural frequency. It can be seen that for this case only one possible flaw location is obtained for a given value of the measured natural frequency. By applying the flaw localization and sizing procedure, finally converged flaw location and flaw size are 0.33 and 0.8, respectively. There are no appreciable changes in estimation of flaw parameters with that of them based on modal parameters as given in Chapter 2. Table 3.4 shows the estimation of the flaw location and the flaw size for different cases. The flaw localization is found to be nearly same in terms of the element number. The flaw depth is found to be very good for the undamped case and good for the damping case, with the measurement error and the noise as given in Table 3.4. If the beam does not have any flaw, then there will be no intersection as in Figure 2.8 or Figure 2.12. Since presence of flaw in a structure results in decrease in the natural frequency, for the intact beam, there is no change (decrement) in the natural frequency.

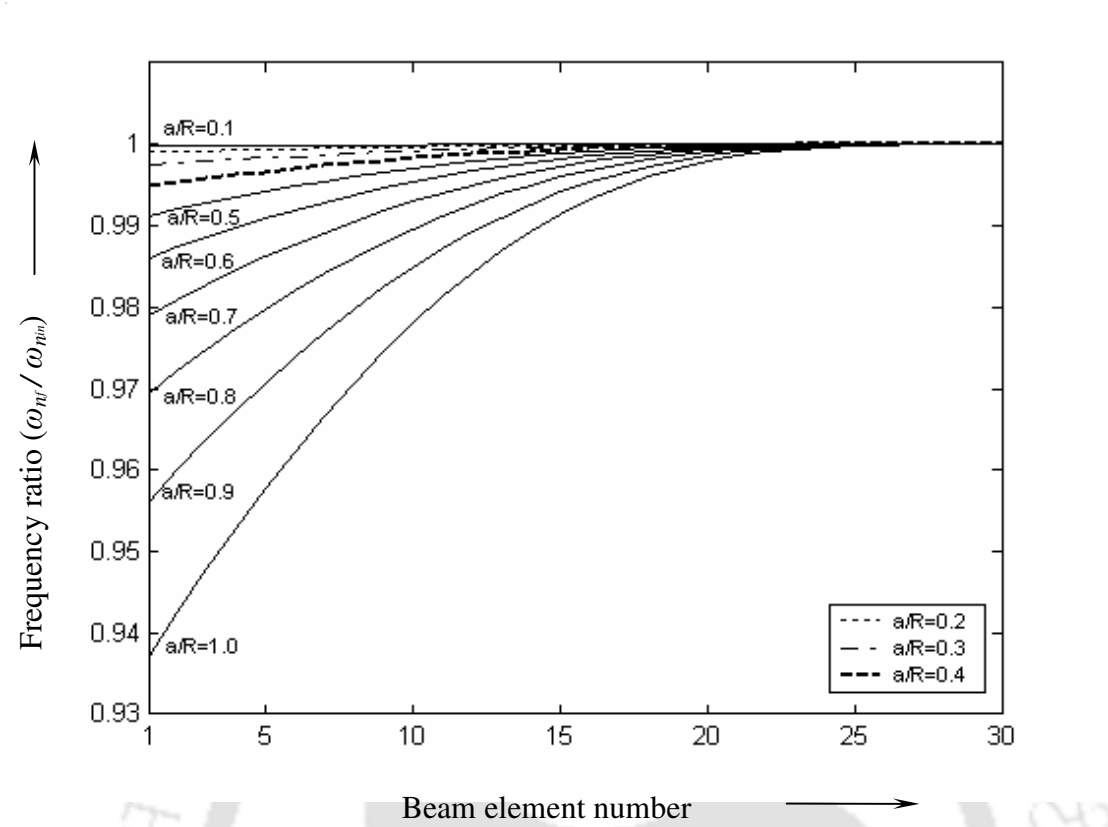

Figure 3.5 Variation of first natural frequency ratios versus flaw positions for different flaw depth ratios for the cantilever beam

In this way, the present algorithm distinguishes the beam without and with flaw cases also. The required convergence is achieved even with 5 percent measurement error in the natural frequency (with respect to the change in the natural frequency due to presence of flaw as compared to the intact beam case) and 1 percent noise in the forced response with 1 percent damping effect present in the system. Similar to Chapter 2, the fundamental natural frequency suffices for the present identification method since the identification is up to the single flaw. Refer Appendix F for detailed intermediate steps involved in the proposed flaw localization and sizing algorithm.

Table 3.4 The assumed and estimated flaw parameters for the cantilevered beam

For numerical experiment					Estimated flaw parameters from the present algorithm															
					With pure response (a)		With 1% noise in forced response (b)		With 5 % error in $\omega_{n_{uc}}$ (c)		With the effect of 1% damping (d)		(b) & (c)		(b) & (d)		(c) & (d)		(b) , (c) and (d)	
Case	Assumed flaw parameters			ω_{nf} (Hz) and % of reduction with $\omega_{n_{in}}$	Flaw depth ratio (e)	Flaw location (element no.) (f)	(e)	(f)	(e)	(f)	(e)	(f)	(e)	(f)	(e)	(f)	(e)	(f)	(e)	(f)
	Flaw depth ratio	Flaw location ratio	Flaw element no.																	
1	0.4	0.4	12	7.180 (0.140)	0.40	0.40 (12)	0.40	0.40 (12)	0.40	0.40 (12)	0.40	0.40 (12)	0.40	0.40 (12)	0.40	0.40 (12)	0.40	0.40 (12)	0.40	0.43 (13)
2	0.4	0.5	15	7.184 (0.084)	0.39	0.50 (15)	0.40	0.50 (14)	0.40	0.50 (15)	0.40	0.50 (15)	0.41	0.53 (16)	0.38	0.50 (15)	0.40	0.50 (15)	0.39	0.50 (15)
3	0.4	0.6	18	7.187 (0.042)	0.40	0.60 (18)	0.41	0.63 (19)	0.40	0.60 (18)	0.40	0.60 (18)	0.39	0.60 (18)	0.41	0.63 (19)	0.40	0.60 (18)	0.39	0.60 (18)
4	0.6	0.3	9	7.150 (0.560)	0.62	0.30 (9)	0.60	0.30 (6)	0.60	0.33 (10)	0.61	0.33 (10)	0.59	0.30 (9)	0.60	0.30 (9)	0.61	0.33 (10)	0.59	0.30 (9)
5	0.6	0.5	15	7.176 (0.195)	0.62	0.50 (15)	0.62	0.53 (16)	0.64	0.53 (16)	0.65	0.53 (16)	0.59	0.50 (15)	0.60	0.53 (16)	0.60	0.50 (15)	0.60	0.50 (15)
6	0.6	0.7	21	7.187 (0.042)	0.67	0.73 (22)	0.61	0.70 (21)	0.66	0.73 (22)	0.67	0.73 (22)	0.60	0.70 (21)	0.59	0.70 (21)	0.67	0.73 (22)	0.58	0.70 (21)
7	0.8	0.2	6	7.060 (1.81)	0.82	0.23 (7)	0.82	0.23 (7)	0.82	0.23 (7)	0.81	0.23 (7)	0.80	0.20 (6)	0.79	0.20 (6)	0.82	0.23 (7)	0.82	0.23 (7)
8	0.8	0.3	9	7.102 (1.21)	0.81	0.33 (10)	0.79	0.30 (9)	0.82	0.33 (10)	0.82	0.33 (10)	0.82	0.33 (10)	0.82	0.33 (10)	0.82	0.33 (10)	0.83	0.33 (10)
9	0.8	0.5	15	7.160 (0.417)	0.80	0.50 (15)	0.82	0.53 (16)	0.85	0.53 (16)	0.85	0.53 (16)	0.79	0.50 (15)	0.80	0.50 (15)	0.85	0.50 (15)	0.81	0.53 (16)
10	0.8	0.8	24	7.188 (0.029)	0.9	0.83 (25)	0.80	0.83 (25)	0.90	0.83 (25)	0.90	0.83 (25)	0.82	0.83 (25)	0.80	0.83 (25)	0.90	0.83 (25)	0.78	0.80 (24)

3.5 Conclusions

A detailed study of forced vibrations and a formulation for the parameter identification of the flaw has been carried out using the Timoshenko beam model. The model incorporates transverse loading conditions and the damping effect. The flaw localization and sizing algorithm is an iterative procedure and has fast convergence. Regularization procedure has been incorporated in the identification algorithm for estimation of bounded flexibility coefficients. The location and the size of the flaw have been found from the measurement of the fundamental natural frequency and force response measurements.

Numerical examples for the simply supported and cantilevered beams with flaw, illustrate the procedure. The procedure has been tested for robustness by introducing the measurement noise contamination in forced responses and the measurement error in the natural frequency. The present method is also capable of identifying no flaw condition similar to the method, which has been discussed in Chapter 2.

One of the practical difficulties of implementing the algorithm is to measure rotational DOFs especially at the flaw location, which is very difficult to measure accurately. Conventional condensation schemes (Friswell and Mottershead, 1996) fail to eliminate rotational DOFs at element with flaw for the present case, since during implementation some of the flaw flexibility parameters are getting eliminated. Hence, the difficulty in accurate measurement of rotational DOFs of forced response demands further improvement of the identification algorithm that will be dealt in the next chapter.

CHAPTER 4

FLAW IDENTIFICATION USING FORCED VIBRATION TECHNIQUES

4.1 Introduction

The practical application of the developed algorithm, which has been discussed in the Chapter 3, is improved by incorporating a novel condensation scheme along with conventional condensation schemes. Condensation schemes have been implemented in order to eliminate some of the linear DOFs and all rotational DOFs (i.e., including that of the nodes of the flaw element). The algorithm uses force-response measurements at resonance. Two parameters are required in algorithm. These are frequency at resonance and transverse linear displacements. The procedure of the flaw detection, localization and sizing is iterative and concurrent in nature. The converged value of the flaw depth and corresponding flaw location, up to a desired accuracy, is considered as the final size and the location of the actual flaw in the beam. For illustrations, beams with the simply support and cantilever end conditions have been considered. The convergence of the algorithm has been found to be very fast. The robustness of the algorithm has been tested by adding the measurement error in the resonant frequency measurement and the measurement noise in forced responses.

4.2 System Modeling

In the present section, assumptions involved in the modeling of the system under consideration are same as that of Subsection 3.2.1. In addition to the assumption of a harmonic force of known amplitude now the sine-sweep frequency is used to develop the identification algorithm based on forced response alone. The flaw model considered for development of the flaw detection, localization and its sizing and system equations of motion developed for a beam with flaw are also same as Subsection 3.2.2.

From equation (3.12) after application of boundary conditions, the reduced system of equations of motion is given as

$$\left(-\omega^2[M]+\mathrm{j}\omega[D]+[K]\right)\{Q\}=\{F\} \tag{4.1}$$

For given system properties (i.e. $[M]$, $[D]$ and $[K]$, which includes the beam element model without and with flaw, the flaw location and its size) the response $\{Q\}$ in the frequency domain can be simulated from equation (4.1) corresponding to a given force $\{F\}$. The simulated response $\{Q\}$ corresponds to the DOFs of all elements. Since only (few) transverse DOFs could be measured in practice and it is difficult to measure transverse rotational DOFs accurately. Hence, all transverse rotational DOFs (and some of linear DOFs) are condensed from the response $\{Q\}$, which is called slave DOFs.

The standard dynamic condensation could be used while development of the identification algorithm for the flaw detection, localization and sizing. However, difficulty is encountered while eliminating transverse rotational DOFs of nodes at the beam element with flaw (Tiwari and Dharmaraju, 2006). Subsequent section addresses these issues in detail during the development of the identification algorithm. Equation (4.1) would be used for generation of numerical forced responses for numerical illustrations.

4.3 Flaw localization and sizing algorithms

In this section the identification algorithm for the flaw sizing with implementation of condensation schemes has been developed. The flaw detection, localization and sizing procedure has been described based on forced response measurements.

4.3.1 Implementation of condensation schemes

Various reduction schemes (Friswell and Mottershead, 1996) have been discussed in order to eliminate DOFs, which could not be accurately measured experimentally or due to the practical constraint of number of sensors that could be used/available. Generally, these are linear DOFs corresponding to measurements other than the location of interest (excluding the beam element with flaw) and rotational DOFs (including the beam element with flaw). However, they retain linear DOFs at actual measurements (i.e. at the flaw element) locations. Dharmaraju et al. (2004) developed a flaw-sizing algorithm by using the static (Guyan) reduction scheme in which all DOFs were eliminated except at the flaw element, thus, rotational

DOFs at the flaw location could not be eliminated. In the static reduction scheme, inertia terms are neglected as compared to the stiffness terms. As the excitation frequency increases the inertia term becomes more significant. Hence, it is suitable only for low excitation frequency operations.

This was overcome by using the high-frequency reduction scheme (Dharmaraju et al., 2004). It was assumed that the stiffness term is to be negligible as contrasting to the conventional static reduction scheme. This is suitable for high operating excitation frequencies. For low or moderate excitation frequency operations stiffness terms also become significant. A hybrid reduction scheme was developed by Tiwari and Dharmaraju (2006) in order to eliminate all required slave DOFs by considering all elemental stiffness terms except that of the flaw. This is suitable for low, moderate and high excitation frequencies. However, in any of above schemes, the effect of damping has not been considered. In the present work, the hybrid reduction scheme has been extended by including proportional (i.e., Rayleigh's) damping and considering the Timoshenko beam model, while applying to the flaw sizing algorithm.

The condensation has been performed in two stages (i) the standard dynamic condensation for most of the linear DOFs and all angular DOFs, except at nodes of the beam element with flaw, and (ii) the hybrid condensation for rotational DOFs at nodes of the beam with flaw.

4.3.1.1 Dynamic condensation

In order to apply the dynamic condensation, while developing the flaw sizing identification algorithm, equation (4.1) can be rearranged as

$$\left(-\omega^2[\hat{M}]+[\hat{K}]\right)\{\hat{Q}\}=\left\{\hat{F}\right\} \tag{4.2}$$

with

$$[\hat{M}]=\left(1-\frac{\mathrm{j}a_0}{\omega}\right)[M]$$

and

$$[\hat{K}]=\left(1+\mathrm{j}\omega a_1\right)[K]$$

The mass, $[\hat{M}]$, and stiffness, $[\hat{K}]$, matrices (it should noted that these matrices are complex due to damping terms); and the response $\{\hat{Q}\}$ and force $\{\hat{F}\}$ vectors are partitioned into two parts, namely, the master and slave DOFs. Master DOFs are the ones, which are at the 'location of interest' especially considering the feasibility or accessibility through sensors and the measuring equipment requirements or availability. The DOFs other than master DOFs are treated as slave DOFs. Equation (4.2) can be partitioned into the master and slave DOFs, as

$$\left(-\omega^2[\tilde{M}]+[\tilde{K}]\right)\{\tilde{Q}\}=\left\{\tilde{F}\right\} \tag{4.3}$$

with

$$[\tilde{M}]=\begin{bmatrix}\hat{M}_{mm} & \hat{M}_{ms}\\ \hat{M}_{sm} & \hat{M}_{ss}\end{bmatrix}, \qquad [\tilde{K}]=\begin{bmatrix}\hat{K}_{mm} & \hat{K}_{ms}\\ \hat{K}_{sm} & \hat{K}_{ss}\end{bmatrix},$$

$$\{\tilde{Q}\}=\begin{Bmatrix}\hat{Q}_m\\ \hat{Q}_s\end{Bmatrix}, \qquad \text{and} \qquad \{\tilde{F}\}=\begin{Bmatrix}\hat{F}_m\\ 0\end{Bmatrix}$$

where subscripts *m* and *s* represent the *master* and *slave* DOFs. After applying the dynamic condensation (Appendix E), equation (4.3) becomes

$$\left(-\omega^2[\bar{M}^d]+[\bar{K}^d]\right)\{\bar{Q}_m\}=\{\bar{F}^d\} \tag{4.4}$$

with

$$[\bar{M}^d]=[T^d]^T[\tilde{M}][T^d], \qquad [\bar{K}^d]=[T^d]^T[\tilde{K}][T^d], \qquad \{\bar{F}^d\}=[T^d]^T\{F\},$$

and $\{\bar{Q}_m\}=[T^d]\{\hat{Q}_m\}=\{\tilde{Q}\}$

where matrices $[\bar{M}^d]$ and $[\bar{K}^d]$ are the condensed mass and stiffness matrices, respectively, (it should be noted that these matrices are complex due to damping terms) and vectors, $\{\bar{F}^d\}$ and $\{\bar{Q}_m\}$, are the condensed response and force vectors, respectively. Since the transverse rotational DOFs of the beam element with flaw have not been eliminated due to difficulties in retaining the flaw flexibility coefficients during condensation, the resulting equation (i.e., equation (4.4)) contains both the transverse linear and rotational DOFs relating to the assumed beam element

with flaw. Hence, by implementing the hybrid condensation in subsequent subsection eliminates transverse rotational DOFs of the (assumed) beam element with flaw.

4.3.1.2 *Hybrid condensation*

The hybrid condensation scheme is applied to equation (4.4) to eliminate rotational DOFs at the beam element with flaw, which is otherwise difficult by standard condensation schemes, since flaw parameters are also getting eliminated in the process.

The stiffness matrix $[\tilde{K}]$ in equation (4.4) can be split into the matrix $[\tilde{K}]_f$, which contributes nodal DOFs of the beam with flaw, and the matrix $[\tilde{K}]_{wf}$, which contributes all other elements nodal DOFs. Matrices $[\tilde{K}]_f$ and $[\tilde{K}]_{wf}$ are of the same dimensions as that of the matrix $[\tilde{K}]$. Hence, equation (4.4) can be written as

$$-\omega^2[T^d]^T[\tilde{M}][T^d]\{\bar{Q}_m\}+[T^d]^T\left([\tilde{K}]_f+[\tilde{K}]_{wf}\right)[T^d]\{\bar{Q}_m\}=\{\bar{F}^d\} \tag{4.5}$$

In this scheme, stiffness terms corresponding to the beam element with flaw are neglected as the flaw introduces considerable amount of flexibility. All other stiffness terms of the beam element with flaw are retained. It should be noted that the mass and stiffness terms are complex due to the presence of damping. Then, equation (4.5) becomes

$$-\omega^2[\bar{M}^d]\{\bar{Q}_m\}+[\bar{K}^d]_{wf}\{\bar{Q}_m\}=\{\bar{F}^d\} \tag{4.6}$$

with

$$[\bar{M}^d]=[T^d]^T[\tilde{M}][T^d]$$

and

$$[\bar{K}^d]_{wf}=[T^d]^T[\tilde{K}]_{wf}[T^d]$$

In equation (4.6), matrices $[\bar{M}^d]$ and $[\bar{K}^d]_{wf}$ and vectors $\{\bar{Q}_m\}$ and $\{\bar{F}^d\}$ can be partitioned into two parts; first the translational DOFs of the assumed beam element with flaw which are treated as master DOFs, and second the rotational DOFs of the beam element with flaw which are treated as slave DOFs. Master DOFs are to be retained and slave DOFs are to be eliminated. Hence, equation (4.6) could be split as

$$-\omega^2\begin{bmatrix}\bar{M}_{mm} & \bar{M}_{ms}\\ \bar{M}_{sm} & \bar{M}_{ss}\end{bmatrix}\begin{Bmatrix}\bar{Q}_m^h\\ \bar{Q}_s^h\end{Bmatrix}+\begin{bmatrix}\bar{K}_{mm} & \bar{K}_{ms}\\ \bar{K}_{sm} & \bar{K}_{ss}\end{bmatrix}_{wf}\begin{Bmatrix}\bar{Q}_m^h\\ \bar{Q}_s^h\end{Bmatrix}=\begin{Bmatrix}\bar{F}_m^h\\ 0\end{Bmatrix} \tag{4.7}$$

After applying the hybrid condensation (detailed in Appendix E), equation (4.7) becomes

$$\left(-\omega^2[\bar{M}^h]+[\bar{K}^h]\right)\{\bar{Q}_m^h\}=\{\bar{F}^h\} \tag{4.8}$$

with

$$[\bar{M}^h]=[T^h]^T[\bar{M}^d][T^h],\qquad [\bar{K}^h]=[T^h]^T[\bar{K}^d][T^h],$$

$$\left\{\bar{F}^h\right\} = [T^h]^T \begin{Bmatrix} \bar{F}_m^h \\ 0 \end{Bmatrix}, \qquad \text{and} \qquad \begin{Bmatrix} \bar{Q}_m^h \\ \bar{Q}_s^h \end{Bmatrix} = [T^h]\left\{\bar{Q}_m^h\right\}$$

where matrices $[\bar{M}^h]$ and $[\bar{K}^h]$ are the reduced mass and stiffness matrices respectively (which are complex due to damping terms), and vectors $\left\{\bar{F}^h\right\}$ and $\{\bar{Q}_m^h\}$ are the reduced response and force vectors, respectively. Equation (4.8) now contains only the translational DOFs, of the beam element with flaw at the assumed location, in the state vector and will be used for the estimation of flaw flexibility coefficients. Equation (4.1) will be used in the numerical experiment for generation of forced responses.

4.3.2 Estimation of flaw flexibility coefficients

Flaw flexibility coefficients can be estimated from equation (4.8) (i.e., the condensed form of equation (4.1)). It can be rearranged as

$$[T^h]^T[T^d]^T \begin{bmatrix} \hat{K}_{mm} & \hat{K}_{ms} \\ \hat{K}_{sm} & \hat{K}_{ss} \end{bmatrix} [T^d][T^h]\left\{\bar{Q}_m^h\right\} = \left\{\bar{F}^h\right\} - \omega^2[\bar{M}^h]\left\{Q_m^h\right\} \tag{4.9}$$

In equation (4.9), $[T^h]$, $[T^h]^T$, $[T^d]$, and $[T^d]^T$ should have dimensional compatibility with members of $[\tilde{K}]$. Accordingly, equation (4.9) could be rearranged as

$$\begin{bmatrix} T_1^h & \vdots & T_2^h \end{bmatrix}^T \begin{bmatrix} \hat{K}_{mm} & \vdots & \hat{K}_{ms} \\ \cdots & \vdots & \cdots \\ \hat{K}_{sm} & \vdots & \hat{K}_{ss} \end{bmatrix} \begin{bmatrix} T_1^h \\ \cdots \\ T_2^h \end{bmatrix} \{\bar{Q}_m^h\} = \{\bar{F}_1^h\} \tag{4.10}$$

with

$$\{\bar{F}_1^h\} = \{\bar{F}^h\} - \omega^2 [\bar{M}^h] \{Q_m^h\} \tag{4.11}$$

Equation (4.10) can be expanded and rearranged as

$$[T_1^h]^T [\hat{K}_{mm}][T_1^h] \{Q_m^h\} = \{\bar{F}_2^h\} \tag{4.12}$$

with

$$\{\bar{F}_2^h\} = \{\bar{F}_1^h\} - \left([T_2^h]^T [\hat{K}_{sm}][T_1^h] + [T_1^h]^T [\hat{K}_{ms}][T_2^h] + [T_2^h]^T [\hat{K}_{ss}][T_2^h]\right) \{Q_m^h\} \tag{4.13}$$

The matrix, $[\hat{K}_{mm}]$, in equation (4.12) could be split into matrices $[\hat{K}_{wf}]$ and $[\hat{K}_f]$, as

$$[T_1^h]^T \left([\hat{K}_{wf}] + [\hat{K}_f]\right)[T_1^h] \{Q_m^h\} = \{\bar{F}_2^h\} \tag{4.14}$$

Subsequently, equation (4.13) can be written as

$$[T_1^h]^T [\hat{K}_f][T_1^h] \{Q_m^h\} = \{\bar{F}_2^h\} - [T_1^h]^T [\hat{K}_{wf}][T_1^h] \{Q_m^h\} \tag{4.15}$$

Substituting equations (3.4) and (3.5) into equation (4.15), it becomes

$$[T_1^h]^T [T] \left([C_0]^{(e)} + [C_c]^{(e)}\right)^{-1} [T]^T [T_1^h] \{Q_m^h\} = \{\bar{F}_3^h\} \tag{4.16}$$

Equation (4.16) could be rearranged as

$$\left([C_0]^{(e)} + [C_c]^{(e)}\right)[A_2^h]^{-1}\left\{\bar{F}_3^h\right\} = [T]^T[T_1^h]\left\{Q_m^h\right\} \tag{4.17}$$

with

$$[A_2^h] = [T_1^h]^T[T] \tag{4.18}$$

and

$$\left\{\bar{F}_3^h\right\} = \left\{\bar{F}_2^h\right\} - [T_1^h]^T[\hat{K}_{wf}][T_1^h]\left\{Q_m^h\right\} \tag{4.19}$$

Equation (4.19) can be written in a compact form as

$$[C_f]^{(e)}\{A_1^h\} = \{B_2^h\} \tag{4.20}$$

with

$$[A_1^h] = [A_2^h]^{-1}\left\{\bar{F}_3^h\right\} \tag{4.21}$$

and

$$\left\{B_2^h\right\} = [T]^T[T_1^h]\left\{Q_m^h\right\} - [C_0]^{(e)}[A_2^h]^{-1}\left\{\bar{F}_3^h\right\} \tag{4.22}$$

Noting the expression for the matrix $[C_f]^{(e)}$, equation (2.1) can be expanded as

$$\begin{bmatrix} C_{22} & 0 & 0 & 0 \\ 0 & C_{33} & 0 & 0 \\ 0 & 0 & C_{44} & C_{45} \\ 0 & 0 & C_{54} & C_{55} \end{bmatrix} \begin{Bmatrix} A^h_{l_1} \\ A^h_{l_2} \\ A^h_{l_3} \\ A^h_{l_4} \end{Bmatrix} = \begin{Bmatrix} B^h_{2_1} \\ B^h_{2_2} \\ B^h_{2_3} \\ B^h_{2_4} \end{Bmatrix} \tag{4.23}$$

Equation (4.23) can be rearranged in the standard regression form as

$$[S^h]\{C\} = \{B^h_2\} \tag{4.24}$$

with

$$[S^h] = \begin{bmatrix} A^h_{l_1} & 0 & 0 & 0 & 0 \\ 0 & A^h_{l_2} & 0 & 0 & 0 \\ 0 & 0 & A^h_{l_3} & A^h_{l_4} & 0 \\ 0 & 0 & 0 & A^h_{l_3} & A^h_{l_4} \end{bmatrix} \tag{4.25}$$

and

$$\{C\} = \{C_{22} \quad C_{33} \quad C_{44} \quad C_{45} \quad C_{55}\}^T \tag{4.26}$$

In equation (4.24), the vector $\{C\}$ contains all unknown flaw flexibility coefficients as given by equation (4.26)). The matrix $[S^h]$ and the vector $\{B^h_2\}$ contain all known information i.e. the intact beam model, the flaw location, the force, and the corresponding response.

4.3.3 Detection, localization and sizing algorithms

The equivalent flaw depth ratio was obtained from equation (2.30) from forced responses for the known location of the flaw. However, in practice usually the location of the flaw will be unknown. Hence, it will be of more practical importance if the position of the flaw can also be identified along with the flaw size. For the localization and the sizing of the flaw (which includes detection of the flaw also) based of the forced vibration data, an iterative algorithm has been applied as described in Subsection 2.3.3. Experimentally measured transverse natural frequency from resonance condition i.e. identifying the peak (or abrupt change in phase) in the steady state forced response due to the harmonic excitation will be used to iteratively to obtain the flaw location and the size.

4.4 Numerical Examples

The proposed algorithm for the flaw localization and the sizing has been tested using numerical simulations for beams with two types of boundary conditions; namely, the simply supported and the cantilevered. For numerical examples, parameters of the beam are same as given in Table 2.1 and the frequency range of 0-100 Hz of the sine-sweep excitation has been chosen such that two modes of vibration are covered and corresponding resonance frequencies are given in Table 4.1

Table 4.1 Resonance frequencies of beams without and with flaw for the simply supported and cantilever boundary conditions

Mode no.	Resonance frequencies (Hz)			
	Simply supported boundary conditions		Cantilever boundary conditions	
	Intact beam	Beam with flaw	Intact beam	Beam with flaw
1	20.18	19.96	7.19	7.10
	20.18	20.18	7.19	7.19
2	80.68	80.36	45.04	44.88
	80.68	80.68	45.04	45.04

A slow sine-sweep vibration testing is the traditional method of measurement (or analysis) of the frequency response and involves the use of a sweep oscillator to provide a sinusoidal command signal, the frequency of which is varied slowly but continuously through the range of interest. It is necessary to check that progress through the frequency range is sufficiently slow to check that steady-state response conditions are attained before measurements are made. If an excessive sweep rate is used, then distortions in the frequency response function (FRF) plot are introduced. One way of checking the suitability of a sweep rate is to make measurements at least twice; the first by sweeping up and the second time by sweeping down through the frequency range. If the similar FRF plot results in two cases, then there is a certainty that the sweep rate is not fast (Ewins, 2000).

The present identification algorithm needs force-response measurements, such as the natural frequency (obtained from the resonance condition) and transverse linear

displacements by the slow sine-sweep excitation through an external exciter. To mimic the actual experimentation, a deliberate flaw is introduced in the beam numerical model with a known flaw location and size for generating the forced responses, which is also used to get the natural frequency. This numerically generated information is fed to the present detection and identification algorithm described in Subsection 4.3.2 to extract back the location and the size of the flaw to test the developed algorithm. The measurement error is introduced in the natural frequency and the measurement noise is introduced in forced responses to check the robustness of the present algorithm. Regularization technique described in Subsection 2.3.2 is used throughout numerical examples.

4.4.1 Simply supported beams

4.4.1.1 Numerical experiment for the response generation:

To generate experimental forced responses, which is required for testing the developed identification algorithm to estimate the flaw location and its size a numerical experimentation is performed. A slow sine-sweep excitation has been applied to the system in vertical plane; however, the motion has been considered in two orthogonal planes. For the given beam parameters, the fundamental natural frequency of the simply-supported intact beam is obtained by the resonance condition from Figure 4.1 and found to be 20.18 Hz.

It should be noted that for the present analysis, both orthogonal plane motions are considered, and for the intact beam the motion in these planes are uncoupled.

Hence, natural frequencies corresponding to orthogonal planes frequencies in the vertical plane (without damping) in a simply supported beam are same.

Now a flaw of the depth ratio $\bar{a}$ = 0.7 is introduced at the flaw location ratio $\bar{x}$ = 0.4 (i.e., 12th element). The fundamental natural frequency is found to reduce to 19.96 Hz. In the presence of flaw in the beam, orthogonal plane motions get coupled due to the cross-coupled flexibility coefficient (i.e. c_{45} in equation (2.1)) of the flaw. In the presence of flaw, there is splitting of natural frequency and we have considered only the lowest frequency. This frequency is considered as measured natural frequency to be used in the identification algorithm.

For a known slow sine-sweep excitation and with the help of equations of motion in the frequency domain (i.e., equation (4.1)) forced responses are generated, initially, for undamped case. Figure 4.1 shows variation of the amplitude and phase responses versus excitation frequencies for the beam with flaw in the vertical plane without the effect of damping. This shows the splitting of natural frequencies while a flaw is introduced in the beam. The splitting of natural frequencies can be observed in the amplitude plot in the form of peaks and in the phase plot in the form of a sudden change in phase of the order of 180^0. The phase change will be a better indication of the natural frequency location apart from the peak in the amplitude. Figure 4.2 gives the similar variation of the response in the horizontal plane for the undamped case.

Figure 4.3 shows the amplitude and phase of the response in the vertical plane with the damping. There are no sharp peaks in amplitude at resonance frequencies (at both the first and second natural frequencies) due to damping effects, however there

are abrupt changes in the phase of about 180°. Table 4.1 shows resonance frequencies of a beam without and with flaw. The damped and undamped forced responses would be treated as measured responses to be used in the identification algorithm.

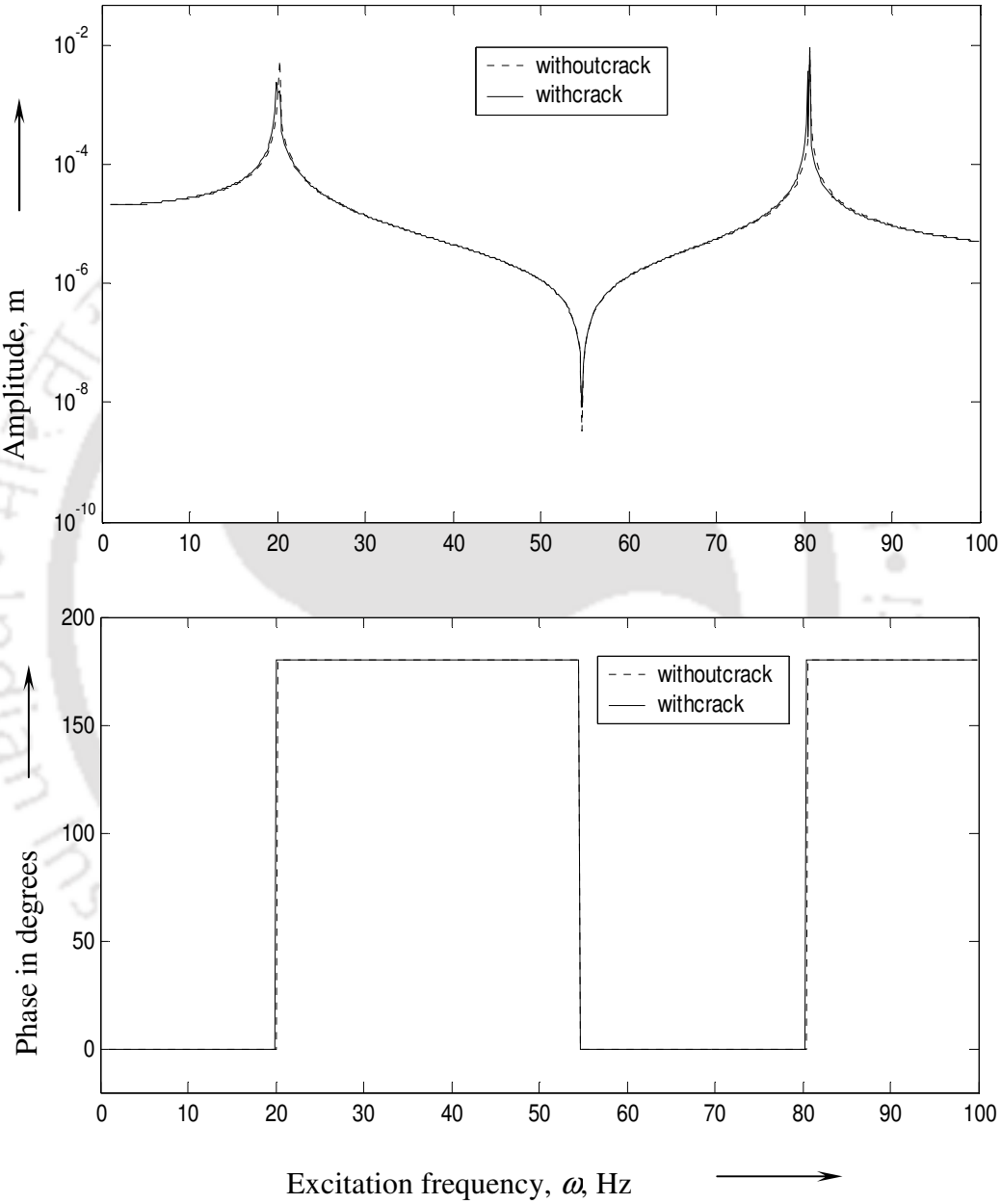

Figure 4.1 Variation of displacement (a) amplitudes and (b) phases with excitation frequencies in vertical plane (without damping) in a simply supported beam

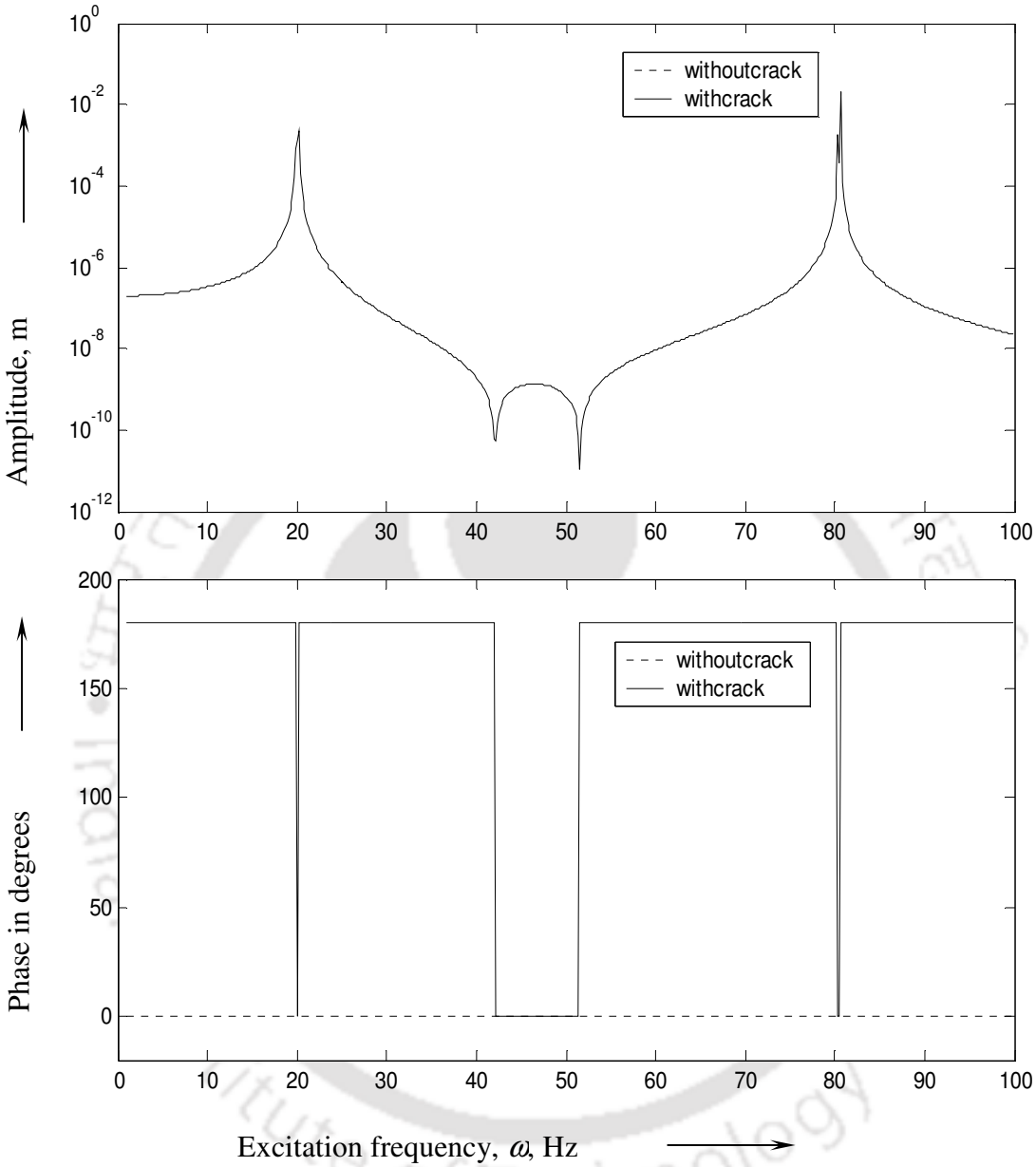

Figure 4.2 Variation of displacement (a) amplitudes and (b) phases with excitation frequencies in horizontal plane (without damping) in a simply supported beam

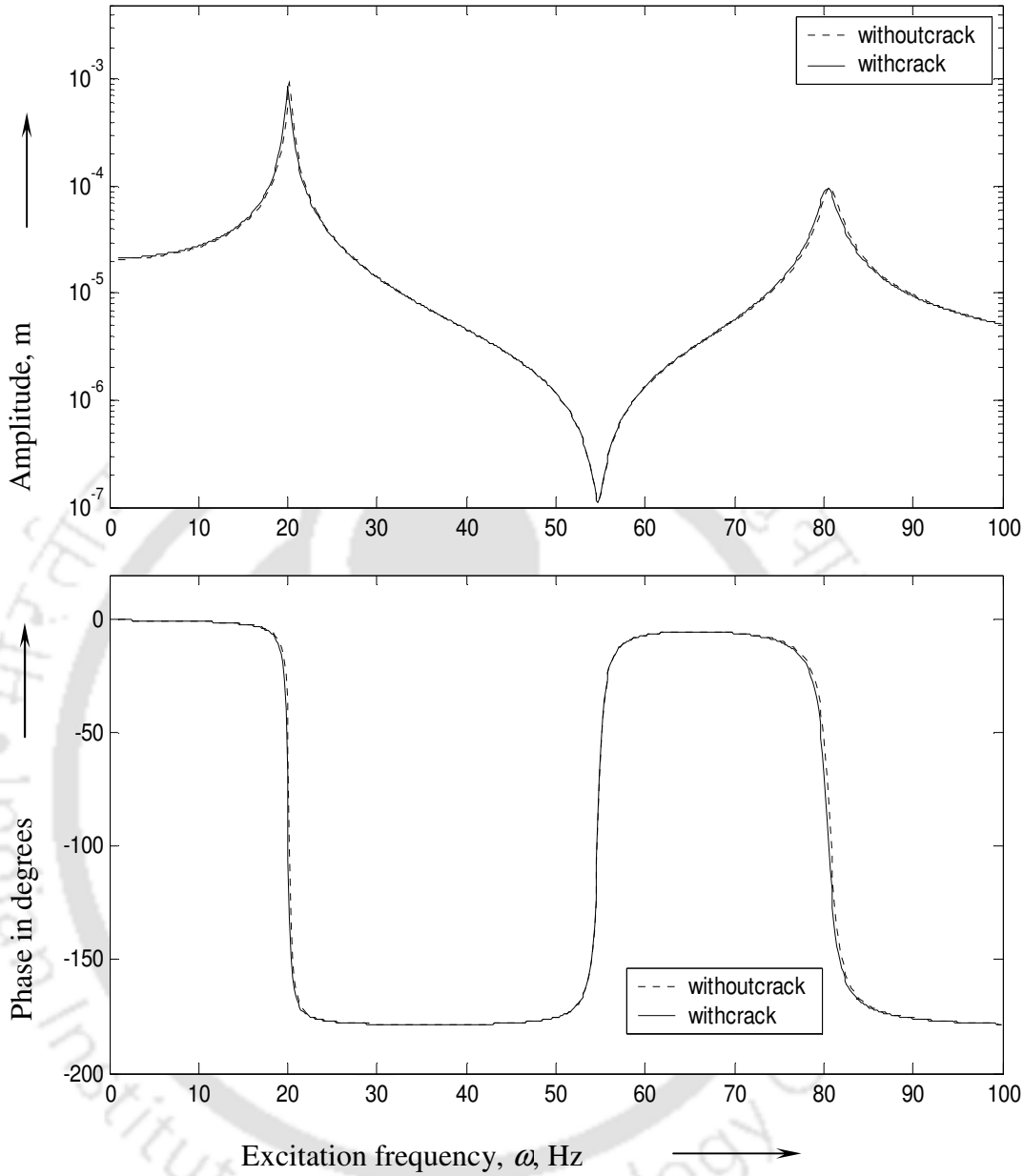

Figure 4.3 Variation of displacement (a) amplitudes and (b) phases with excitation frequencies in vertical plane (with damping) in a simply supported beam

4.4.1.2 Identification of flaw parameters:

The detection and identification has two basic parts, namely, the flaw detection and secondly localization & sizing. These parameters of the flaw have to be estimated iteratively for their convergence.

The variation of natural frequency ratio (i.e., the ratio of natural frequencies of a beam with and without flaw, $\omega_{n_f} / \omega_{n_{in}}$) is obtained from the finite element analysis (i.e., equation (2.14)) of the experimental setup configuration with different possible flaw location (i.e., in the element number from 1 to 30, alternatively) for various chosen flaw depth ratio (i.e., 0.1 to 1.0 in steps of 0.1). Figure 3.3 shows such a variation of natural frequencies with different possible flaw locations for different chosen flaw sizes, and it can be used to obtain the flaw location with the help of measured natural frequency.

Figure 2.8 (from chapter 2) shows the procedure of finding the flaw location. For the flaw localization, the flaw depth ratio is assumed initially between 0.9 and 1.0. For the initially assumed flaw depth ratio of $\bar{a}_{ig}$ = 0.9, when the natural frequency is available from measurements, it gives the initial flaw location to be 0.23 (7^{th} element). With this flaw location, flexibility coefficients of the flaw are obtained from estimation equation (4.24), and subsequently it gives equivalent flaw depth from equation (2.30). The equivalent flaw depth is used as a new flaw depth and variations of resonance frequencies are obtained by using equation (2.14) to get a new possible flaw location. The convergence criteria adopted here is that the difference between flaw depth ratios of the two consecutive iterations should be less than 1×10^{-2}. It is

illustrated in Table 4.2 with the present algorithm the flaw location converges to actual flaw location only (i.e., at $\bar{x} = 0.4$). The regularization parameter $\eta = 4.5\times10^{-5}$ is used for the above case.

Table 4.3 shows several case studies by changing the flaw location and its size in the numerical experiment. In modeling of the flaw, the actual location of the flaw in the element is not defined from element nodes; hence the flaw location corresponding to the beam element number is also tabulated. For each case the fundamental natural frequency and its percentage of reduction with that of the intact beam are also provided.

Table 4.2 Iteration details for the numerical example (simply supported end conditions)

Iteration no	Initial guess for flaw depth ratio	Flaw location ratio (element no.)	Equivalent flaw depth
1	0.90	0.23 (7)	0.77
2	0.77	0.33 (10)	0.74
3	0.74	0.37 (11)	0.72
4	0.72	0.37 (11)	0.71
5	0.71	0.40 (12)	0.71(converged)

To check the robustness of the present algorithm the measurement error in the natural frequency and the measurement noise in forced responses are considered,

without and with damping. Table 4.2 gives a typical convergence study. It can be observed that for most cases, the actual flaw location in terms of the element number is achieved and provided in Table 4.3. The flaw depth estimated from the present algorithm is quite good with the damping, measurement error and noise effects. For undamped case, the flaw size convergences quite close to the actual size. The error in the measured natural frequency could be either positive or negative, however, in the present illustration consistently negative error has been taken for brevity. Refer Appendix F for detailed intermediate steps involved in the proposed flaw localization and sizing algorithm.

Table 4.3 The assumed and estimated flaw parameters for the simply supported beam

For numerical experiment					Estimated flaw parameters from the present algorithm													
					With pure response (a)		With 1% noise in forced response (b)		With 5 % error in $\omega_{n_{uc}}$ (c)		With the effect of 1% damping (d)		(b) & (c)		(b) & (d)		(c) & (d)		(b), (c) and (d)	
Case	Assumed flaw parameters			ω_{nf} (Hz) and % of reduction with $\omega_{n_{in}}$	Flaw depth ratio (e)	Flaw location (element no.) (f)	(e)	(f)	(e)	(f)	(e)	(f)	(e)	(f)	(e)	(f)	(e)	(f)	(e)	(f)
	Flaw depth ratio	Flaw location ratio	Flaw location element no.																	
1	0.4	0.4	12	20.127 (0.26)	0.43	0.37 (11)	0.42	0.37 (11)	0.40	0.40 (12)	0.42	0.37 (11)	0.40	0.40 (12)	0.42	0.37 (11)	0.41	0.40 (12)	0.41	0.40 (12)
2	0.4	0.5	15	20.121 (0.29)	0.42	0.47 (14)	0.41	0.43 (13)	0.41	0.43 (13)	0.41	0.43 (13)	0.41	0.43 (13)	0.41	0.47 (14)	0.41	0.43 (13)	0.41	0.47 (14)
3	0.4	0.6	18	20.127 (0.26)	0.42	0.67 (20)	0.40	0.60 (18)	0.40	0.63 (19)	0.41	0.63 (19)	0.42	0.67 (20)	0.40	0.63 (19)	0.39	0.60 (18)	0.40	0.60 (18)
4	0.6	0.3	9	20.076 (0.51)	0.59	0.33 (10)	0.60	0.30 (9)	0.61	0.30 (9)	0.62	0.30 (9)	0.61	0.30 (9)	0.60	0.30 (9)	0.62	0.30 (9)	0.60	0.30 (9)
5	0.6	0.5	15	20.022 (0.78)	0.60	0.47 (14)	0.61	0.43 (13)	0.61	0.43 (13)	0.62	0.43 (13)	0.60	0.50 (15)	0.61	0.47 (14)	0.60	0.47 (14)	0.62	0.43 (13)
6	0.6	0.7	21	20.076 (0.51)	0.62	0.73 (22)	0.60	0.70 (21)	0.63	0.73 (22)	0.63	0.73 (22)	0.61	0.73 (22)	0.60	0.70 (21)	0.61	0.73 (22)	0.60	0.73 (22)
7	0.7	0.4	12	19.964 (1.1)	0.71	0.40 (12)	0.71	0.40 (12)	0.71	0.40 (12)	0.72	0.40 (12)	0.70	0.40 (12)	0.70	0.40 (12)	0.71	0.40 (12)	0.70	0.40 (12)
8	0.8	0.2	6	20.056 (0.61)	0.82	0.20 (6)	0.83	0.20 (6)	0.80	0.20 (6)	0.80	0.20 (6)	0.81	0.20 (6)	0.80	0.20 (6)	0.80	0.20 (6)	0.81	0.20 (6)
9	0.8	0.5	15	19.832 (1.72)	0.80	0.50 (15)	0.80	0.47 (14)	0.80	0.47 (14)	0.81	0.47 (14)	0.80	0.50 (15)	0.80	0.50 (15)	0.81	0.47 (14)	0.80	0.50 (15)
10	0.8	0.8	24	20.056 (0.61)	0.87	0.83 (25)	0.87	0.83 (25)	0.86	0.83 (25)	0.81	0.83 (25)	0.87	0.83 (25)	0.80	0.80 (24)	0.78	0.80 (24)	0.81	0.83 (25)

4.4.2 Cantilevered beams

This example is provided to justify the versatility of the present algorithm. Both the free and forced vibrations study of a beam with cantilevered end condition has been studied.

4.4.2.1 Numerical experiment for the response generation:

For the assumed beam parameters, the natural frequency of the intact cantilever beam is found to be 7.19 Hz for the intact beam case and there is no change with frequencies which has been estimated in Chapter 3. For the beam with flaw the natural frequency is found to be 7.1 Hz for the flaw depth ratio ($\bar{a}$) and the flaw location ($\bar{x}$) of 0.8 and 0.3, respectively and there is no appreciable change with that of them which has been discussed in Chapter 3. Figure 4.4 shows the variation of the amplitude and phase of responses with respect to excitation frequencies with the damping of 1%. The effect of flaw can be observed from the splitting of resonance frequencies (i.e. natural frequencies) as given in Table 4.1, which is not present for the case of intact beam.

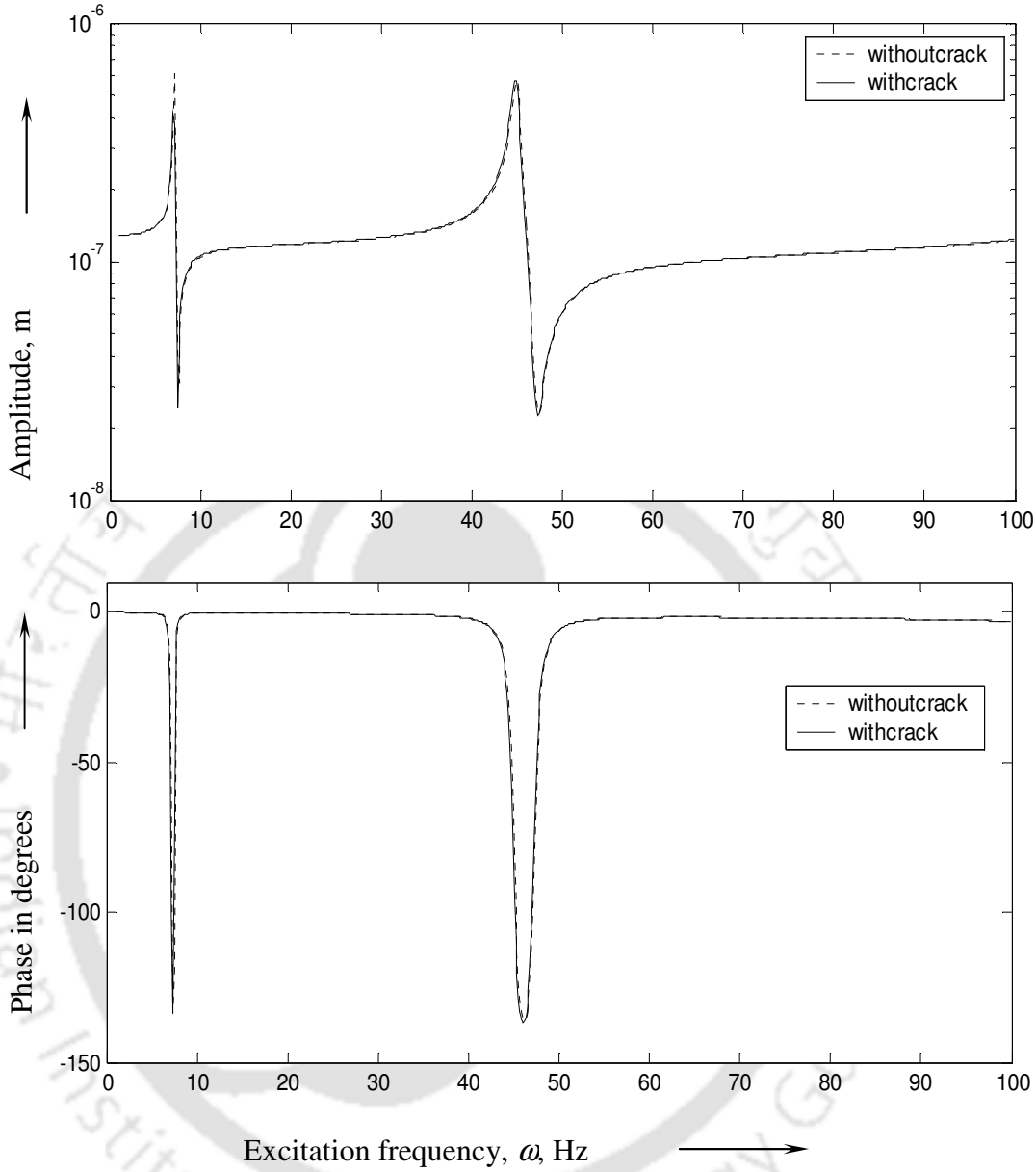

Figure 4.4 Variation of displacement (a) amplitudes and (b) phases with excitation frequencies in vertical plane (with damping) in a cantilever beam

4.4.2.2 Identification of flaw parameters:

The flaw localization and sizing procedure (Figure 2.4) is applied to this example. The similar steps as in previous example are not repeated here for brevity. However, changes due to end conditions have been explained.

The Figure 3.5 shows the variation of fundamental natural frequency for different flaw depths and for various locations of the flaw for the cantilevered beam. Unlike the simply supported beam, variations of fundamental natural frequency are more (in terms of the effect of flaw) when the flaw is at the support. However, when the flaw is present at the free end it is close to the intact beam case. Figure 2.12 shows the procedure of obtaining possible flaw location from the measured and calculated natural frequency. It can be seen that for this case only one possible flaw location is obtained for a given value of the measured natural frequency. By applying the flaw localization and sizing procedure, finally converged flaw location and flaw size are 0.30 and 0.80, respectively.

Table 4.4 shows the estimation of the flaw location and the flaw size for different cases. The flaw localization is found to be nearly same in terms of the element number. The flaw depth is found to be very good for the undamped case and good with damping, along with the measurement error and the noise as given in Table 4.4. The required convergence is achieved even with 5 percent measurement error in the natural frequency (with respect to the change in the natural frequency due to presence of flaw as compared to without flaw case) and 1 percent noise in the forced response with 1 percent damping effect present in the system. Higher natural

frequency can also be used for the flaw location, however, number of possible flaw locations will be far more and the iteration time will be larger. The fundamental natural frequency suffices for present identification method since its identification is up to the single flaw. Refer Appendix F for detailed intermediate steps involved in the proposed flaw localization and sizing algorithm.

Table 4.4 The assumed and estimated flaw parameters for the cantilever beam

For numerical experiment					Estimated flaw parameters from the present algorithm															
					With pure response (a)		With 1% noise in forced response (b)		With 5 % error $\omega_{n_{uc}}$ (c)		With the effect of 1% damping (d)		(b) & (c)		(b) & (d)		(c) & (d)		(b) , (c) and (d)	
Case	Assumed flaw parameters			ω_{nf} (Hz) and % of reduction with $\omega_{n_{in}}$	Flaw depth ratio (e)	Flaw location (element no.) (f)	(e)	(f)	(e)	(f)	(e)	(f)	(e)	(f)	(e)	(f)	(e)	(f)	(e)	(f)
	Flaw depth ratio	Flaw location ratio	Flaw location element no.																	
1	0.4	0.4	12	7.180 (0.140)	0.40	0.40 (12)	0.39	0.40 (12)	0.41	0.43 (13)	0.42	0.43 (13)	0.39	0.40 (12)	0.38	0.40 (12)	0.43	0.43 (12)	0.40	0.40 (12)
2	0.4	0.5	15	7.184 (0.084)	0.39	0.50 (15)	0.39	0.50 (15)	0.39	0.50 (15)	0.42	0.53 (16)	0.38	0.50 (15)	0.42	0.53 (16)	0.41	0.53 (16)	0.40	0.53 (16)
3	0.4	0.6	18	7.187 (0.042)	0.39	0.60 (18)	0.42	0.63 (18)	0.40	0.63 (19)	0.41	0.63 (19)	0.40	0.60 (18)	0.39	0.60 (18)	0.39	0.60 (18)	0.39	0.60 (18)
4	0.6	0.3	9	7.150 (0.560)	0.61	0.33 (10)	0.61	0.33 (10)	0.60	0.30 (9)	0.63	0.33 (10)	0.58	0.30 (9)	0.60	0.30 (9)	0.59	0.30 (9)	0.61	0.33 (10)
5	0.6	0.5	15	7.176 (0.195)	0.60	0.53 (16)	0.59	0.50 (15)	0.61	0.53 (16)	0.59	0.50 (15)	0.61	0.53 (16)	0.60	0.53 (16)	0.60	0.53 (16)	0.58	0.50 (15)
6	0.6	0.7	21	7.187 (0.042)	0.60	0.73 (22)	0.61	0.73 (22)	0.59	0.60 (21)	0.60	0.73 (21)	0.60	0.73 (21)	0.59	0.70 (21)	0.62	0.73 (22)	0.60	0.70 (21)
7	0.8	0.2	6	7.060 (1.81)	0.82	0.23 (7)	0.80	0.23 (7)	0.82	0.23 (6)	0.80	0.20 (6)	0.78	0.20 (6)	0.80	0.20 (6)	0.82	0.23 (7)	0.82	0.23 (7)
8	0.8	0.3	9	7.102 (1.21)	0.80	0.30 (9)	0.81	0.33 (10)	0.79	0.30 (9)	0.80	0.30 (9)	0.79	0.30 (9)	0.80	0.30 (9)	0.80	0.30 (9)	0.80	0.30 (9)
9	0.8	0.5	15	7.160 (0.417)	0.80	0.50 (15)	0.80	0.53 (16)	0.79	0.50 (15)	0.81	0.53 (16)	0.80	0.50 (15)	0.81	0.53 (16)	0.79	0.50 (15)	0.79	0.50 (15)
10	0.8	0.8	24	7.188 (0.029)	0.81	0.83 (25)	0.80	0.80 (24)	0.81	0.83 (25)	0.79	0.80 (24)	0.78	0.80 (24)	0.80	0.80 (24)	0.79	0.80 (24)	0.80	0.80 (24)

4.5 Conclusions

In the present chapter, a flaw detection and diagnostics identification algorithm for a beam has been developed. The Timoshenko beam model has been used in beam modeling, by incorporating transverse loading conditions and the damping effect. The main focus is to eliminate the measurement of all rotational DOFs, which otherwise difficult to measure accurately and eliminate some of the linear DOFs so that the number of sensors required could be reduced. Condensation schemes have been applied to the flaw localization and sizing algorithm in elimination of the transverse linear and rotational DOFs. The proposed algorithm is an iterative procedure and has fast convergence. Regularization procedure has been incorporated in the identification algorithm for estimation of bounded flexibility coefficients. The location and the size of the flaw have been found from the measurement of the fundamental natural frequency and force response measurements.

The proposed procedure requires only the fundamental transverse natural frequency and transverse linear displacement DOFs from forced responses, which can be easily and accurately measured with the state of the art instrumentation technology. If the number of measurements to be restricted at two locations only (because of the availability of the sensors and associated conditioning hardware) the experimentation has to be repeated by changing locations of these measurement position at various measurement points. Numerical examples for beams with the simply supported and cantilevered end conditions illustrate the procedure. The procedure has been tested for robustness by introducing the measurement noise contamination in forced responses and the measurement error in the natural frequency measurements. The present method is capable of identifying no flaw condition also, which is difficult in feature-

based and non-physical parameters based methods. The present identification algorithm overcomes the posed practical hurdles (such as the difficulty involved in accurate measurement of rotational DOFs and inaccessibility in some of linear DOFs) and reached a stage at which it could be implemented in practice.

CHAPTER 5

EXPERIMENTAL INVESTIGATION

5.1 Introduction

Experimental investigation has been carried out in the laboratory in order to validate the proposed theoretical approach for the flaw detection, localization and sizing. A model of a beam with artificially induced flaw was made and tested in vibration laboratory at IIT Guwahati. The standard impact test was conducted for the estimation of system damping ratio. In the present method, a harmonic force of continuously varying frequency was applied to excite the specimen by an independent electromagnetic exciter unit. The responses in the horizontal and vertical directions were measured at various locations of the beam with flaw by using proximity sensors. The signal output from transducers was sampled and stored in a personal computer by using a data acquisition system. The stored data were further processed to a convenient form as required by the proposed flaw identification algorithm in frequency domain. Resonant frequencies, amplitude, and phase information of responses were then fed into the algorithm for subsequent estimation of flaw parameters (i.e., the flaw location and its equivalent depth, the flaw flexibility coefficients).

5.2 Model Descriptions and Support Conditions

A beam model with flaw is shown in Figure 5.1. A mild steel beam of circular cross section with the diameter of 0.0097m and the length of 1.022m is considered. The parameters of the beam are given in Table 5.1.

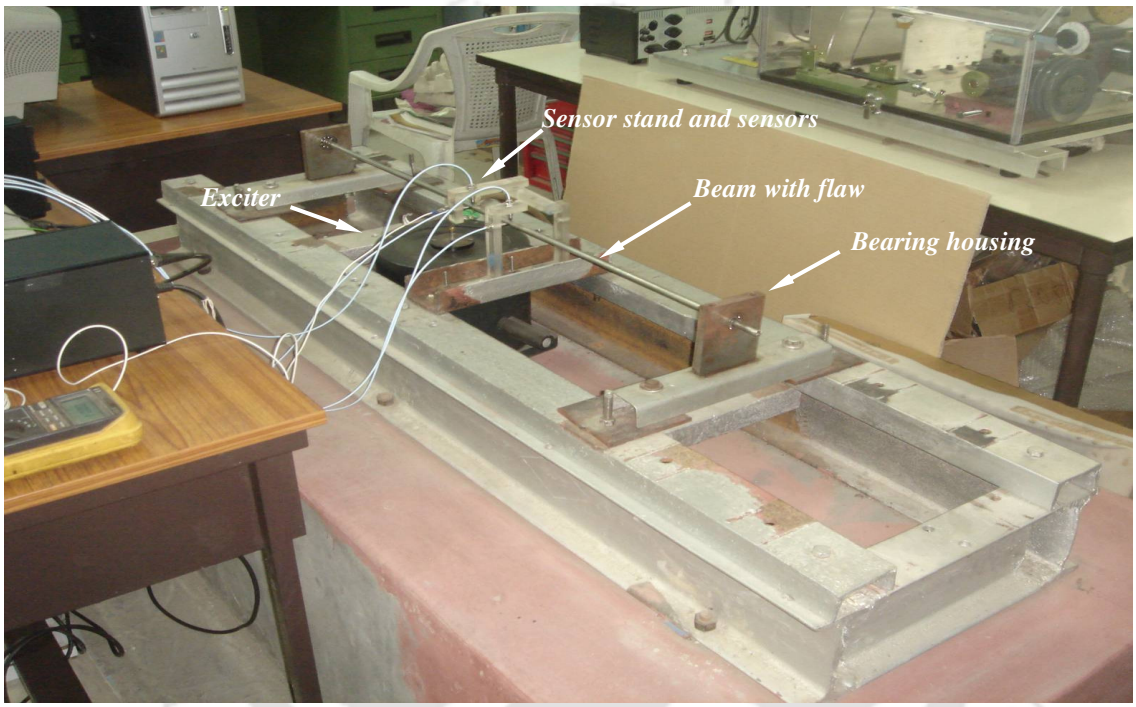

Figure 5.1 An experimental setup of a beam with flaw

The beam was supported by preloaded deep-groove ball bearings at both ends as shown in Figure 5.2. The bearings were accommodated in specially fabricated split type bearing housings (made from rectangular mild steel plates), which provided a firm support and simple means for mounting/dismounting of bearings as well as of the beam. The housings were fixed to the basement via C-channels through bolted joints, which was again fixed to long I-channels by bolted joints. Finally, the I-channels were

bolted to a heavy concrete foundation. The beam with flaw had a transversely open slit flaw (see Figure 5.3).

Table 5.1 Parameters of the beam for the experimental setup

S. No.	**Parameters**	**Values**
1	Diameter of the circular beam, D	0.0097 m
2	Beam span, L	0.941 m
3	Young's modulus of the beam material, E	2.06×10^{11} N / m^2
4	Density of the beam material, ρ	7800 kg / m^3
5	Number of beam elements, N (Both for modeling and experiment)	27
6	For beam 1 with flaw: Beam element number of the flaw (location and size, approximately)	14 (x/L = 0.5 and a/R = 0.41)
7	For beam 2 with flaw: Beam element number of the flaw (location and size, approximately)	9 (x/L = 0.3 and a/R = 0.72)

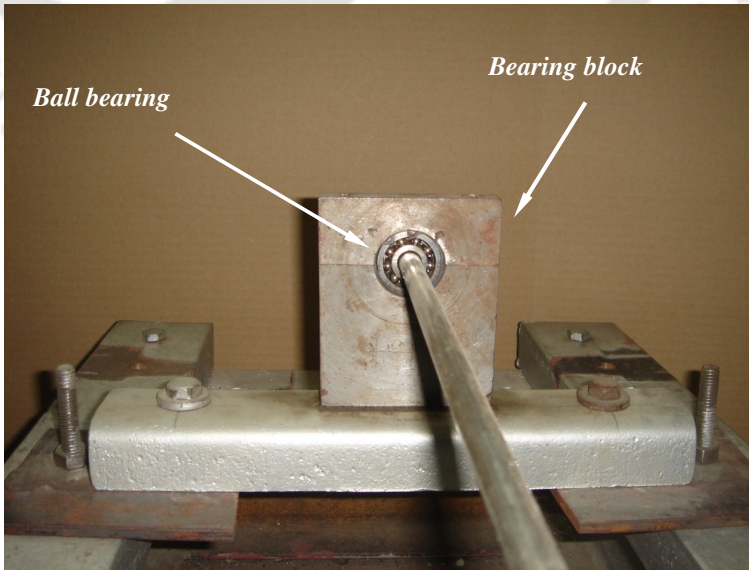

Figure 5.2 Close view of a beam supported on rolling bearings

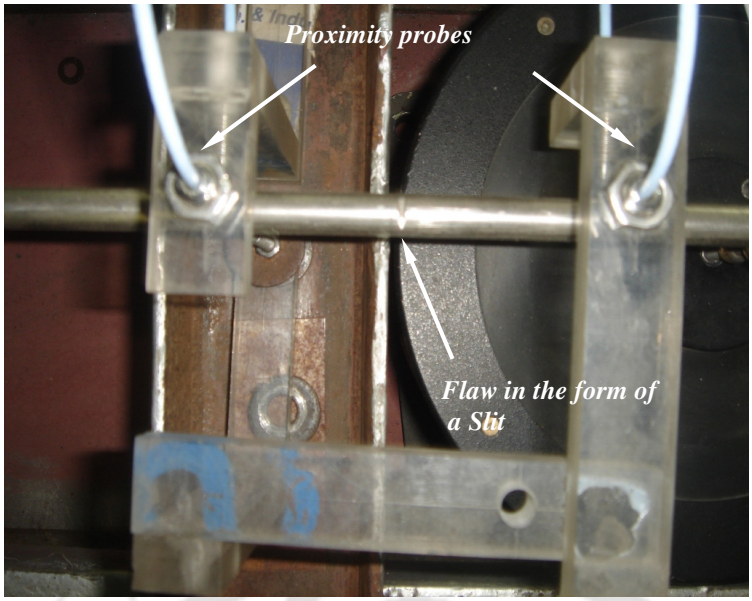

Figure 5.3 Close view of a flaw on the beam

5.3 Experimental Setup and Instrumentations

A photograph of the experimental setup with instrumentations is shown in Figure 5.4 and it comprises of the following units

1. Experimental setup
2. Excitation unit
3. The signal generator and power amplifier unit
4. The force transducer and signal conditioning amplifier unit
5. Proximity sensors and proximitor (amplifier) unit
6. Pulse analyzer (data acquisition system) and time capture module

These will be described in detail in the subsequent subsections.

Figure 5.4 An overall view of the experimental setup and instrumentations

5.3.1 Experimental setup

Figure 5.5 shows a schematic diagram of the present experimental setup with instrumentations. A circular beam was supported at its ends by rolling bearings. Rolling bearings give very high transverse stiffness; however, it allows rotation of the beam. The rotation of the beam was prevented through a stinger (pushrod), which was used to connect the exciter to the beam. An artificial open flaw (transverse slit) was made by the saw on the beam. The beam was dynamically excited with help of a modal exciter, which provided the harmonic force of a known amplitude and frequency.

A modal exciter was placed under the beam at a suitable location. For the present case, the excitation frequency was 5-105 Hz (sine-sweep) covering the first two natural frequencies of beam. The placement of the exciter was well away from the nodes of the first two modes of vibration. Moreover, the placement of the exciter was decided at the location away from the location of the flaw in the beam, which will be the most likely the case. A sensor stand was designed and fabricated to mount four proximity sensors. Depending upon the level of accuracy desired in locating the flaw (i.e., the axial distance along the beam) and the restriction due to the cross-talk between two neighboring proximity sensors; the axial distance between two proximity sensors were fixed. Provisions were made to slide the sensor stand in the axial direction of the beam at various locations over the beam length.

5.3.2 Excitation unit

Devices for exciting the structure could be divided into two types: the contacting and the non-contacting. The former involves the connection of an exciter of some form, which remains attached to the structure through out the test, whether the excitation type is continuous (sinusoidal, random etc.) or transient (pulse, chirp). The latter type includes devices, which are either out of contact throughout the vibration (such as provided by a non-contacting electromagnet) or which are only in contact for a short period, while the excitation is being applied (such as a hammer blow).

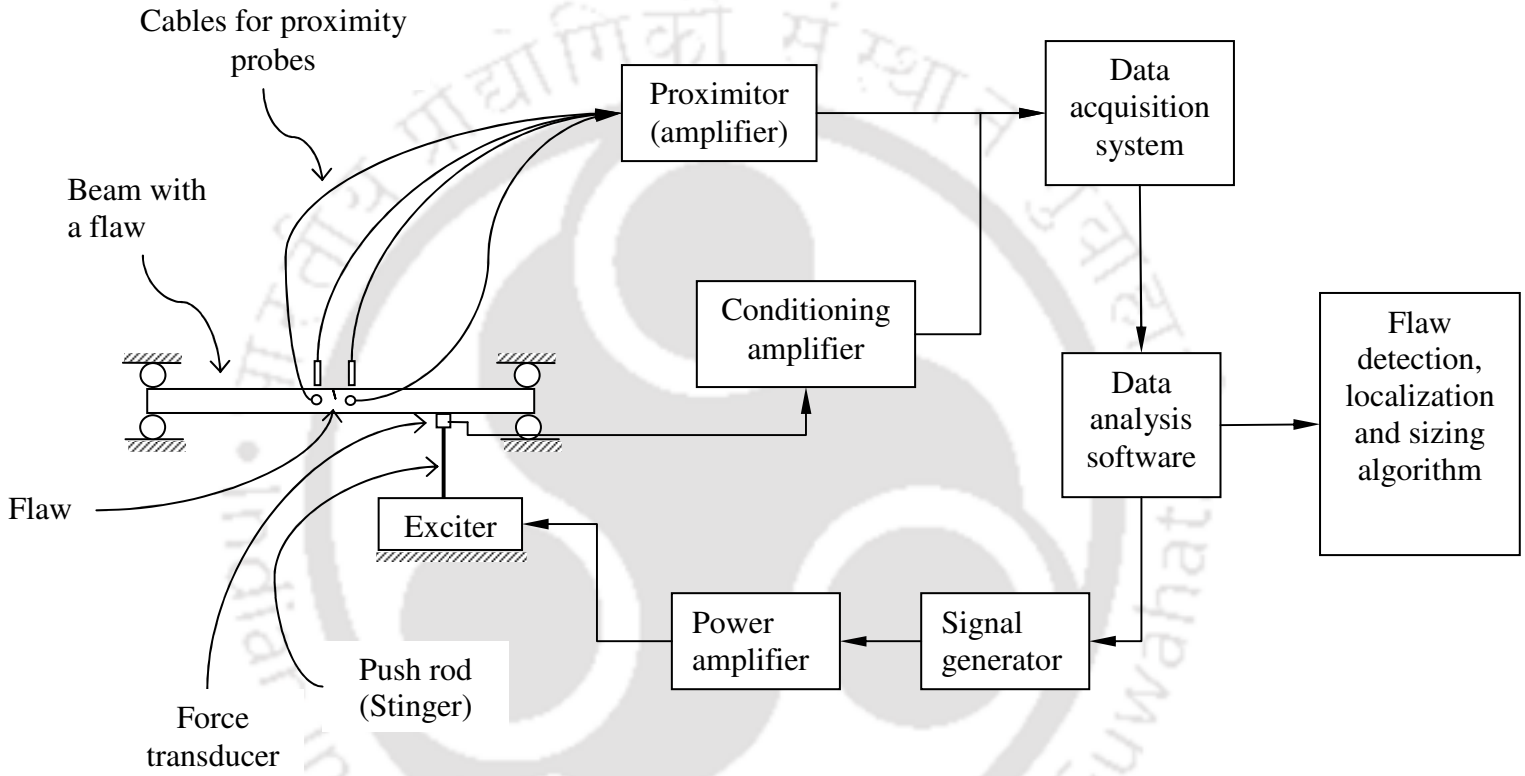

Figure 5.5 A schematic diagram of the experimental setup with instrumentations

Depending upon the types of force generated the classification of the shaker could also be made as follows:

a. Mechanical (out-of-balance rotating masses),

b. Electromagnetic (a moving coil in the magnetic field), and

c. Electrohydraulic/pneumatic.

These have been described briefly as follows:

a. Mechanical exciters

The mechanical exciter, which uses rotating out of balance masses, is capable of generating a prescribed force at a variable frequency, although there is relatively little flexibility or control in its use. The magnitude of the force is restricted by the out-of-balance, and is only variable by making adjustments to this quantity and not something that could be done while the vibration is continuing. Also, this type of excitation mechanism is relatively ineffective at low frequencies because of the speed-squared dependence. However, unless the amplitude of vibration caused by the exciter becomes large relative to the orbit of the out-of-balance mass, the magnitude and phase of the excitation force is known quite accurately and does not need further measurement, as is the case for other types of exciter. For this type of exciter the higher frequency limit is also low as compared to other type of exciters.

b. Electromagnetic exciters

The electromagnetic principle has long been used to generate vibrations in structures for the purpose of 'the modal testing'. The simplest of these applications is through the direct application of a magnetic force on the structure to be excited, without any direct physical contact. This method has its attractions but also presents severe problems of control and is not widely used, except in special cases like in the testing of rotating machines.

The most common types of exciter is the electromagnetic (or the electro-dynamic) shaker, in which the supplied input signal is converted to an alternating magnetic field by means of a coil which is attached to the drive part of the device, and to the structure. In this case, the frequency and amplitude of excitation are controlled independent of each other, giving more operational flexibility, especially useful as it is generally found that it is better to vary the level of the excitation as resonances are passed through. However, it must be noted that the electrical impedance of these devices varies with the amplitude of motion of the moving coil and so it is not possible to deduce the excitation force from a measurement of the voltage applied to the shaker. Nor, in fact, is it usually appropriate to deduce the excitation force by measuring the current passing through the shaker because this measures the force applied not to the structure itself, but to the assembly of structure and shaker drive. Although, it may appear that the difference between this force (generated within the shaker) and that applied to the structure is likely to be small, it must be noted that just near the resonance very little force is required to produce a large response and what usually happens is that without altering the settings of the power amplifier of the

signal generator, there is a marked reduction in the force level at frequencies adjacent to the structure's natural frequencies. As a result, the true force applied to the structure becomes the (small) difference between the force generated in the exciter and the inertia force required to move the drive rod and shaker table and is, in fact, much smaller than either. This is an important feature of most attached-shaker tests using the continuous sinusoidal, random or periodic excitation.

Generally, the larger the shaker greater is the force, which may be generated for exciting the structure. However, besides the obvious penalty of expense incurred by using too large an exciter, there is a limitation imposed on the working frequency range. The force generated in the exciter itself finds its way out to the structure, applies only as long as the moving parts of the shaker remain a rigid mass. Once the frequency of vibration approaches and passes the first natural frequency of the shaker coil and the drive platform, then there is a severe attenuation of the force that is available for driving the test object and although some excitation is possible above this critical frequency, it does impose a natural limit on the useful working range of the device. For larger shakers this frequency is lower.

Another consideration that concerns the shaker is how it should be supported, or mounted, in relation to the test structure. The most satisfactory arrangement is in which the shaker is fixed to ground while the test structure is supported by a soft suspension. Of the many possibilities, the structure could be grounded or ungrounded, but it may be necessary to add an additional inertia mass to the shaker in order to generate sufficient excitation forces at low frequencies. The particular problem, which arises here, is that the reaction force causes a movement of the shaker body, which at

low frequencies, could be of large displacement. This in turn, causes a reduction in the force generation by the shaker so that its effectiveness at driving the test structure is diminished.

c. Electrohydraulic/pneumatic exciter

In this excitation device, the power amplification to generate a substantial force is achieved through the use of hydraulics/pneumatics; however, these are more costly and complex than their electromagnetic counterparts.

The following are the features of the vibration exciter (B&K, Type 4808) that was used in the present experiment (see Figure 5.6). It has force rating of 112 N sine-peak (or 187 N with the cooling). The working frequency range is 5 Hz to 10 kHz and the first axial resonance is 10 kHz. The maximum bare table acceleration is 700m/s^2 (71g). It has low cross motion and low distortion, robust rectilinear guidance system and highly damped axial, transverse and flexural resonances. The table displacement is continuous 12.7 mm (0.5 in) peak-to-peak with over travel stops.

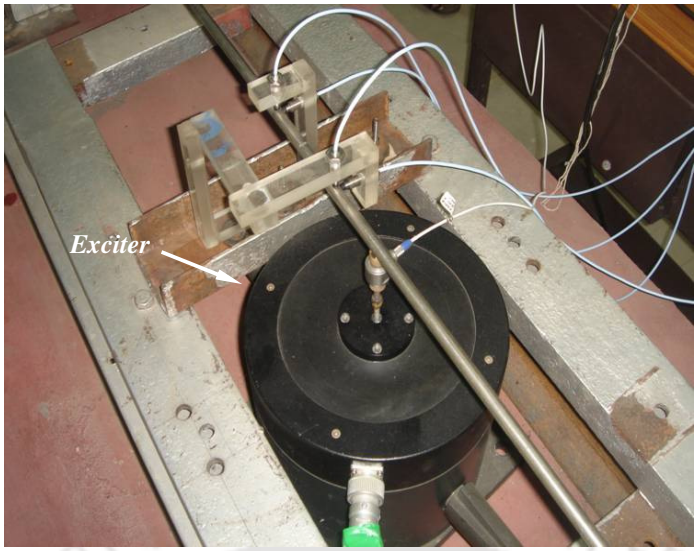

Figure 5.6 Close view of a vibration exciter assembly

5.3.2.1 Attachment to the structure

For excitation devices, it is necessary to connect the driving platform of the shaker to the structure, usually incorporating a force transducer. In the present experiment, a stinger was used as a connector (see Figure 5.7). Precautions to be taken in order to avoid the introduction of unwanted excitations or the inadvertent modification of the structure are discussed in the subsequent paragraph.

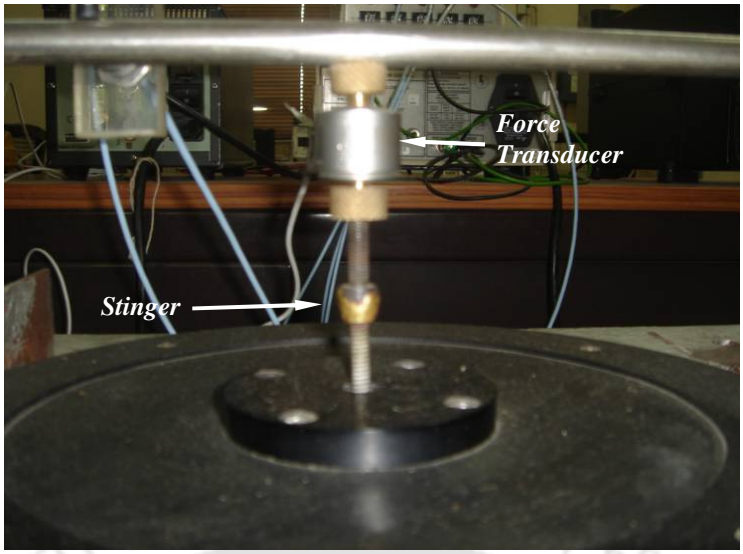

Figure 5.7 Close view of a stinger and a force transducer

A single force must be the only excitation of the structure and we must satisfy this condition in any test. Although, it may seem that the essentially a unidirectional device - there exists a problem on most practical structures whose motion is generally complex and multidirectional. The problem is that when pushed in one direction- say, along the *x* axis - the structure responds not only in that same direction but also in others, such as along the *y* and *z* axes, and also in the rotation directions. Such motion is perfectly in order and expected but it is possible that it can give rise to a secondary form of excitation, if the shaker incorrectly attached to the structure. It is usual for the moving part of the shaker to be very mobile along the axis of its drive but for it to be quite the opposite (i.e., very stiff) in the other directions. Thus, if the structure wishes to respond in, say, a lateral direction as well as in the line of action of the exciter, then the stiffness of the exciter will cause resisting forces or moments to be generated which are, in effect, exerted on the structure in the form of a secondary excitation. The response transducers pickup the total response, which is that caused not only by the intended driving force (which is known) but also by the secondary and unknown

forces. The solution is to attach the shaker to the structure through a drive rod (stinger) or similar connector which has the characteristic of being stiff in one direction (that of the intended excitation), while at the same time being relatively flexible in the other five directions.

5.3.3 Signal generator and power amplifier

The necessary excitation to the beam with flaw was given by a modal exciter, which was operated by a signal generator module of the B&K Pulse software through a power amplifier. Descriptions of these equipments are provided in the subsequent subsections. Figure 5.8 shows the signal generator module with associated Pulse software and the power amplifier.

5.3.3.1 Signal generator module

The generator module (B&K, Type 3107) provides various kinds of signals required for system measurements. In the present experiment a sine-sweep signal of 5-105 Hz was used to excite the beam. The phase between sine waves from different generator modules could be set. In addition to this, it has capability of generating random or burst random signals from different generator modules and is uncorrelated. Some of features of the signal generator module are as follows:

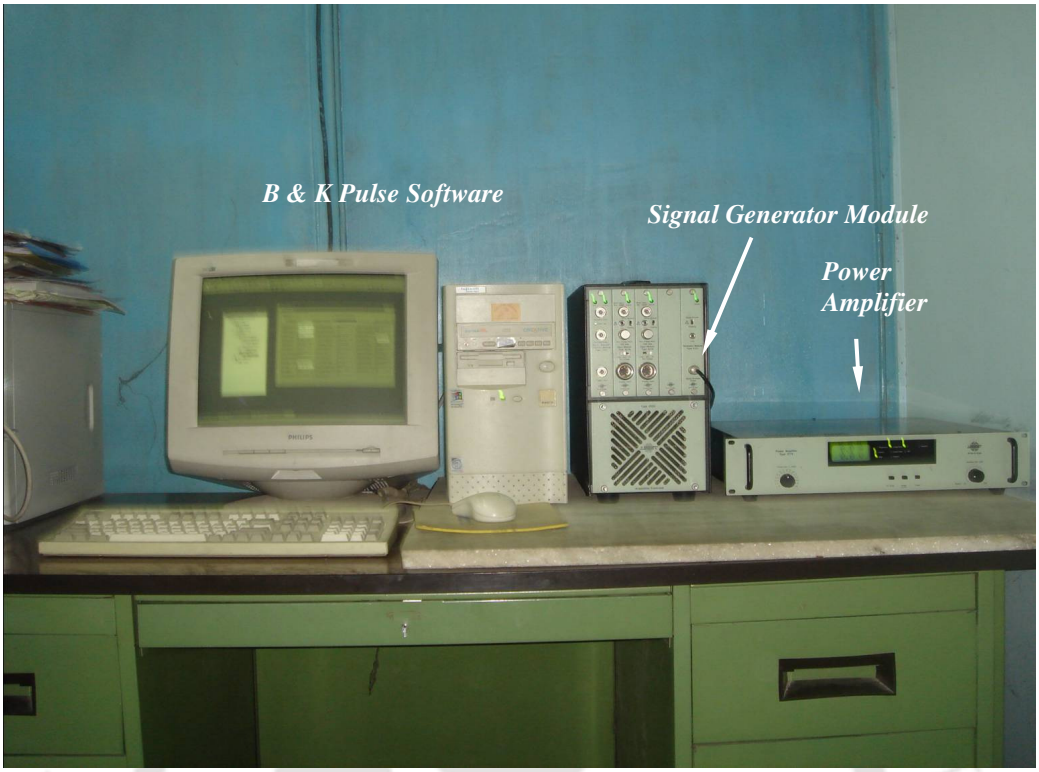

Figure 5.8 A signal generator module with a power amplifier

(i) Generator: The generator is designed around a digital signal processor and a 16-bit D/A converter. The frequency range is 0 to 102.4 kHz, with a frequency accuracy and stability of ± 0.01%. Output levels are adjustable from 1 mV to 5V, and can be referred to ground or floating. It is possible to add a DC offset, but any unwanted DC offset is automatically removed.

(ii) Waveforms: The single and dual superimposed sine waves could be generated. Both the sine and dual sine waveforms could be swept. Dual sine waves could be combined in fixed/swept, swept/swept or fixed/ fixed modes. There are other options for the types of waveforms, like the multi-sine, random, pseudo-random, periodic-random, pulse, and user-defined. The waveform of the single sine wave combined with swept mode was used in the present experiment.

5.3.3.2 Power amplifier

The power amplifier (B&K, Type 2719) was used in the present experimentation to drive the vibration exciter. It has 180VA power output, adjustable RMS output-current limit and low or high output impedance. It can be operated over wide frequency range with low distortion. The front panel of the power amplifier has indicators (LEDs) showing the clipped output signal, temperature and current overloads, output signal phase (0° or 180°), operating mode (current or voltage), current state, and interlock input disabled. Multifunction display (backlit LCD) shows the output current and voltage. The power amplifier is designed to drive small vibration exciters, particularly the 112 N vibration exciter (B&K, Type 4808).

5.3.4 Force transducer and signal conditioning amplifier

The amplitude of the excitation to the beam is to be amplified and measured. This is done by force transducers that sense the amplitude of the exciting force and the signal conditioning amplifier, which amplify the force signal sensed by the force transducer to the measurable level. The following are the description of force measuring equipments.

5.3.4.1 Force transducers

The piezoelectric type of transducers is the most popular and widely used means of measuring the parameters of interest in modal tests. The force transducer is the simplest type of the piezoelectric transducer. The transmitted force, or a known fraction of it, is applied directly across the crystal, which thus generates a

corresponding charge, proportional to the force. It is usual for sensitive crystals to be used in pairs, arranged so that negative sides of both are attached to the case, and positive sides are in mutual contact at their interface. This arrangement obviates the need to insulate one end of the case from the other electrically. One important feature in the design of force gauge is the relative stiffness (in the axial direction) of crystals and of the case. The fraction of force, which is transmitted through crystals, depends directly upon this ratio.

The force indicated by the charge output of crystals will always be slightly different from the force applied by the shaker, and also from that transmitted to the structure. This is because a fraction of the force detected by crystals will be used to move the small amount of material between crystals and the structure. The following are features of the force transducer (B&K, Model 2311-1), which was used in the present experiment (see Figure 5.7). It was designed for the modal exciter, and to measure the compression and tension excitations. It had low impedance output and its force sensitivity was 0.227 mV/N and the maximum frequency range was up to 75 kHz.

5.3.4.2 Signal conditioning amplifier

One of the advantages of the piezoelectric transducer is that it is an active device, and does not require a power supply in order to function. However, this means that it cannot measure truly static quantities and so there is a low frequency limit below which measurements are not practical. This limit is usually determined not simply by the properties of the transducer itself, but also by those of amplifiers which

are necessary to boost the very small electrical charge that is generated by crystals into a signal enough to be measured by the analyzer. Two types of amplifier are available for this role- voltage amplifiers and charge amplifiers- and the essential characteristic for either type is that it must have very high input impedance.

The measuring amplifier (B&K, Type 2525) was used for the present experimentation. It had charge and DeltaTron inputs. The signal integration was there for getting the displacement and the velocity responses. It had selectable low, high-pass filters and user-defined filters. It could be connected for external filters. It had dynamic range of 100 dB with RMS, +peak, –peak, peak-to-peak meter function with read-out in metric or imperial units. Its measurement mode could be the acceleration, velocity, displacement or force.

5.3.5 Proximity sensors and proximitor unit

Vibrations (displacements) of the excited beam were sensed by proximity sensors, and sensed signals were amplified to the required level by the proximitor. Descriptions of these equipments are given as follows.

Non-contact displacement transducers (see Figure 5.9) operate on eddy current principles i.e., it provides a voltage signal proportional to the gap between the probe tip and the shaft. It comprises of a probe, a length of extension cable and an oscillator demodulator. The proximity probe sensitivity was 7874 V/m. Displacement signals sensed by proximity sensors were amplified in the proximitor and the conditioning amplifier (see Figure 5.10).

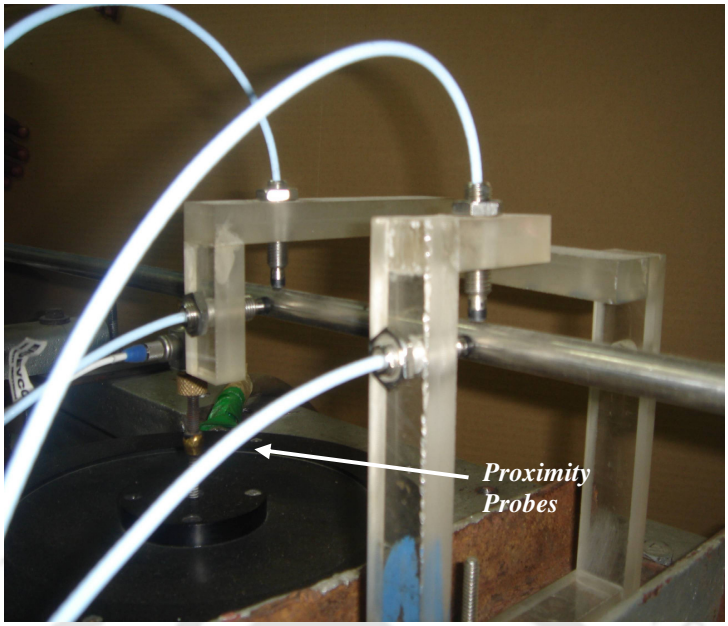

Figure 5.9 Proximity sensors and its mountings

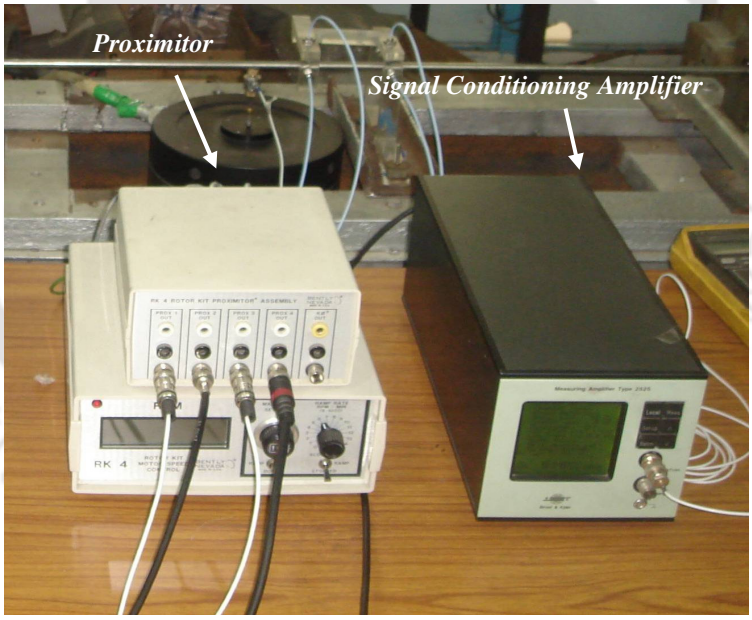

Figure 5.10 A proximitor with a signal conditioning amplifier

The probe stand was a specially fabricated plastic stand, which had threaded holes. Proximity sensors were screwed in these holes. The stand could be fixed at any required axial position of the beam for transverse displacement measurements.

5.3.6 Pulse analyzer (Data acquisition system) and time capture module

Pulse analyzer® (B&K, 3560C) as shown in Figure 5.11 is a PC-based sound and vibration analysis system.

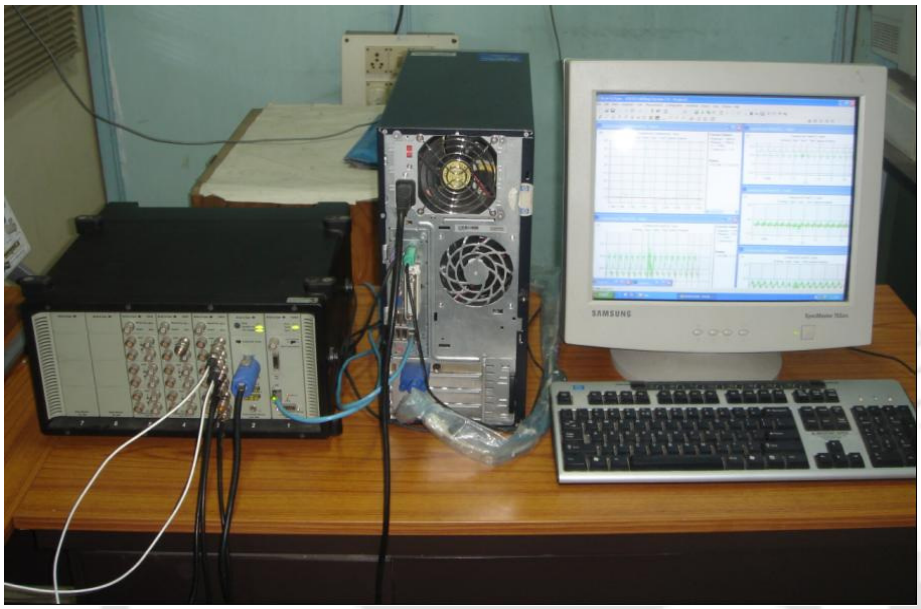

Figure 5.11 The Pulse analyzer hardware and software

A Pulse system consists of a PC with LAN interface, Pulse software, Microsoft® Windows® operating system, and data acquisition front-end hardware. The system has both time capture and FFT analyzers for recording the real-time data. The input/output conditioning modules perform signal conditioning and digitize transducer signals. The Pulse software provides analysis capabilities like real-time measurements, real-time DSP resources to perform FFT analysis on 16 channels up to 25.6 kHz bandwidth (0% overlap, 6400 lines) and 1/3-octave analysis on 6 channels up to 25.6 kHz bandwidth. This performance requires a Pentium III 1GHz computer or faster.

5.3.6.1 Time capture module

The basic objective of the data acquisition and processing mechanism is to measure signals developed by the sensing mechanism and to ascertain the magnitude and phase of excitation forces and responses. There are devices for this purpose, called analyzers, which incorporate many functions and even include the signal generation component. Among many analyzers, time capture analyzers are used to capture signals in 'as is' format in time domain. This feature enables easier extraction of the phase information of responses with respect to force signals.

The time capture analyzer (B&K, Type 7705) was used in the present experimentation in order to capture, retrieval and export of time-data sequences. Capture of long time records for Vold-Kalman order analysis (B&K, Type 7703) also could be possible with the analyzer. Pre-processing of the input data; and the post-processing and the time inspection of long time records could be done. Any selectable part of a recorded signal can be extracted and all these analysis could be done as post-processing. Its frequency range varies from 156.25 μHz up to 102.4 kHz for the normal analysis and the post-processing.

Having described the detailed description of the experimental setup, and all the necessary signal measuring and processing instruments; now in the subsequent section the procedures of conducting experiment are presented.

5.4 Test Procedure

There are many types of excitation testing, which is available based on the use of different excitation signals. They are the stepped-sine testing, slow-sine sweep testing/sine sweep testing, and broadband testing; which uses the random and periodic excitations. In the present experiment, the slow-sine sweep testing was adopted and it is described in subsequent subsections.

5.4.1 Slow - Sine Sweep Testing

This is a traditional method of the mobility (or the frequency response) measurement, and involves the use of a sweep oscillator to provide a sinusoidal command signal; the frequency of which is varied slowly but continuously through the range of interest. It is necessary to check that progress through the frequency range is sufficiently slow to ensure that the steady-state response conditions are attained before measurements are made. Table 5.1 gives required information about beam parameters, number of beam elements, and flaw parameters (i.e., the location and the size). Main steps of the experimental procedure are detailed in stages as follows.

Stage 1: Presetting of the experimental setup

i. The intact beam was assumed to have a number of finite beam elements and each node of elements was marked as reference for measurement locations.

ii. The beam at its both ends was supported on two preloaded rolling bearings (see Figure 5.2), which gives very high transverse stiffening effect (Goodwin, 1989).

iii. The modal exciter was placed under the beam around one third of the beam span (Figure 5.6).

iv. The signal input of the exciter was connected to the signal output channel of the power amplifier, and the power amplifier was connected to the signal generator module of the Pulse system as shown in Figure 5.8.

v. One end of the stinger was firmly fixed to the exciter, and the other end was connected to the beam through a force transducer as shown Figure 5.7.

vi. The force transducer was attached to the beam via a screw connector, which was glued to the beam and the signal output of the transducer was connected to the signal-conditioning amplifier.

vii. The proximity sensor stand was fixed at a measurement location. There were two measurement planes at two axial positions of the beam, and measurements were taken in the vertical and horizontal directions; hence total four proximity sensors were mounted on the stand (see Figure 5.9). The proximity sensors were connected to the proximitor.

viii. The force signal output (one) from the signal-conditioning amplifier, and displacement signal outputs (four) from the proximitor were connected to signal input channels (total five) of the data acquisition (DAQ) system of the Pulse system.

ix. Proximity sensors observing the beam were adjusted to have 30 mil (0.000762 m) gap using a DC voltmeter, which should measure -5.75±0.5V approximately.

x. The time capture module of the Pulse system was started to capture signals in order to ensure working of all input channels of the DAQ. Now the experimental setup was ready to measure the force and displacement signals.

Stage 2 Measurement of signals

i. The time capture module of the Pulse system was started to capture the signals.

ii. The standard impact test was performed for estimating the system damping ratio by using the logarithmic decrement method. The damping ratio of the system was assumed to be one percent for numerical simulation; however, it was estimated experimentally for experimental investigation.

iii. The signal generator was started to generate the sinusoidal signal in the preset sweep range of frequency (i.e., 5-105 Hz).

iv. The generated signal were amplified and controlled by the power amplifier, and was sent to the exciter.

v. The exciter was started to give the excitation. The excitation in time domain for the whole sine sweep period (i.e., 5-105 Hz) was sensed by the force transducer and conditioned by signal conditioning amplifier. The force signal was sent to the DAQ for the digitization.

vi. Transverse plane linear displacements (four) were sensed by proximity sensors, amplified in the proximitor, and sent to the DAQ for digitization.

vii. The digitized measurement data, which was recorded for the whole frequency sweep (100 seconds, i.e., 5-105 Hz @ 1 Hz per second), were stored in a personal computer for the post processing.

viii. Similar measurements were taken by shifting the sensor stand at various axial locations of the shaft. All such measurements were stored in personal computer for further processing. The distance between two probes at the element nodes was 35 mm (i.e., element length) and probes were shifted and positioned at alternative element locations.

Stage 3 Signal processing

i. Captured measurement data were transported to the MATLAB environment for processing.

ii. The stored force and displacement data were resampled for small time duration (i.e., equivalent to one Hz of frequency), during which the change in the frequency was assumed to be negligible. Such samples were chosen in the whole frequency range of data, and the amplitude and phase information were extracted (i.e., the frequency response function). The phase of displacement was obtained with respect to the corresponding force data for all the displacement data at various frequencies.

iii. As the number of sample (i.e., that many frequency points in the frequency response function) could affect the accuracy of extraction of flaw information using the proposed identification algorithm, an optimum number of samples were chosen by the trial and error to compromise between the computational time and the loss of information.

iv. The extracted information (from all the captured data) was used to obtain the ratio of the force and the response with respect to frequencies.

v. In these data resonance conditions were observed from the amplitude peaks and associated sudden change in the phase of the order of 180^0.

vi. These frequency response functions and first resonance frequency are required for the proposed flaw detection, localization and sizing algorithm.

The above procedure was repeated for two beams with flaw as well as for the intact beam. The measured and processed data will be used for the estimation of damping coefficients, updating of the FE model and the flaw parameter estimation.

5.5 Results and Discussions

This section includes the estimation of damping ratio of the test beam system, and updating of FE model. The detection, localization and sizing of the flaw by the developed algorithm based on experimental forced responses have been discussed.

5.5.1 Estimation of damping of the beam

Experimentally the damping ratio is estimated by using the standard impact test method in order to provide the damping ratio in the flaw identification algorithm. Figure 5.12 shows the amplitude of acceleration versus time for the excitation with help of an impact hammer. The damping ratio ζ can be expressed as (Meirovitch, 1986)

$$\zeta = \frac{\delta}{\sqrt{(2\pi)^2 + \delta^2}} \tag{5.1}$$

where δ is the logarithmic decrement and can be written as

$$\delta = \frac{1}{p} \ln \frac{x_1}{x_{p+1}} \tag{5.2}$$

where p is the number of complete cycles, x_1 and x_{p+1} are vibration amplitudes of the first and p^{th} cycle, respectively.

The damping ratio was estimated from equations (5.1) and (5.2) for the four numbers of samples at different time intervals in Figure 5.12. They were $\zeta_1 = 0.0116$, $\zeta_2 = 0.0181$, $\zeta_3 = 0.0143$, and $\zeta_4 = 0.0165$. The average damping ratio $\zeta = 0.0151$ was used for estimating the Rayleigh's damping factors a_0 and a_1, and expressions for these are given in Appendix B. The obtained damping factors were used to develop the system Rayleigh's damping given by equation (3.9).

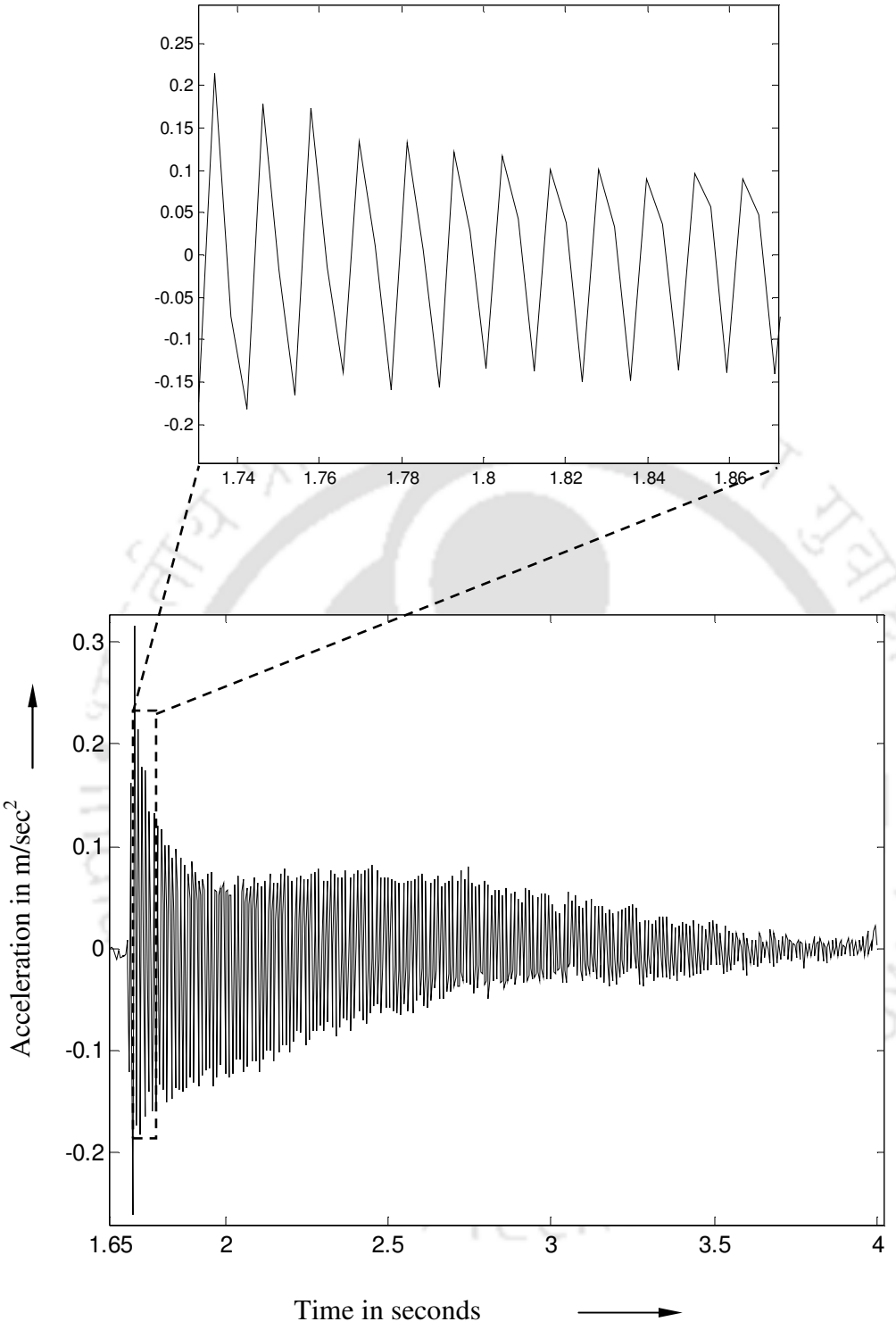

Figure 5.12 Free vibration of the test beam for the estimation of damping ratio

5.5.2 Updated finite element model

The approach of numerical predictions to the behaviour of a physical system is limited by the assumptions used in the development of the mathematical model. The finite element model has been updated, which is about correcting invalid (unknown) assumptions by processing vibration test results. A finite element model, which will be updated, requires in its preparation the consideration of factors not normally taken into account in the regular model construction. For example, the main span of a beam, away from the boundaries, might be considered to be modeled with a high level of confidence. Joints and constrains could be considered to be less accurately modeled, and therefore in greater need of updating. The extent to which a numerical model could be improved by updating depends upon the richness of information of the test structure contained in measurements. Rigidly clamped boundary or simply supported conditions are usually very difficult to obtain in a physical test. Extreme care is necessary to either eliminate systematic errors, or to obtain an assessment of them, which can be used in subsequent processing.

In the present work, the theoretical model assumes the simply supported boundary condition; however, it is very difficult to mimic the same boundary condition experimentally. In practice the supports would provide some flexibility. For the rolling bearing support theoretical calculations are available to obtain the stiffness, approximately (Goodwin, 1989). The error involved in modeling the bearing stiffness was updated (i.e., by the trial and error method) in the finite element model by matching natural frequencies (up to second modes) from the theoretical model with experimental frequencies. The stiffness of the rolling bearing was modeled by two

transverse direction direct stiffness coefficients only, and obtained by the method given in Goodwin (1989). For brevity, both rolling bearings were assumed to be identical for a particular case. For two beams (e.g., Beams 1 and 2 in Table 5.1), which were considered for the present case, the updated direct stiffness coefficients, respectively, were $k_{xx} = k_{yy} = 75315$ N/m and $k_{xx} = k_{yy} = 447215$ N/m . First the intact beam was mounted and measurements were taken, and then without dismounting the bearings a flaw was created in a form of a slit by a saw on the beam. Therefore, it was assumed that during this process boundary conditions remained the same. Table 5.2 compares the first resonance frequency obtained experimentally with the finite element analysis by considering simply supported boundary conditions, and the updated finite element model by considering the flexibility of supports.

Table 5.2 Comparison of the first resonance frequency

Beam No	Intact beam resonance frequency (RF) in Hz			Beam with flaw RF in Hz (% of reduction with intact beam)
	Experimental	FEM with simply supports	Updated FE model	Experimental
1	21.5	22.1	21.5	21.25 (1.16)
2	22.0	22.1	22.0	21.625 (1.71)

The first resonance frequency has been chosen to match perfectly, since the flaw identification algorithm uses the first natural frequency for the flaw localization, however, the updated second natural frequency also comes closer to the experimental ones, as it can be observed from Figures 5.13 and 5.14.

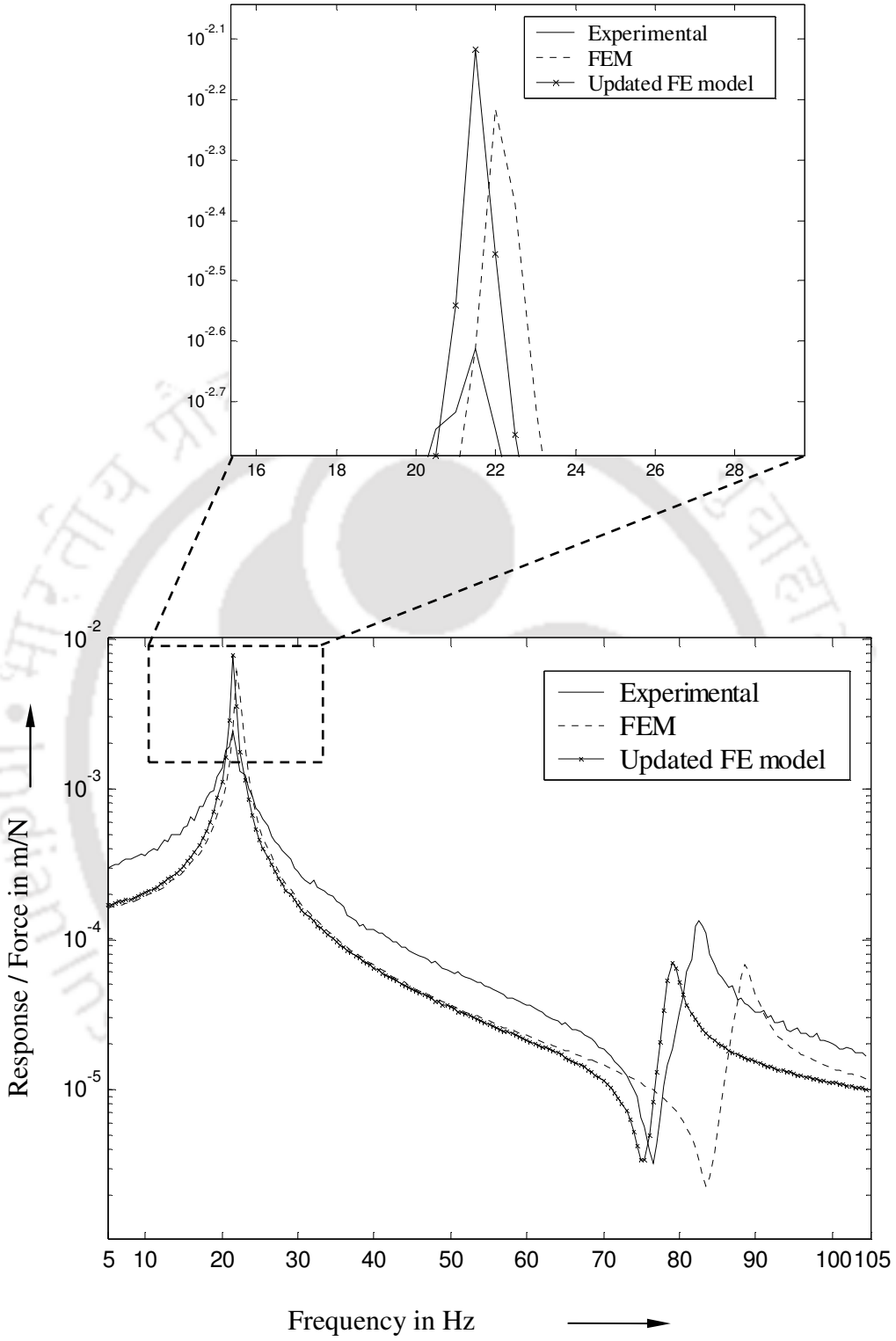

Figure 5.13 Comparison of FRFs for beam 1 with flaw

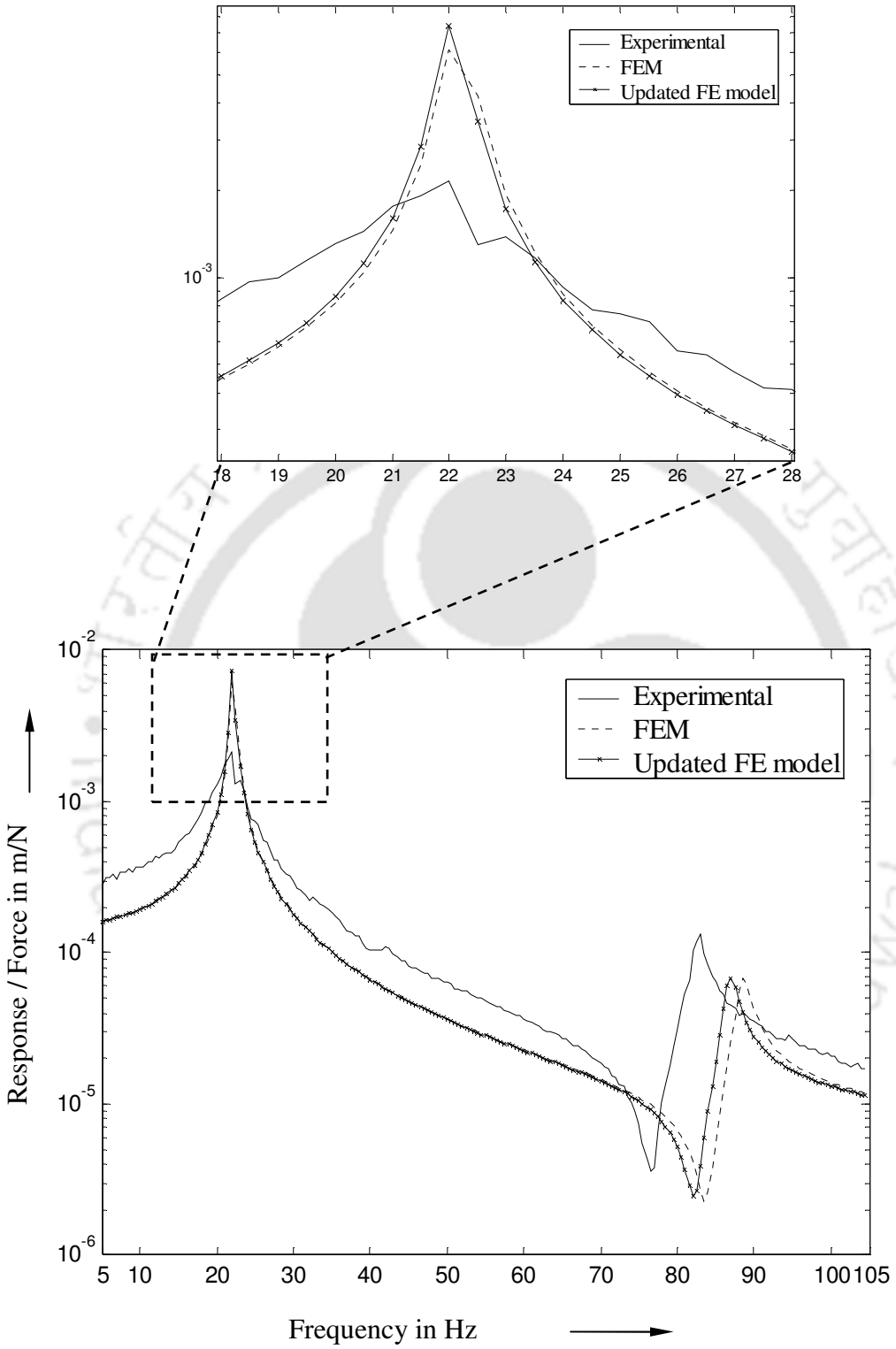

Figure 5.14 Comparison of FRFs for beam 2 with flaw

Figures 5.13 and 5.14 also show the comparison of FRF (i.e., the receptance FRF; Ewins, 2000) obtained by experiments, FEM and updated FE model for beams 1 and 2 with flaw, respectively. The difference in direct stiffness coefficients for beams 1 and 2 is due the fact during dismounting/remounting of bearings; it is difficult to maintain the same level of tightness of the bearing inside the bearing block. Literature also indicate that the stiffness of the rolling bearing very much depends upon the level of preloading (Tiwari and Vyas, 1995). The updated FE model was used for the flaw detection, localization and sizing algorithm, which is discussed in subsequent sections.

5.5.3 Detection, localization and sizing of the flaw

The proposed algorithm for the flaw detection, localization and sizing was tested using experimentally obtained responses of a beam with flaw. Two beams were considered, which had a flaw at different locations and of dissimilar sizes, and their properties are given in Table 5.1. For beam 1, the flaw was made at mid span to study the effects of the flaw in the first mode of vibrations. Since effects is expected to be more in the first mode, and less (due to presence of a node) in the second mode of vibrations. Moreover, in order to study effects of the flaw in the second mode of vibrations, the flaw was made at around 1/3 of the span for beam 2.

5.5.3.1 Beam 1 with flaw

For beam 1, the first resonance frequency (experimental) of the intact beam was found to be 21.50 Hz (see Figure 5.13). For beam 1 with flaw, which had a flaw of the depth ratio $\bar{a}$ = 0.41 and the flaw location ratio $\bar{x}$ = 0.5 (i.e., 14th element), the

first resonance frequency was found to reduce to 21.25 Hz. The change in resonance frequencies confirmed the presence of flaw and was used in the flaw detection (see Table 5.2).

Figure 5.15 shows the comparison of the measured and estimated responses from the updated FE model (with the help of estimated flaw parameters) for beam 1 with flaw in the vertical plane. The comparison of the first two resonance peaks is in very good agreement. The phase variation shows good comparisons of phase change of around 180^0 at resonances. However, it also shows the phase changes at anti-resonances. Figure 5.16 gives the similar variation, in the horizontal plane. The experimental fundamental resonance frequency and forced responses were fed to the identification algorithm in order to identify flaw parameters as discussed in Subsection 4.3.2.

Identification of *flaw parameters*:

The identification of flaw parameters means the estimation of flaw location and its size. In the identification algorithm, both (i.e., the flaw location and its size) have to be estimated iteratively for their convergence by using the experimental measured force and response information, and updated FE model.

Figure 2.8 shows the procedure of finding the flaw location. For the flaw localization, the flaw depth ratio is assumed initially between 0.9 and 1.0 (based on the numerical simulation exercise, it is advisable to use a higher flaw depth ratio as an initial guess).

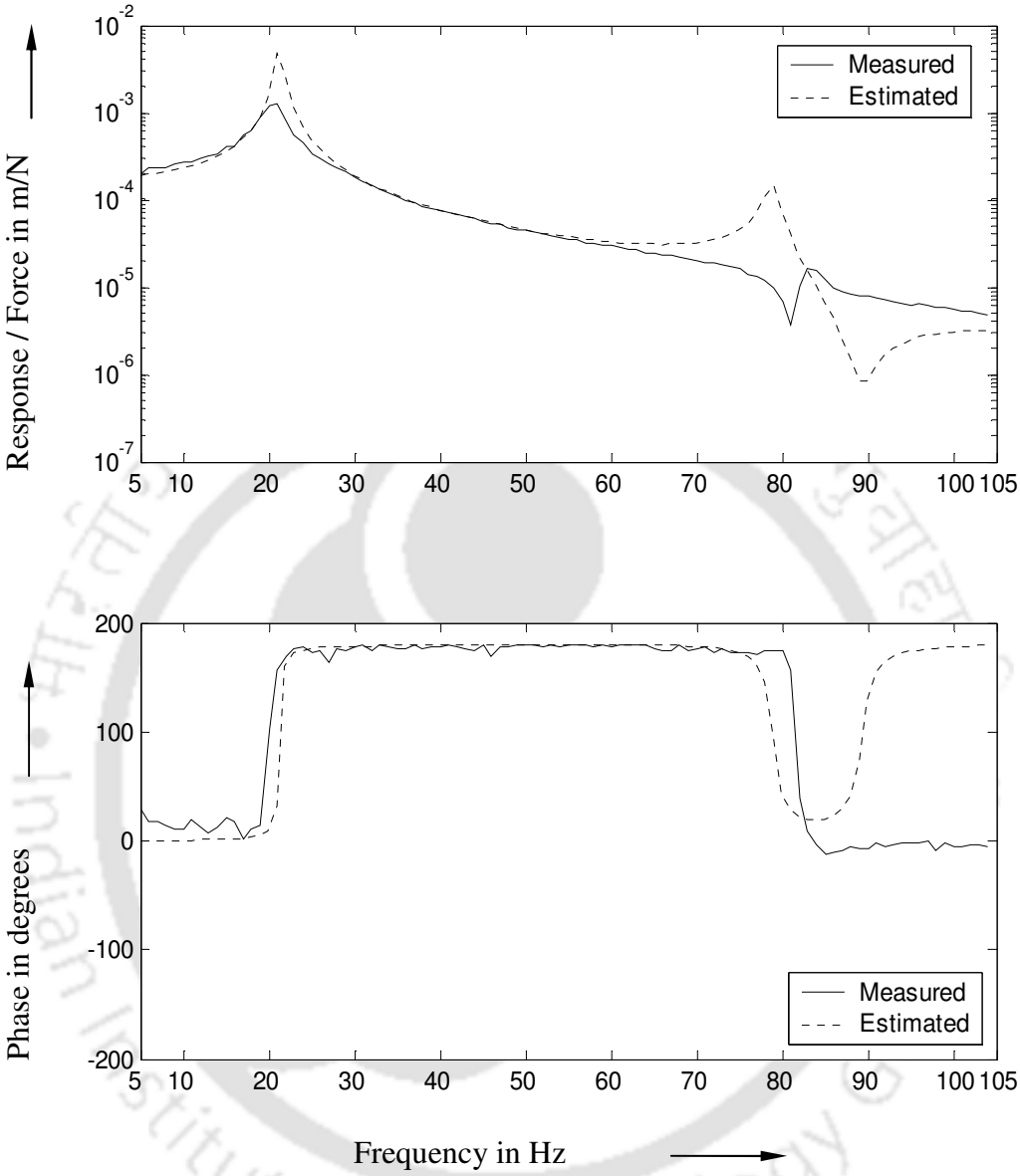

Figure 5.15 Frequency response function in vertical plane for beam 1 with flaw

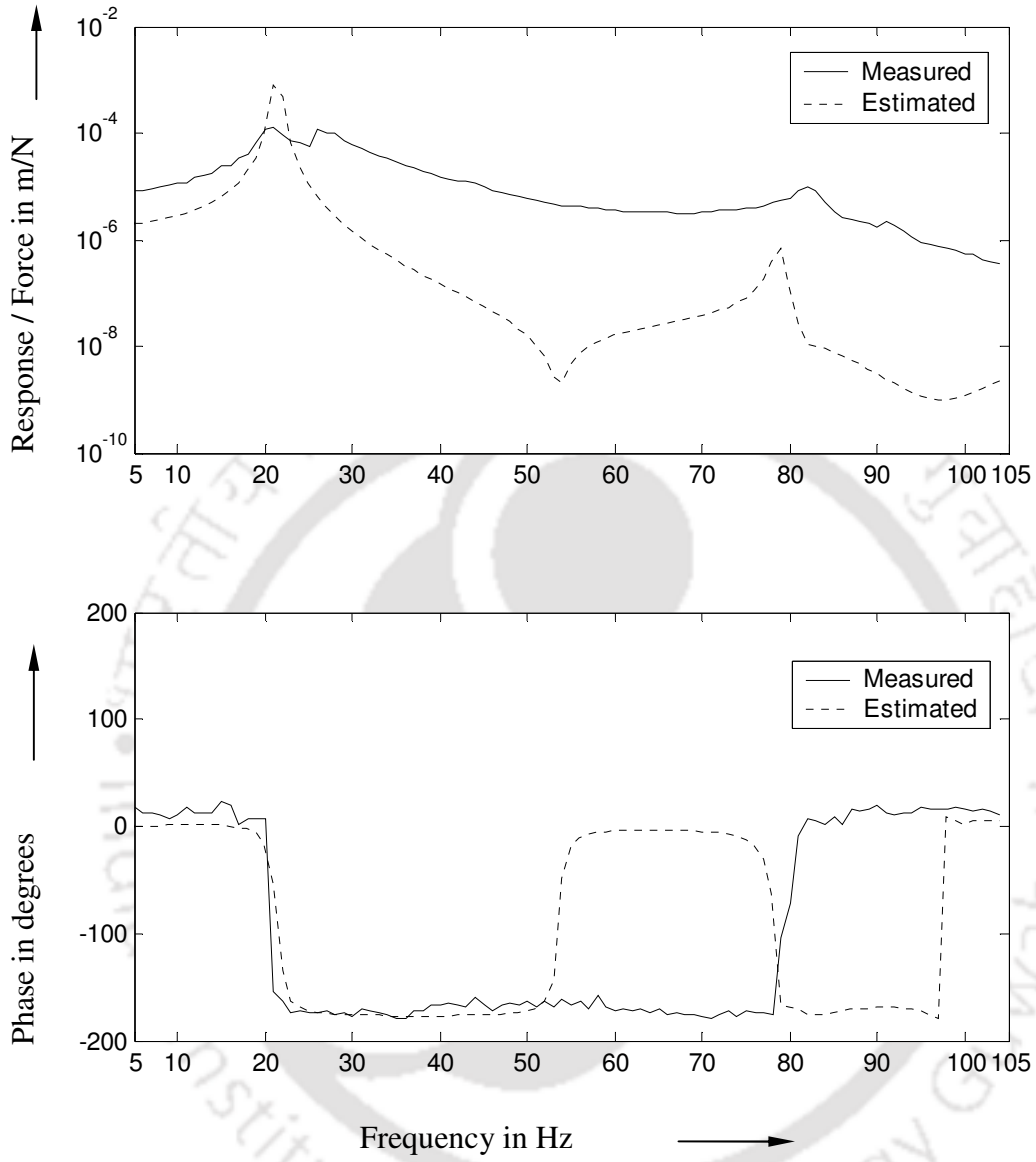

Figure 5.16 Frequency response function in horizontal plane for beam 1 with flaw

For the initially assumed flaw depth ratio of $\bar{a}_{ig}$ = 0.9, when the natural frequency is available experimentally, it gives the initial flaw location to be 0.27 (8th element). With this flaw location, flaw location flexibility coefficients of the flaw are obtained from estimation equation (4.24), and subsequently it gives equivalent flaw depth from equation (2.30). The equivalent flaw depth is used as a new flaw depth

and variations of resonance frequencies (see Figure 2.8) are obtained by using equation (2.14) to get a new possible flaw location. The convergence criteria adopted here is that the difference between flaw depth ratios of the two consecutive iterations should be less than 0.01.

It is possible to get two or more intersection points, which corresponds to that many number of possible flaw locations. It was found that with each of these possible flaw locations as subsequent guess value, finally all converges to a single value of the flaw location. It can be seen from Table 5.3 that at 7^{th} iteration corresponding to flaw depth ratio of 0.69, there is no possible intersection of the experimental natural frequency line with the natural frequency variation by the FEM (as shown in Figure 2.8). Hence, the final converged value of the flaw location has been chosen as 0.7 (the guess in the 6^{th} step in Table 5.3). As illustrated in Table 5.3, with the present algorithm, the flaw location converges at $\bar{x} = 0.48$ (13^{th} element) along with the flaw size $\bar{a} = 0.70$. It should be noted that the actual location of the flaw was at $\bar{x} = 0.50$ (14^{th} element) along with the flaw size $\bar{a} = 0.41$. However it should be pointed out that the size of the flaw is equivalent that means while modeling a flaw, it is considered as a negligible thickness and a perfectly straight flaw front. Moreover, in actual case it has a finite thickness and an irregular flaw front.

Table 5.4 summarized the flaw parameter estimated for the above case in the first row, which is corresponding to the force and the response data for five number of frequency points below the first natural frequencies. Apart from the flaw location and its size, it also shows the comparison of flexibility coefficients. It can be seen that the prediction for the flaw location is very good. The flexibility coefficients are compared

with the theoretical ones corresponding to the obtained flaw size and found to be very good in agreement. The estimate of the flaw size is over estimated as compared to the measurement made physically. Table 5.4 also shows several case studies by using experimental measurements corresponding to different number of excitation frequencies (5 or 10) and in different regions of the resonance (i.e., before and after the first resonance) and the converged estimated parameters, viz. the flaw location, flaw flexibility coefficients, and equivalent flaw depth ratios. It is observed that there is no appreciable change in the estimation of flaw locations, flaw flexibility coefficients and flaw sizes. Overall the number of iterations for the final convergence is very less (maximum is less than 10, however, 3 to 4 is very common). The regularization parameter $\eta = 900$ is used for the present case.

Table 5.3 Iteration details for beam 1 with flaw

Iteration no	Guess for the flaw depth ratio	Flaw location ratio (corresponding element no.)	Equivalent flaw depth
1	0.90	0.27 (8)	0.85
2	0.85	0.33 (9)	0.77
3	0.77	0.37 (10)	0.73
4	0.73	0.41 (11)	0.72
5	0.72	0.44 (12)	0.70
6	0.70	0.48 (13)	0.69
7	0.69	no possible intersection *	0.70

* There is no possible intersection of the experimental natural frequency line with the natural frequency variation by the FEM (as shown in Figure 2.8)

Table 5.4 Actual and estimated flaw parameters for beam 1 with flaw

Beam no.	Actual flaw parameters (approx.)		No. of ω (case)*	Estimated flaw and parameters											
				Flaw flexibility coefficients (C^{id} and C^{th}) †										$\bar{x}$ (n)	$\bar{a}_e$
	$\bar{x}$ (n)	$\bar{a}$		$C_{22}\,(\mathrm{mN}^{-1})$		$C_{33}\,(\mathrm{mN}^{-1})$		$C_{44}\,(\mathrm{mN})^{-1}$		$C_{45}\,(\mathrm{mN})^{-1}$ ($=C_{54}$)		$C_{55}\,(\mathrm{mN})^{-1}$			
				C_{22}^{id}	C_{22}^{th}	C_{33}^{id}	C_{33}^{th}	C_{44}^{id}	C_{44}^{th}	C_{45}^{id}	C_{45}^{th}	C_{55}^{id}	C_{55}^{th}		
1	0.5 (14)	0.41	5, (b)	0.598	0.602	0.894	0.901	1.443	1.467	3.900	3.959	8.730	8.813	0.48 (13)	0.702
			10, (b)	0.613	0.609	0.917	0.910	1.498	1.493	4.002	4.016	8.929	8.910	0.48 (13)	0.705
			5, (a)	0.641	0.609	0.958	0.910	1.554	1.493	4.431	4.016	8.560	8.910	0.48 (13)	0.705
			10, (a)	0.665	0.611	0.994	0.914	1.704	1.502	4.333	4.034	8.625	8.943	0.48 (13)	0.706

where ω is excitation frequencies, n is element number, and $\bar{a}_e$ is the equivalent flaw depth ratio

* Cases (b) and (a) indicates before and after the first resonance condition, respectively;

† Superscripts '*id*' and '*th*' indicate the estimated and theoretical, respectively (theoretically, flaw flexibility coefficients were obtained from linear fracture mechanics approach (Papadopoulos and Dimarogonas, 1987)).

5.5.3.2 Beam 2 with flaw

This example is provided to justify the consistency of the present algorithm. The required beam parameters and other data are provided in Table 5.1. From experiments, the first resonance frequency of the intact beam is found to be 22.00 Hz (see Figure 5.14). For the beam with flaw the first resonance frequency is found to be 21.625 Hz for the physically measured flaw depth ratio ($\bar{a}$) and the flaw location ($\bar{x}$) of 0.72 and 0.30, respectively. Figures 5.17 and 5.18 show the comparison of the measured and estimated responses, for beam 2 with flaw, similar to Figures 5.15 and 5.16, respectively.

Table 5.5 Iteration details for beam 2 with flaw

Iteration no	Initial guess for flaw depth ratio	Flaw location ratio (corresponding element no.)	Equivalent flaw depth
1	0.99	0.26 (7)	0.96
2	0.96	0.27 (8)	0.91
3	0.91	0.33 (9)	0.867
4	0.867	0.33 (9)	0.86
5	0.86	No possible intersection	0.867

Identification of *flaw parameters*:

The flaw localization and sizing algorithm (Subsection 4.3.2) is applied to this example. The similar steps as in previous example are not repeated here for brevity. However, changes due to flaw location and size have been explained. By applying the

flaw localization and sizing procedure, finally converged flaw location and size are 0.33 (i.e., at 9th element) and 0.867, respectively, and is given in Table 5.5. Table 5.6 shows the estimation of the flaw location and the flaw size for different choices of excitation frequencies. The flaw localization is found to be nearly same in terms of element number. The flaw depth also is found to be good.

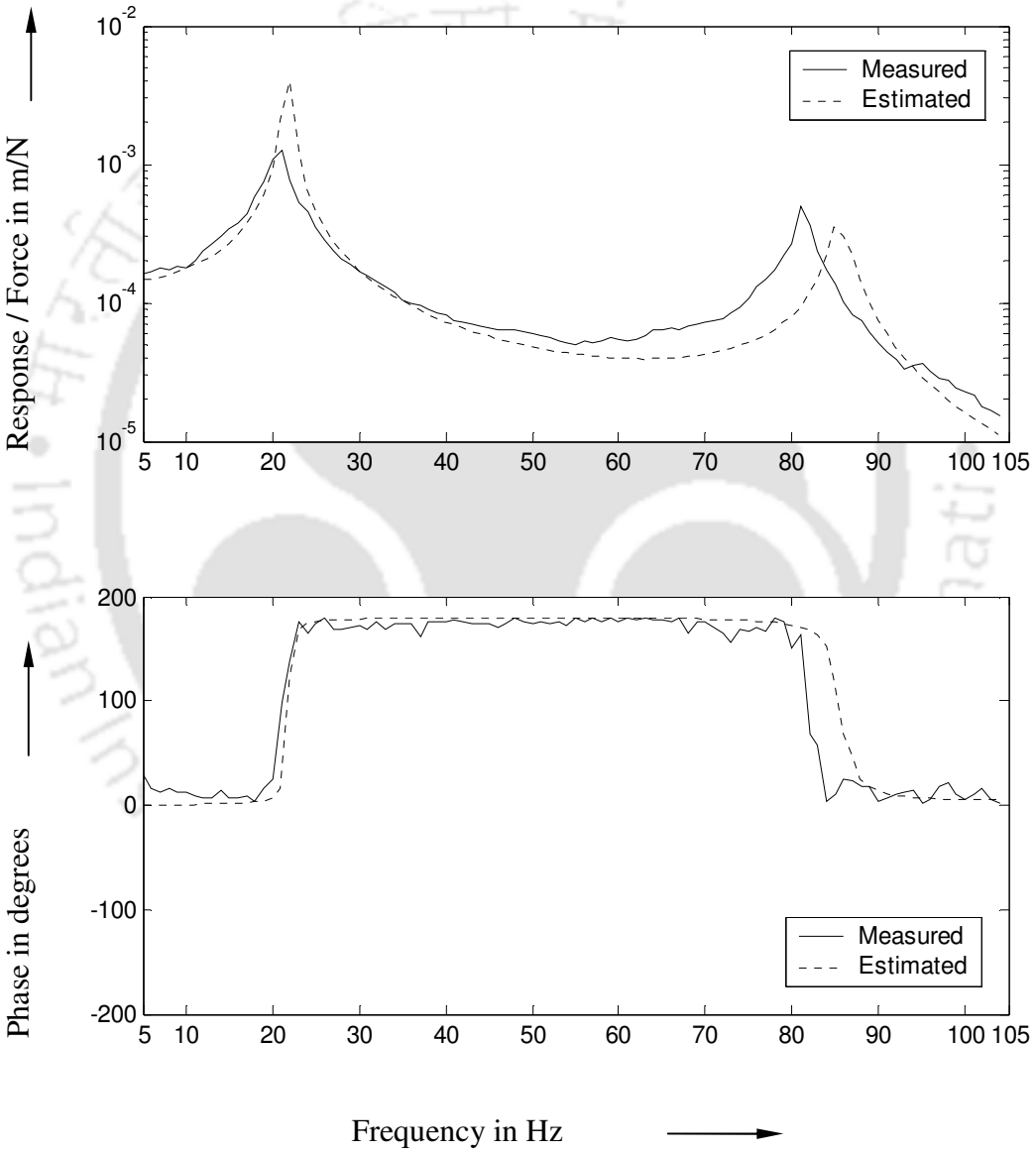

Figure 5.17 Frequency response function in vertical plane for beam 2 with flaw

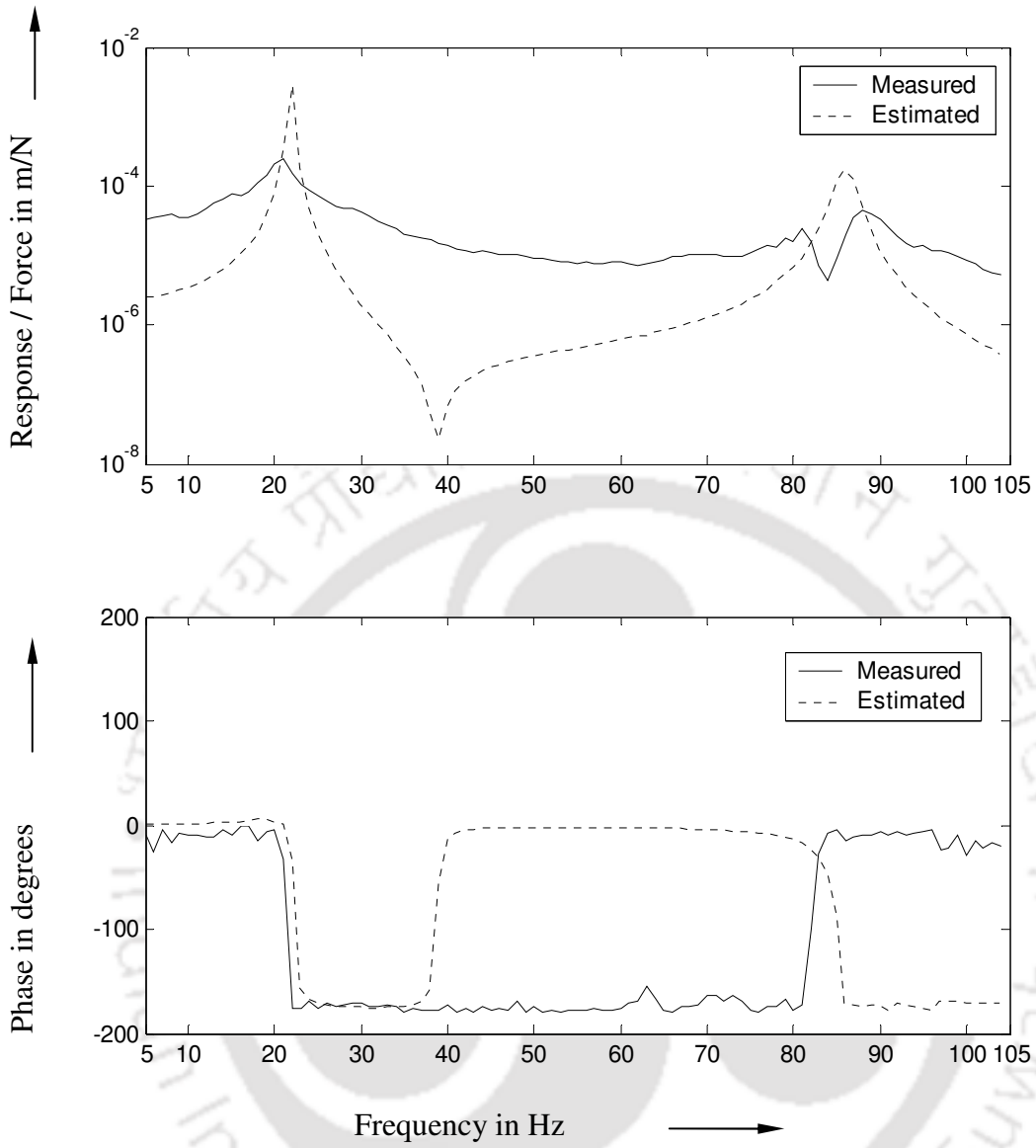

Figure 5.18 Frequency response function in horizontal plane for beam 2 with flaw

Higher resonance frequencies can also be used for the flaw location, however, number of possible flaw locations will be far more and the iteration time will be larger. The fundamental resonance frequency suffices for present identification method since its identification is up to the single flaw.

Table 5.6 Actual and estimated flaw parameters for beam 2 with flaw

Beam no.	Actual flaw parameters (approx.)		No. of ω (case)*	Estimated flaw and parameters											
				Flaw flexibility coefficients (C^{id} and C^{th}) †										$\bar{x}$ (n)	$\bar{a}_e$
	$\bar{x}$ (n)	$\bar{a}$		$C_{22}\,(\mathrm{mN}^{-1})$		$C_{33}\,(\mathrm{mN}^{-1})$		$C_{44}\,(\mathrm{mN})^{-1}$		$C_{45}\,(\mathrm{mN})^{-1}$ ($=C_{54}$)		$C_{55}\,(\mathrm{mN})^{-1}$			
				C_{22}^{id}	C_{22}^{th}	C_{33}^{id}	C_{33}^{th}	C_{44}^{id}	C_{44}^{th}	C_{45}^{id}	C_{45}^{th}	C_{55}^{id}	C_{55}^{th}		
1	0.33 (9)	0.72	5, (b)	1.040	1.031	1.557	1.544	3.841	3.814	8.335	8.333	15.760	15.684	0.33 (9)	0.867
			10, (b)	1.054	1.034	1.580	1.549	3.860	3.836	8.241	8.370	15.808	15.737	0.33 (9)	0.868
			5, (a)	1.044	1.034	0.984	1.549	3.975	3.836	8.486	8.370	15.778	15.737	0.33 (9)	0.868
			10, (a)	1.038	1.031	1.554	1.544	3.799	3.814	8.415	8.333	15.661	15.684	0.33 (9)	0.867

where ω is excitation frequencies, n is element number, and $\bar{a}_e$ is equivalent flaw depth ratio

* Cases (b) and (a) indicates before and after the first resonance condition, respectively;

† superscripts '*id*' and '*th*' indicate the estimated and theoretical, respectively.

5.6 Conclusions

The developed algorithm for the detection, localization and sizing of a flaw in beams based forced vibration, was verified based on experimental forced vibration measurements. The details of experimental setup and procedure have been provided. The damping ratio of the beam system was estimated experimentally and used to develop the system proportional (i.e., Rayleigh's) damping, which was assumed in the FE model.

Experimental measurements were correlated with numerically simulated measurements and used to update the theoretical model accordingly. The algorithm, with the updated finite element model, detected and identified the flaw parameters for two beams with different flaw location and size. The iteration details of the identification procedure are tabulated. The comparison of theoretical with identified flaw flexibility coefficients and actual with identified flaw locations and sizes were tabulated for the various excitation frequencies. The identification for the flaw detection, localization and sizing were in very good agreement with their actual counterpart.

CHAPTER 6

CONCLUSIONS AND FUTURE WORKS

6.1 Conclusions

A model based identification algorithm has been developed for detecting, localizing and sizing of a flaw in a beam. The Timoshenko beam theory along with the FEM has been used to model the beam with a flaw for transverse vibrations. The flaw model is given by the five standard flaw flexibility coefficients. The Rayleigh's damping has been considered in the beam model. The convergence of the flaw location and size has been obtained, iteratively. For an assumed flaw location, the regularization technique has been used to estimate the bounded value of flaw flexibility coefficients. The equivalent flaw size has been obtained from the flaw flexibility coefficients and is used to obtain a new flaw location during the iteration process. Numerically, the algorithm has been tested with the noise contamination in the free and forced responses and the error in measured resonance frequencies, for the beams having simply supported and cantilever end conditions.

Development of the identification algorithm has been carried out in such a way that it can be applied experimentally. First, the detection, localization, and quantification of the flaw have been done using free vibration measurements i.e., natural frequencies and mode shapes. Next, the practical difficulty in accurate measurement of mode shapes motivated to use forced response measurements for the

development of identification algorithm. However, the difficulty of accurate measurement of the rotational DOFs and inaccessible linear DOFs led to implementation of hybrid condensation schemes to eliminate these DOFs. Experimentally, the detection, localization, and sizing of the flaw have been carried out for two specimen beams, i.e., beam 1 and beam 2. Beam 1 has the flaw at the mid span, and beam 2 has the flaw at the 1/3rd span to observe the effects of the flaw on the first and second mode of vibrations, respectively. The measured forced response (i.e. resonance frequencies, and the amplitude and phase of forced responses) have been used in the algorithm.

Some of the conclusions arrived at the present study are given below:

- The increase in the flexibility causes decrease in natural frequencies of the structure and changes in mode shapes. Moreover, the flaw model considered for the analysis, introduces coupling of motions in two orthogonal planes even for symmetrical beams. This leads to doubling in natural frequencies (i.e., splitting of a natural frequency).
- The splitting of the natural frequency is found to be more when the location of the flaw is at the anti-nodal point of the mode shape as compared to nodal points.
- These shifts and splitting of natural frequencies of the structure with flaw could be used as the indication of flaws, however, it is difficult to get quantitative information about the flaw (i.e., the location and the size).
- Changes in mode shapes could be used for the location of flaws. However, accuracy depends on the measurement of mode shapes which is still difficult in practical applications. The measurement of forced vibrations of the

structure is comparatively easier in terms of limited number of sensors required for the response measurement and can be used to localize the flaw in a structure.

- The sensitivity of a (square of a) natural frequency is proportional to the square of the curvature of the corresponding mode shape, evaluated for the undamaged beam at the damaged cross-section by Morassi (1993). However, the primary reason for avoiding modal curvature in the present work is to the eliminate error that may result from numerical differentiation of mode shape data.
- In the case of forced vibrations also, the flaw causes the split in resonance frequencies and a change in phase of the order of 180° after the each resonances. This information could be used for both the detection and identification of flaws.
- Flaw flexibility coefficients are only the function of the flaw size and independent of the flaw location. However, the forced response depends upon both the flaw size and its location. Hence, initially the flaw location has to be assumed to obtain the flaw size and later iteratively it has to be refined.
- Regularization method has been found useful to estimate the bounded flaw flexibility coefficients, especially when there is noise contamination in the forced response and the crack location is approximate.
- The most of flaw identification techniques are based on changes in natural frequencies alone, which is a scalar quantity. For symmetric systems, flaw localization is difficult since natural frequencies alone will not have exact information of the flaw location. Since we will have same natural frequencies for the flaw placed at two symmetric locations.

- However, with the present identification algorithm this difficulty will not be there since forced responses (or mode shapes) will contain the location information even in symmetrically placed structures, since these are vector quantities.
- In case of simply supported beams, the flaw localization algorithm gives two choices for flaw locations for an assumed flaw size due to the symmetric property of the variation of natural frequencies. However, in case of cantilever beams, only one location of the flaw is obtained.
- In the case of multiple choices of flaw locations from the flaw localization algorithm, since forced responses do contain information regarding possible actual location of the flaw even in symmetrical structures in the form of distortion in responses more towards the flaw location. Hence the iteration can be started, from either one of the choice to achieve the convergence.
- In this work, the hybrid reduction scheme as proposed by Tiwari and Dharmaraju (2006) has been extended by including the damping to the crack localization and sizing algorithm based on purely the forced response measurements, which is a more controlled and accurate way of measurements. This is a major step toward development of the flaw identification method, which allowed the application of the method to the actual experimental data.
- In the undamped case, both eigen values and eigen vectors (i.e., mode shapes) are real. The mode-shape vector indicates the relative position of different masses at any given instant of time at a single natural frequency.
- In the present case, the proportional damping have been considered in the system for numerical illustration of the procedure. For this case eigen values are complex, however, eigen vectors remain real (or even if they are complex

they have at least 0^o or 180^o phase difference among various degree of freedoms at a single natural frequency). However, the present flaw identification algorithm is capable of handling even complex mode shapes as input, which we get from the modal testing from general damped systems.

- The system damping has negligible effect on the resonance frequencies; and marginal on the estimation flaw flexibility coefficients, and subsequently on the flaw location and the size.
- While there is error in the resonance frequency measurements, it introduces a shift in the location of the flaw during iterations. However, in the present algorithm, measurement error of 5 percent of the change (defined in terms of change in the natural frequency due to the flaw as compared to the intact beam) in natural frequencies has no appreciable effect on the estimation of flaw location.
- In order to minimize the discrepancies between theoretical FE model and experimental beam systems, the developed theoretical model has been updated by including the effect of support flexibility based on experimental measurements (i.e., by tuning the fundamental natural frequency of the numerical model and from the experimentation).
- The identification algorithm always over estimates the flaw size (i.e., comparatively more than the actually measured one). This is due to the fact that the equivalent flaw depth is corresponding to a fatigue flaw of negligible width and in actual case it has some finite width.
- The dynamic response frequency at resonance is compared with the natural frequency obtained through the classical closed form solutions, which are matching quite good (refer Appendix G).

- The response reproduction capabilities of the present algorithm have been found to be very good in most of the frequency range.

6.2 Limitations

The following are the limitations of the present methodology of flaw identification:

- The identification algorithm's success very much depends upon the accurate mathematical modeling of the actual system. In real case it will be challenging problem.
- In the experimentation an exciter was used to excite the beam, in some real situation this may not be practical. It would be more realistic, if identification of flaw parameters can be done with naturally available responses, in that case measurement of support force may be required.
- In the experimentation the support dynamic parameters where obtained by curve fitting the experimental response and the numerical response by trial and error method. More advanced available technique could be used to obtain the support dynamic parameters to improve the mathematical model.
- The present identification algorithm requires accurate measurement of forced response and the location of resonance. The success of the present algorithm very much depends upon the accurate measurement of vibration responses since it is based on the mathematical model of the system. Other feature based flaw identification methods depends on trend of these vibration responses so even some error in measurement is tolerable.
- The identification algorithm for flaw parameters requires the measurements at various location of the test structure. Hence, it becomes necessary to have such

arrangements (i.e., more number of sensors and fixture setup, input channels of DAQ, space requirements, etc.), when these are intended to be applied in field. These instrumentation is costly and is not portable.

- In most of the engineering structures the damping is relatively less, and hence the measurement natural frequency is relatively accurate. However, with heavily damped beam, the measurement of natural frequency will have more error.
- The implementation of condensation schemes (Chapter 4) introduces some error in prediction of the flaw parameters.
- The experimental investigation of the present work is more of academic and it requires careful implementation to more complicated practical structures, which incorporate more structural unknowns such as the real boundary conditions, material parameters, and others which affect the free and forced vibration behavior.

6.3 Scopes for Future Work

- The present work can be extended to include the study of the influence of flaws on the axial and torsional vibrations of beams.
- Various types of flaw models available for other types of flaws such as the longitudinal, circumferential, slant, gaping cracks, etc. can be used as an extension of the present algorithm.
- Identification of flaw parameters of multiple flaws can be carried out. More information from vibration measurements, such as second resonance frequencies and forced responses of few more excitation frequencies will be required for the localization and sizing algorithm.
- The effect of support flexibility on estimation flaw parameters could be studied. Since the support condition of the beam is assumed by theoretical bearing stiffness, identification procedures could be developed to estimate the stiffness coefficients along with flaw flexibility coefficients.
- Development of identification algorithms could be attempted for rotating beams/rotors with flaws. When the beam is rotated, subsequently transverse surface flaw opens and closes (i.e., breaths), and the identification procedure to estimate the time dependent of the flaw flexibility coefficients could be carried out.
- The identification algorithm for the beam could be extended for other types of structures such as, pipes, shell, turbine blades, plates etc. The effect of environment (especially change in temperatures) changes on the vibration response can be explored.

APPENDIX A

FLEXIBILITY COEFFICIENTS OF AN OPEN CRACK

The Dimensionless terms of the flexibility matrix $[\bar{C}]$ are given by Papadopoulos and Dimarogonas (1987),

$$\bar{C}_{22} = \frac{\pi E R^3 C_{22}}{(1-\nu^2)} = 4\int_0^{\bar{a}}\int_0^{\bar{b}} \bar{y} F_{III}^2(\bar{h})\, d\bar{z}\, d\bar{y}\,; \qquad \bar{C}_{33} = \frac{\pi E R^3 C_{33}}{(1-\nu^2)} = 4\int_0^{\bar{a}}\int_0^{\bar{b}} \bar{y} F_{II}^2(\bar{h})\, d\bar{z}\, d\bar{y}\,;$$

$$\bar{C}_{44} = \frac{\pi E R^3 C_{44}}{(1-\nu^2)} = 32\int_0^{\bar{a}}\int_0^{\bar{b}} \bar{z}^2 \bar{y} F_1^2(\bar{h})\, d\bar{z}\, d\bar{y}\,;$$

$$\bar{C}_{45} = \bar{C}_{54} = \frac{\pi E R^2 C_{45}}{(1-\nu^2)} = 64\int_0^{\bar{a}}\int_0^{\bar{b}} \bar{z}\, \bar{y} \sqrt{1-\bar{z}^2}\, F_1(\bar{h}) F_2(\bar{h})\, d\bar{z}\, d\bar{y}\,;$$

$$\bar{C}_{55} = \frac{\pi E R^3 C_{55}}{(1-\nu^2)} = 64\int_0^{\bar{a}}\int_0^{\bar{b}} \bar{y}(1-\bar{z}^2) F_2^2(\bar{h})\, d\bar{z}\, d\bar{y}\,; \qquad \text{(A.1)}$$

where

$$\bar{z} = z/R, \qquad \bar{a} = a/R, \qquad \bar{y} = y/R, \qquad \bar{b} = b/R, \qquad \bar{h} = h/R. \qquad \text{(A.2)}$$

$$F_1\left(\frac{\alpha}{h}\right) = \sqrt{\frac{\tan\lambda}{\lambda}}\left[0.752 + 2.02\left(\frac{\alpha}{h}\right) + 0.37(1-\sin\lambda)^3\right] \Big/ \cos\lambda$$

$$F_2\left(\frac{\alpha}{h}\right) = \sqrt{\frac{\tan\lambda}{\lambda}}\left[0.923 + 0.199(1-\sin\lambda)^4\right] \Big/ \cos\lambda.$$

$$F_{II}\left(\frac{\alpha}{h}\right)=\left[1.122-0.561\left(\frac{\alpha}{h}\right)+0.085\left(\frac{\alpha}{h}\right)^{2}+0.18\left(\frac{\alpha}{h}\right)^{3}\right]\Big/\sqrt{1-\left(\frac{\alpha}{h}\right)}.$$

$$F_{III}\left(\frac{\alpha}{h}\right)=\sqrt{\frac{\tan\lambda}{\lambda}}.$$

and

$$\lambda=\frac{\pi\alpha}{2h} \quad \text{as given in Tada et al. (2000)} \tag{A.3}$$

where R is the radius of the beam of circular cross section, h is the height of assumed elemental strip, a is the crack depth, $2b$ is the width of the elemental strip and α is the local crack depth which varies along the cross section (refer Figure 2.2).

APPENDIX B

RAYLEIGH DAMPING

The relation between damping ratio, ζ, and natural frequency, ω_n, is expressed as Clough and Penzien (1993)

$$\zeta_n = \frac{a_0}{2\omega_n} + \frac{a_1 \omega_n}{2} \tag{B.1}$$

where a_0 and a_1 are Rayleigh damping factors and this can be evaluated by the solution of a pair of simultaneous equations, if the damping ratios ζ_m and ζ_n associated with two specific known frequencies ω_m and ω_n. Writing equation (B.1) for each of these two cases and expressing them in the matrix form leads to

$$\begin{Bmatrix} \zeta_m \\ \zeta_n \end{Bmatrix} = \frac{1}{2}\begin{bmatrix} 1/\omega_m & \omega_m \\ 1/\omega_n & \omega_n \end{bmatrix}\begin{Bmatrix} a_0 \\ a_1 \end{Bmatrix} \tag{B.2}$$

from Equation (B.2), a_0 and a_1 can be obtained as,

$$\begin{Bmatrix} a_0 \\ a_1 \end{Bmatrix} = 2\frac{\omega_m \omega_n}{\omega_n^2 - \omega_m^2}\begin{bmatrix} \omega_n & -\omega_m \\ -1/\omega_n & 1/\omega_m \end{bmatrix}\begin{Bmatrix} \zeta_m \\ \zeta_n \end{Bmatrix} \tag{B.3}$$

where ω_m and ω_n are the system fundamental and highest natural frequencies of interest.

APPENDIX C

TIKHONOV'S REGULARIZATION METHOD

The linear least-squares problem of equation

$$[A_1]\{\gamma\} = \{d_1\} \tag{C.1}$$

to determine the flaw flexibility coefficients is ill-posed hence the solution is sensitive to noise contamination and measurement errors in response. Hence the regularization is imperative for a stabilized solution. In Tikhonov's regularization method the regularized solution $\{\gamma\}$ is a solution to the following weighted combination of the residual norm and the side constraint

$$\min \{ \|A_1\gamma - d_1\|_2^2 + \eta^2 \|L_r(\gamma - \bar{\gamma})\|_2^2 \} \tag{C.2}$$

where L_r is the identity matrix I_n, $\bar{\gamma}$ is a initial estimate of the solution obtained from the assumed dynamic parameters and η is the regularization parameter that controls the relative minimization of the side constraint with respect to the residual norm. η is obtained from the *L-curve* aids in seeking a compromise between the minimization of the two norms $\|L_r(\gamma)\|_2$ and $\|A_1\gamma - d_1\|_2$. In the algorithm for the Tikhonov's method the singular value decomposition (SVD) of matrix $[A_1]$ of the form

$$[A_1] = U\sum V^T = \sum_{i=1}^{n} u_i \sigma_i v_i^T \quad \text{(C.3)}$$

is used where $U=(U_1,...,U_n)$ and $V=(V_1,...,V_n)$ are matrices with orthonormal columns of right and left singular vectors of A such that $U^TU=V^TV=I_n$ and $\sum=\text{diag}(\sigma_1,...,\sigma_n)$ has non-negative singular values of A. Tikhonov's method produces a regularized solution

$$x_\eta = \sum_{i=1}^{n} f_i \frac{U_i^T b_1}{\sigma_i} V_i \quad \text{(C.4)}$$

where $f_i = \dfrac{\sigma_i^2}{(\sigma_i^2+\eta^2)}$ are filter factors and the filtering sets in for $\sigma_i < \eta$.

APPENDIX D

MASS AND STIFFNESS MATRICES AND DISPLACEMENT VECTOR OF THE TIMOSHENKO BEAM ELEMENT

D.1 Elemental Mass and Stiffness Matrices for Transverse Vibrations

The element mass matrix $[M]^{(e)}$ consists of the translational mass matrix $[M_T]^{(e)}$ and the rotational mass matrix $[M_R]^{(e)}$, which is given as

$$[M]^{(e)} = [M_T]^{(e)} + [M_R]^{(e)} \tag{D.1}$$

with

$$[M_T]^{(e)} = [M_T]_0 + \Phi[M_T]_1 + \Phi^2[M_T]_2$$

and

$$[M_R]^{(e)} = [M_R]_0 + \Phi[M_R]_1 + \Phi^2[M_R]_2$$

The element translational mass matrix $[M_T]^{(e)}$

$$[M_T]_0 = \frac{\rho Al}{420(1+\Phi)^2}\begin{bmatrix} 156 & & SYM. & \\ 22l & 4l^2 & & \\ 54 & 13l & 156 & \\ -13l & -3l^2 & -22l & 4l^2 \end{bmatrix};$$

$$[M_T]_1 = \frac{\rho Al}{420(1+\Phi)^2}\begin{bmatrix} 294 & & SYM. & \\ 38.5l & 7l^2 & & \\ 126 & 31.5l & 294 & \\ -31.5l & -7l^2 & -38.5l & 7l^2 \end{bmatrix}$$

$$[M_T]_2 = \frac{\rho Al}{420(1+\Phi)^2}\begin{bmatrix} 140 & & SYM. & \\ 17.5l & 3.5l^2 & & \\ 70 & 17.5l & 140 & \\ -17.5l & -3.5l^2 & -17.5l & 3.5l^2 \end{bmatrix} \quad \text{(D.2)}$$

The element rotational mass matrix $[M_R]^{(e)}$

$$[M_R]_0 = \frac{\rho I_d}{(1+\Phi)^2}\begin{bmatrix} 6/5l & & SYM. & \\ 1/10 & 2l/15 & & \\ -6/5l & -1/10 & 6/5l & \\ 1/10 & -l/30 & -1/10 & l/15 \end{bmatrix};$$

$$[M_R]_1 = \frac{\rho I_d}{(1+\Phi)^2}\begin{bmatrix} 0 & & SYM. & \\ -1/2 & l/6 & & \\ 0 & 1/2 & 0 & \\ -1/2 & -l/6 & 1/2 & l/6 \end{bmatrix};$$

$$[M_R]_2 = \frac{\rho I_d}{(1+\Phi)^2}\begin{bmatrix} 0 & & SYM. & \\ 0 & l/3 & & \\ 0 & 0 & 0 & \\ 0 & l/6 & 1/2 & l/6 \end{bmatrix} \tag{D.3}$$

The element stiffness matrix $[K_{wf}]^{(e)}$

The element stiffness matrix $[K_{wf}]^{(e)}$ can be expressed as

$$[K_{wf}]^{(e)} = [K_{wf}]_0 + \Phi[K_{wf}]_1 \tag{D.4}$$

where

$$[K_{wf}]_0 = \frac{EI}{(1+\Phi)l^3}\begin{bmatrix} 12 & & SYM. & \\ 6l & 4l^2 & & \\ -12 & -6l & 12 & \\ 6l & 2l^2 & -6l & 4l^2 \end{bmatrix};$$

$$[K_{wf}]_1 = \frac{EI}{(1+\Phi)l^3}\begin{bmatrix} 0 & & SYM. & \\ 0 & l^2 & & \\ 0 & 0 & 0 & \\ 0 & -l^2 & 0 & l^2 \end{bmatrix}$$

$$\Phi = \frac{12EI}{k_{sc}GAl^2} \qquad \text{and} \qquad k_{sc} = \frac{6(1+\nu)}{7+6\nu}$$

where EI is the flexural rigidity of the beam, l is the element length, A is the cross sectional area of the beam, G is the modulus of rigidity of the beam material, ρ is the

mass density of the beam material, k_{sc} is the shear correction factor for the circular cross section and ν is the Poisson's ratio .

D.2 Elemental Displacement Vector for Transverse Vibrations

The element displacement vector $\{q\}^{(e)}$

The element displacement vector for transverse vibrations can be written as

$$\{q\}^{(e)} = \{v_1 \quad \theta_1 \quad v_2 \quad \theta_2\}^T \tag{D.5}$$

APPENDIX E

DYNAMIC AND HYBRID CONDENSATIONS

E.1 Dynamic Condensation

Equation (4.3) can be expanded into two equations, as

$$-\omega^2[M_{mm}]\{\hat{Q}_m\}-\omega^2[M_{ms}]\{\hat{Q}_s\}+[K_{mm}]\{\hat{Q}_m\}+[K_{ms}]\{\hat{Q}_s\}=\{\hat{F}_m\} \tag{E.1}$$

and

$$-\omega^2[M_{sm}]\{\hat{Q}_m\}-\omega^2[M_{ss}]\{\hat{Q}_s\}+[K_{sm}]\{\hat{Q}_m\}+[K_{ss}]\{\hat{Q}_s\}=\{0\}$$

Equation (E.1) can be rearranged as

$$\{\hat{Q}_s\}=-\left(-\omega^2[M_{ss}]+[K_{ss}]\right)^{-1}\left(-\omega^2[M_{sm}]+[K_{sm}]\right)\{\hat{Q}_m\} \tag{E.2}$$

with an identity equation

$$\{\hat{Q}_s\}=[I]\{\hat{Q}_m\} \tag{E.3}$$

Equations (E.2) and (E.3) can be combined as

$$\begin{Bmatrix} \hat{Q}_m \\ \hat{Q}_s \end{Bmatrix} = [T^d]\{\hat{Q}_m\} \tag{E.4}$$

with

$$[T^d] = \begin{bmatrix} [I] \\ \cdots\cdots\cdots\cdots\cdots\cdots\cdots\cdots\cdots\cdots \\ -\left(-\omega^2[\hat{M}_{ss}]+[\hat{K}_{ss}]\right)^{-1}\left(-\omega^2[\hat{M}_{sm}]+[\hat{K}_{sm}]\right) \end{bmatrix}$$

where $[T^d]$ is the dynamic transformation matrix relating master DOFs with all DOFs of all elements.

E.2 Hybrid Condensation

Equation (4.7) can be expanded as

$$-\omega^2[\bar{M}_{mm}]\{\bar{Q}_m^h\} - \omega^2[\bar{M}_{ms}]\{\bar{Q}_s^h\} + [\bar{K}_{mm}]_{wf}\{\bar{Q}_m^h\} + [\bar{K}_{ms}]_{wf}\{\bar{Q}_s^h\} = \{\bar{F}_m^h\} \tag{E.6}$$

and

$$-\omega^2[\bar{M}_{sm}]\{\bar{Q}_m^h\} - \omega^2[\bar{M}_{ss}]\{\bar{Q}_s^h\} + [\bar{K}_{sm}]_{wf}\{\bar{Q}_m^h\} + [\bar{K}_{ss}]_{wf}\{\bar{Q}_s^h\} = \{0\} \tag{E.7}$$

Equation (E.7) can be written as

$$\{\bar{Q}_s^h\} = -\left(-\omega^2[\bar{M}_{ss}] + [\bar{K}_{ss}]_{wf}\right)^{-1}\left(-\omega^2[\bar{M}_{sm}] + [\bar{K}_{sm}]_{wf}\right)\{\bar{Q}_m^h\} \tag{E.8}$$

with an identity equation

$$\{\bar{Q}_s^h\} = [I]\{\bar{Q}_m^h\} \tag{E.9}$$

Equations (E.8) and (E.9) can be combined to give

$$\begin{Bmatrix}\bar{Q}_m^h \\ \bar{Q}_s^h\end{Bmatrix} = [T^h]\{\bar{Q}_m^h\} \tag{E.10}$$

with

$$[T^h] = \begin{bmatrix} [I] \\ \cdots\cdots\cdots\cdots\cdots\cdots\cdots\cdots\cdots\cdots \\ -\left(-\omega^2[\bar{M}_{ss}] + [\bar{K}_{ss}]_{wf}\right)^{-1}\left(-\omega^2[\bar{M}_{sm}] + [\bar{K}_{sm}]_{wf}\right) \end{bmatrix}$$

where $[T^h]$ is the hybrid transformation matrix relating master DOFs (i.e. translational DOFs) and all DOFs (i.e. the translational and the rotational) at the beam element with flaw.

APPENDIX F

INTERMEDIATE STEPS IN THE PROPOSED ALGORITHM

The detail of the procedure is explained in Subsection 2.3.3 (Page 71) along with the flow chart in Fig. 2.4 (Page 73). With respect to the specific example of the simply supported and cantilever beams are now given as follows,

F.1 Intermediate Steps of the Algorithm in Chapter 2

2.4.1 Simply Supported Beam

1. For illustration purpose from Table 2.5 for Case no. 7, flaw depth ratio $\bar{a} = 0.7$ and flaw location ratio $\bar{x} = 0.4$ (i.e. 12^{th} element) are assumed for the numerical experiment. The fundamental transverse natural frequency obtained is 19.96 Hz, and first two mode shapes are shown Figures 2.5 and 2.6. These are obtained from equation (2.14).
2. These modal parameters so obtained in Step 1 are treated as experimentally measured from a beam with unknown flaw parameters (i.e., the flaw location and its size). Now the aim is to get back the assumed flaw parameters (i.e., the flaw depth ratio, $\bar{a}$, and flaw location ratio, $\bar{x}$) by using the flaw localization and sizing algorithm with the measured modal parameters of Step 1.
3. From the finite element model of the beam with flaw, the fundamental transverse natural frequency is obtained for a particular value of an initial guess

of 0.9 for flaw depth and for different possible values of flaw locations (from element no.1 to 30).

6. As shown in Figure 2.8, the experimentally obtained transverse natural frequency of step is matched with computational natural frequencies (which are obtained by the FEM in step 3), which gives two possible flaw locations 0.23 (7^{th} element) and 0.80 (24^{th} element).

7. One of the possible flaw locations (i.e. 0.23 (7^{th} element)) obtained in Step 4 is used (the other choice for the flaw locations, 0.80 (24^{th} element) can also be used) by the identification algorithm (Steps 6&7) to obtain an updated value of the assumed flaw depth ratio.

8. In Subsection 2.3.1 (i.e., identification algorithm for flaw sizing), the numerically generated mode shapes are utilized by equation (2.18) in which the vector $\{Q_f\}^{(e)}$ is the member of the system eigen vector $\{h_0\}$ of equation (2.14).

9. Flaw flexibility coefficients are obtained using equation (2.27) and subsequently the equivalent flaw depth ratio (i.e., $\bar{a}_e$ = 0.71, see Table 2.3) is obtained using equation (2.30).

10. With the new value of the equivalent flaw depth ratio obtained in Step 7 (i.e., $\bar{a}_e$ =0.71, which is now treated as initial guess for next iteration), now again Steps 3 to 7 are repeated and the iterations continue until the convergence of

the flaw size is achieved up to the desired level of accuracy of 0.01 and simultaneously the same element number for the flaw location in two consecutive iterations. The converged flaw parameters are (see Table 2.3): flaw location ratio $\bar{x} = 0.40$ (i.e., 12^{th} element) and equivalent flaw depth ratio $\bar{a}_e = 0.71$.

2.4.2 Cantilever Beam

1. For illustration purpose from Table 2.7 for Case no. 8, flaw depth ratio $\bar{a} = 0.8$ and flaw location ratio $\bar{x} = 0.3$ (i.e. 9^{th} element) are assumed for the numerical experiment. The fundamental transverse natural frequency obtained is 7.11 Hz, and first two mode shapes (i.e. eigen vector $\{h_0\}$) are shown Figures 2.9 and 2.10. These are obtained from equation (2.14).

2. These modal parameters so obtained in step 1 are treated as experimentally measured from a beam with unknown flaw parameters (i.e., the flaw location and its size). Now the aim is to get back the assumed flaw parameters (i.e., the flaw depth ratio, $\bar{a}$, and flaw location ratio, $\bar{x}$) by using the flaw localization and sizing algorithm with the measured modal parameters of step 1.

3. From the finite element model of the beam with flaw, the fundamental transverse natural frequency is obtained for a particular value of an initial guess of 0.9 for flaw depth and for different possible values of flaw locations (from element no.1 to 30).

4. As shown in Figure 2.12, the experimentally obtained transverse natural frequency of step is matched with computational natural frequencies (which are obtained by the FEM in step 3), which gives possible flaw location 0.17 (5^{th} element).

5. The possible flaw location (i.e. 0.17 (5^{th} element)) obtained in Step 4 is used by the identification algorithm (Steps 6&7) to obtain an updated value of the assumed flaw depth ratio.

6. In Subsection 2.3.1 (i.e., the identification algorithm for flaw sizing), the numerically generated mode shapes are utilized by equation (2.18) in which the vector $\{Q_f\}^{(e)}$ is member of the system eigen vector $\{h_0\}$ of equation (2.14).

7. Flaw flexibility coefficients are obtained using equation (2.27) and subsequently the equivalent flaw depth ratio is obtained using equation (2.30).

8. With the new value of the equivalent flaw depth ratio (which is now treated as initial guess for next iteration) obtained in Step 7, now again Steps 3 to 7 are repeated and the iterations continue until the convergence of the flaw size is achieved up to the desired level of accuracy of 0.01 and simultaneously the same element number for the flaw location in two consecutive iterations. The converged flaw parameters are (see Table 2.7): flaw location ratio $\bar{x} = 0.30$ (i.e., 9^{th} element) and equivalent flaw depth ratio $\bar{a}_e = 0.79$.

F.2 Intermediate Steps of the Algorithm in Chapter 3

3.4.1 Simply Supported Beam

1. For illustration purpose from Table 3.3 for Case no. 7, flaw depth ratio $\bar{a} = 0.7$ and flaw location ratio $\bar{x} = 0.4$ (i.e. 12^{th} element) are assumed for the numerical experiment. The fundamental transverse natural frequency obtained is 19.96 Hz from equation (2.14), and forced responses (i.e. vector $\{Q\}$) as shown Figures 3.1 and 3.2 are obtained from equation (3.12).

2. These parameters so obtained in step 1 are treated as experimentally measured from a beam with unknown flaw parameters (i.e., the flaw location and its size). Now the aim is to get back the assumed flaw parameters (i.e., the flaw depth ratio, $\bar{a}$, and flaw location ratio, $\bar{x}$) by using the flaw localization and sizing algorithm with the measured first natural frequency and force response of step 1.

3. From the finite element model of the beam with flaw, the fundamental transverse natural frequency is obtained for a particular value of an initial guess of 0.9 for flaw depth and for different possible values of flaw locations (from element no.1 to 30).

4. As shown in Figure 2.8, the experimentally obtained transverse natural frequency of step is matched with computational natural frequencies (which

are obtained by the FEM in step 3), which gives two possible flaw locations 0.23 (7^{th} element) and 0.80 (24^{th} element).

5. One of the possible flaw locations (i.e. 0.23 (7^{th} element)) obtained in Step 4 is used (the other choice for the flaw locations, 0.80 (24^{th} element) can also be used) by the identification algorithm (Steps 6&7) to obtain an updated value of the assumed flaw depth ratio.

6. In Subsection 3.3.1 (i.e., the identification algorithm for flaw sizing), the numerically generated forced responses (denoted by the vector $\{Q\}$)) are utilized by equation (3.13).

7. Flaw flexibility coefficients are obtained using equation (3.16) and subsequently the equivalent flaw depth ratio (i.e., $\bar{a}_e$ = 0.86, see Table 3.2) is obtained using equation (2.30).

8. With the new value of the equivalent flaw depth ratio obtained in Step 7 (i.e., $\bar{a}_e$ =0.86, which is now treated as initial guess for next iteration), now again Steps 3 to 7 are repeated and the iterations continue until the convergence of the flaw size is achieved up to the desired level of accuracy of 0.01 and simultaneously the same element number for the flaw location in two consecutive iterations. The converged flaw parameters are (see Table 3.2): flaw location ratio $\bar{x}$ = 0.40 (i.e., 12^{th} element) and equivalent flaw depth ratio $\bar{a}_e$ = 0.72.

3.4.2 Cantilever Beam

1. For illustration purpose from Table 3.4 for Case no. 8, flaw depth ratio $\bar{a} = 0.8$ and flaw location ratio $\bar{x} = 0.3$ (i.e. 9th element) are assumed for the numerical experiment. The fundamental transverse natural frequency obtained is 7.11 Hz, from equation (2.14), and forced responses (i.e. vector $\{Q\}$) as shown Figure 3.4 are obtained from equation (3.12).

2. These parameters so obtained in Step 1 are treated as experimentally measured from a beam with unknown flaw parameters (i.e., the flaw location and its size). Now the aim is to get back the assumed flaw parameters (i.e., the flaw depth ratio, $\bar{a}$, and flaw location ratio, $\bar{x}$) by using the flaw localization and sizing algorithm with the measured first natural frequency and force response of Step 1.

3. From the finite element model of the beam with flaw, the fundamental transverse natural frequency is obtained for a particular value of an initial guess of 0.9 for flaw depth and for different possible values of flaw locations (from element no.1 to 30).

4. As shown in Figure 2.12, the experimentally obtained transverse natural frequency of step is matched with computational natural frequencies (which are obtained by the FEM in step 3), which gives possible flaw location 0.17 (5th element).

5. The possible flaw location (i.e. 0.17 (5^{th} element)) obtained in Step 4 is used by the identification algorithm (Steps 6&7) to obtain an updated value of the assumed flaw depth ratio.

6. In Subsection 3.3.1 (i.e., the identification algorithm for flaw sizing), the numerically generated forced responses (denoted by the vector $\{Q\}$)) are utilized by equation (3.13).

7. Flaw flexibility coefficients are obtained using equation (3.16) and subsequently the equivalent flaw depth ratio is obtained using equation (2.30).

8. With the new value of the equivalent flaw depth ratio (which is now treated as initial guess for next iteration) obtained in Step 7, now again Steps 3 to 7 are repeated and the iterations continue until the convergence of the flaw size is achieved up to the desired level of accuracy of 0.01 and simultaneously the same element number for the flaw location in two consecutive iterations. The converged flaw parameters are (see Table 3.4): flaw location ratio $\bar{x}$ = 0.33 (i.e., 10^{th} element) and equivalent flaw depth ratio $\bar{a}_e$ = 0.81.

F.3 Intermediate Steps of the Algorithm in Chapter 4

4.4.1 Simply Supported Beam

1. For illustration purpose from Table 4.3 for Case no. 7, flaw depth ratio $\bar{a}$ = 0.7 and flaw location ratio $\bar{x}$ = 0.4 (i.e. 12^{th} element) are assumed for the

numerical experiment. The fundamental transverse natural frequency obtained is 19.96 Hz from equation (2.14), and forced responses (i.e. vector $\{Q\}$) as shown Figures 4.1 and 4.2 are obtained from equation (4.1).

2. These parameters so obtained in Step 1 are treated as experimentally measured from a beam with unknown flaw parameters (i.e., the flaw location and its size). Now the aim is to get back the assumed flaw parameters (i.e., the flaw depth ratio, $\bar{a}$, and flaw location ratio, $\bar{x}$) by using the flaw localization and sizing algorithm with the measured first natural frequency and force response of Step 1.

3. From the finite element model of the beam with flaw, the fundamental transverse natural frequency is obtained for a particular value of an initial guess of 0.9 for flaw depth and for different possible values of flaw locations (from element no.1 to 30).

4. As shown in Figure 2.8, the experimentally obtained transverse natural frequency of step is matched with computational natural frequencies (which are obtained by the FEM in step 3), which gives two possible flaw locations 0.23 (7^{th} element) and 0.80 (24^{th} element).

5. One of the possible flaw locations (i.e. 0.23 (7^{th} element)) obtained in Step 4 is used (the other choice for the flaw locations, 0.80 (24^{th} element) can also be used) by the identification algorithm (Steps 6&7) to obtain an updated value of the assumed flaw depth ratio.

6. In Subsection 4.3.1 (i.e., the identification algorithm for flaw sizing), the numerically generated forced responses (denoted by the vector $\{Q\}$)) are utilized by equation (4.1).

7. Flaw flexibility coefficients are obtained using equation (4.24) and subsequently the equivalent flaw depth ratio (i.e., $\bar{a}_e$ = 0.77, see Table 4.2) is obtained using equation (2.30).

8. With the new value of the equivalent flaw depth ratio (i.e. $\bar{a}_e$ =0.77, which is now treated as initial guess for next iteration) obtained in Step 7, now again Steps 3 to 7 are repeated and the iterations continue until the convergence of the flaw size is achieved up to the desired level of accuracy of 0.01 and simultaneously the same element number for the flaw location in two consecutive iterations. The converged value (as given in Table 4.2) of flaw location ratio $\bar{x}$ = 0.40 (i.e.12th element) and equivalent flaw depth ratio $\bar{a}_e$ = 0.71.

4.4.2 Cantilever Beam

1. For illustration purpose from Table 4.4 for Case no. 8, flaw depth ratio $\bar{a}$ = 0.8 and flaw location ratio $\bar{x}$ = 0.3 (i.e. 9th element) are assumed for the numerical experiment. The fundamental transverse natural frequency obtained is 7.11 Hz, from equation (2.14), and forced responses (i.e. vector $\{Q\}$) as shown Figure 4.4 are obtained from equation (4.1).

2. These parameters so obtained in Step 1 are treated as experimentally measured from a beam with unknown flaw parameters (i.e., the flaw location and its size). Now the aim is to get back the assumed flaw parameters (i.e., the flaw depth ratio, $\bar{a}$, and flaw location ratio, $\bar{x}$) by using the flaw localization and sizing algorithm with the measured first natural frequency and forced responses of Step 1.

3. From the finite element model of the beam with flaw, the fundamental transverse natural frequency is obtained for a particular value of an initial guess of 0.9 for flaw depth and for different possible values of flaw locations (from element no.1 to 30).

4. As shown in Figure 2.12, the experimentally obtained transverse natural frequency of step is matched with computational natural frequencies (which are obtained by the FEM in step 3), which gives possible flaw location 0.17 (5^{th} element).

5. The possible flaw location (i.e. 0.17 (5^{th} element)) obtained in Step 4 is used by the identification algorithm (Steps 6&7) to obtain an updated value of the assumed flaw depth ratio.

6. In Subsection 4.3.1 (i.e., the identification algorithm for flaw sizing), the numerically generated forced responses (denoted by the vector $\{Q\}$)) are utilized by equation (4.1).

7. Flaw flexibility coefficients are obtained using equation (4.24) and subsequently the equivalent flaw depth ratio is obtained using equation (2.30).
8. With the new value of the equivalent flaw depth ratio (which is now treated as initial guess for next iteration) obtained in Step 7, now again Steps 3 to 7 are repeated and the iterations continue until the convergence of the flaw size is achieved up to the desired level of accuracy of 0.01 and simultaneously the same element number for the flaw location in two consecutive iterations. The converged flaw parameters are (see Table 4.4): flaw location ratio $\bar{x} = 0.30$ (i.e., 9^{th} element) and equivalent flaw depth ratio $\bar{a}_e = 0.80$.

APPENDIX G

CLASSICAL SOLUTION OF NATURAL FREQUENCIES FOR A SIMPLY SUPPORTED TIMOSHENKO BEAM

The classical closed form solution for natural frequencies of the simply supported continuous Timoshenko beam can be obtained by solving the following characteristic equation as given by Inman (2001)

$$\omega_n^4 \frac{\rho r^2}{k_{sc}^2 G} - \left(1 + \frac{n^2\pi^2 r^2}{L^2} + \frac{n^2\pi^2 r^2}{L^2}\frac{E}{k_{sc}^2 G}\right)\omega_n^2 + \frac{\alpha^2 n^4 \pi^4}{L^4} = 0 \qquad \text{(G.1)}$$

with r and α is defined by

$$r^2 = \frac{I}{A} \qquad \text{and} \qquad \alpha^2 = \frac{EI}{\rho A} \qquad \text{(G.2)}$$

where ω_n is the natural frequency associated with n^{th} mode of vibration, L is the beam span, and other notations E, I, A, ρ and k_{sc} are same as already defined in the main text.

BIBLIOGRAPHY

Abraham, O. N. L., Brandon, J. A., and Cohen, A. M., Remark on the determination of compliance coefficients at the crack section of a uniform beam with circular cross-section, *Journal of Sound Vibration* 1994; 169(4), 570–574.

Adams, R. D., Cawley, P., Pye, C. J., and Stone, B. J., A vibration technique for non-destructively assessing the integrity of structures, *Journal of Mechanical Engineering Science* 1978; 20, 93-100.

Adhikari, S., Damping models for structural vibration, *Ph. D thesis, Engineering Department, Cambridge University*, 2000.

Alvandi, A., and Cremona, C., Assessment of vibration-based damage identification techniques, *Journal of Sound and Vibration* 2006; 292, 179-202.

Bachschmid, N., Pennacchi, P., and Vania, A., Identification of multiple faults in rotor systems, *Journal of Sound and Vibration* 2002; 254(2), 327-366.

Bachschmid, N., Mazza, M., and Tanzi, E., Dynamic bending and torsion behaviour of a cracked pump shaft, in *Proceedings of 7th IFToMM-Conference on Rotor Dynamics, Vienna, Austria* 2006; Paper-ID 166.

Bachschmid, N., and Tanzi, E., Non-Linear behaviours in cracked rotors, in *Proceedings of 7th IFToMM-Conference on Rotor Dynamics, Vienna, Austria* 2006; Paper-ID 167.

Bamnios, Y., Douka, E., and Trochidis, A., Crack identification in beam structures using mechanical impedance, *Journal of Sound and Vibration* 2002; 256(2), 287-297.

Barbieri, N., Novak, P. R., and Barbieri, R., Experimental identification of damping, *International Journal of Solids and Structures* 2004; 41, 3585−3594.

Barr, A. D. S., An extension of the Hu-Washizu variational principle in linear elasticity for dynamic problems. *Transactions of ASME Journal of Applied Mechanics* 1966; 33 (2), 465.

Benfratello, S., Cacciola, P., Impollonia, N., Masnata, A., and Muscolino, G., Numerical and experimental verification of a technique for locating a fatigue crack on beams vibrating under Gaussian excitation, *Engineering Fracture Mechanics* 2006; *In Press, Corrected Proof.*

Binici, B., Vibration of beams with multiple open cracks subjected to axial force, *Journal of Sound and Vibration* 2005; 287, 277-295.

Boltezar, M., Strancar, B., and Kuhelj, A., Identification of transverse crack location in flexural vibrations of free-free beams, *Journal of Sound and Vibration* 1998; 211(5), 729-734.

Borsaikia, A., Talukdar, S. and Dutta, A., Study of modal parameters and vibration signatures of notched concrete prisms, *Cement and Concrete Research* 2006; 36(3),592-598.

Bouaanani, N., Numerical investigation of the modal sensitivity of suspended cables with localized damage, *Journal of Sound and Vibration* 2006; 292, 1015-1030.

Cai, C. Q., and Shin, C. S., A normalized area-compliance method for monitoring surface crack development in a cylindrical rod, *International Journal of Fatigue* 2005; 27, 801-809.

Carneiro, S. H. S., and Inman, D. J., Continuous Model for the Transverse Vibration of Cracked Timoshenko Beams, *Transactions of the ASME, Journal of Vibration and Acoustics* 2002; 124, 310-320.

Chang, C-C., and Chen, L-W., Detection of the location and size of cracks in the multiple cracked beam by spatial wavelet based approach, *Mechanical Systems and Signal Processing* 2005; 19, 139–155.

Changhe, L., Bernasconi, O., and Xenophontidis, N., A generalized approach to the dynamics of cracked shafts, *ASME Journal of Vibration, Acoustics, Stress & Reliability in Design* 1989; 111, 257-263.

Chasalevris, A. C., and Papadopoulos, C. A., Identification of multiple cracks in beams under bending, *Mechanical Systems and Signal Processing* 2006; 20, 1631-1673.

Chasalevris, A. C., and Papadopoulos, C. A., Cross Coupled Bending Vibrations of Rotating Shaft due to a Transverse Breathing Crack, in *Proceedings of 7th IFToMM-Conference on Rotor Dynamics, Vienna, Austria* 2006; Paper-ID 247

Cheung, Y. K., and Leung, Y. T., *Finite element methods in dynamics*, Science press; 1991, 56-40.

Chinchalkar, S., Determination of crack location in beams using natural frequencies, *Journal of Sound and Vibration* 2001; 247(3), 417-429.

Chondros, T. G., Dimarogonas, A. D., and Yao, J., A consistent cracked bar vibration theory, *Journal of Sound and Vibration* 1997; 200(3), 303-313.

Chondros, T. G., Dimarogonas, A. D., and Yao, J., A continuous cracked beam vibration theory, *Journal of Sound and Vibration* 1998; 215(1), 17-34.

Chondros, T. G., Dimarogonas, A. D., and Yao, J., Longitudinal vibration of a continuous cracked bar, *Engineering Fracture Mechanics* 1998; 61, 593-606.

Chondros, T. G., Variational formulation of a rod under torsional vibration for crack identification, *Theoretical and Applied Fracture Mechanics* 2005; 44, 95-104.

Christides, S., and Barr, A. D. S., One-dimensional theory of cracked Bernoulli-Euler beams, *International Journal of Mechanical Sciences* 1984; 26(11-12), 639-648.

Clough, R. W. and Penzien, J., *Dynamics of Structures*, McGraw-Hill, Inc 1993.

Cuitino, L. A., and Saaverda, P. N., Crack detection and vibration behaviour of cracked beams, *Computers and structures* 2001; 79, 1451–1459.

Dado, M. H. F., and Abuzeid, O., Coupled transverse and axial vibratory behaviour of cracked beam with end mass and rotary inertia, *Journal of Sound and Vibration* 2003; 261, 675-696.

Darpe, A. K., Gupta, K., and Chawla, A., Dynamics of a two-crack rotor, *Journal of Sound and Vibration* 2003; 259(3), 649–675.

Darpe, A. K., Gupta, K., and Chawla, A., Experimental investigations of the response of a cracked rotor to periodic axial excitation, *Journal of Sound and Vibration* 2003; 260, 265-286.

Darpe, A. K., Gupta, K., and Chawla, A., Coupled bending, longitudinal and torsional vibrations of a cracked rotor, *Journal of Sound and Vibration* 2004; 269, 33–60.

Darpe, A. K., Gupta, K., and Chawla, A., Dynamics of a bowed rotor with a transverse surface crack, *Journal of Sound and Vibration* 2006; 296, 888-907.

Dharmaraju, N., Tiwari, R., and Talukdar, S., Identification of an open crack model in a beam based on force–response measurements, *Computers and Structures* 2004; 82, 167-179.

Dharmaraju, N., Tiwari, R., and Talukdar, S., Development of a novel hybrid reduction scheme for identification of an open crack model in a beam, *Mechanical Systems and Signal Processing* 2005; 19, 633-657.

Dharmaraju, N, and Sinha, J. K., Some comments on use of anti-resonance for crack identification in beams, *Journal of Sound and Vibration* 2005; 286, 669-671.

Di, W., and Law, S. S., Eigen-parameter decomposition of element matrices for structural damage detection *Engineering Structures* 2006; *In Press, Corrected Proof* .

Dilena, M., and Morassi, A., Identification of crack location in vibrating beams from changes in node positions, *Journal of Sound and Vibration* 2002; 255(5), 915-930.

Dilena, M., and Morassi, A., The use of anti-resonances for crack detection in beams, *Journal of Sound and Vibration* 2004; 276, 195-214.

Dilena, M., and Morassi, A., Damage detection in discrete vibrating systems, *Journal of Sound and Vibration* 2006; 289, 830-850.

Dimarogonas, A. D., and Massouros, G., Torsional vibration of a shaft with a circumferential crack, *Engineering Fracture Mechanics* 1981; 15(3-4), 439-444.

Dimarogonas, A. D., and Paipetis, S. A., *Analytical Methods in Rotor Dynamics*, Elsevier Applied science, London 1983.

Dimarogonas, A. D., Vibration of cracked structures: A state of the art review, *Engineering Fracture Mechanics* 1996; 55(5), 831-857.

Doebling, S. W., Farrar, C. R., and Prime, M. B., A summary review of vibration based damage identification methods, *Shock and Vibration Digest*, 1998; 30(2), 91-105.

Dong, G. M., Chen, J., and Zou, J., Parameter identification of a rotor with an open crack, *European Journal of Mechanics A/Solids* 2004; 23(2), 325-333.

Douka, E., Bamnios, G., and Trochidis, A., A method for determining the location and depth of cracks in double-cracked beams, *Applied Acoustics* 2004; 65, 997-1008.

Duffour, P., Morbidini, M. and Cawley, P., A study of the vibro-acoustic modulation technique for the detection of cracks in metals, *The Journal of the Acoustical Society of America* 2006; 119(3), 1463-1475.

Eshleman, R. L., and Eubanks, R. A., On the critical speeds of a continuous rotor, *ASME Journal of Engineering for Industry* 1969; 91(4B), 1180-1188.

Ewins, D. J., *Modal Testing: Theory, Practice and Application, 2nd edition,* Research Studies Press Ltd., Hertfordshire, 2000.

Fernandez-saez, J., and Navarro, C., Fundamental frequency of cracked beams in bending vibrations: an analytical approach, *Journal of Sound and Vibration* 2002; 256(1), 17-31.

Friswell, M. I., Garvey, S. D., and Penny, J. E. T., Model reduction using an iterated Improved Reduced System technique, *Fifth International Conference on Recent Advances in Structural Dynamics, UK* July 1994; 879-889.

Friswell, M. I., and Mottershead, J. E., *Finite Element Model Updating in Structural Dynamics*, Kluwer Academic Publishers, London, 1995.

Friswell, M. I., Penny, J. E. T., and Garvey, S. D., A combined genetic and eigen sensitivity algorithm for the location of damage in structures, *Computers and Structures* 1998; 69, 547-556.

Gasch, R., A survey of the dynamic behaviour of a simple rotating shaft with a transverse crack, *Journal of Sound and Vibration* 1993; 160(2), 313-332.

Goodwin, M. J., *Dynamics of rotor-bearing systems*, Unwin Hyman Publishers, London 1989.

Gómez-Mancilla, J., Sinou, J-J., Nosov, V. R., Thouverez, F., and Zambrano, A., The influence of crack-imbalance orientation and orbital evolution for an extended cracked Jeffcott rotor, *Comptes Rendus Mecanique* 2004; 332, 955-962.

Gounaris, G., and Dimarogonas, A. D., A finite element of a cracked prismatic beam in structural analysis, *Computers and Structures* 1988; 28(3), 309–13.

Gounaris, G. D., and Papadopoulos, C. A., Crack identification in rotating shafts by coupled response measurements, *Engineering Fracture Mechanics* 2002; 69, 339-352.

Green, I., and Casey, C., Crack Detection in a Rotor Dynamic System by Vibration Monitoring-Part I: Analysis, *Transactions of the ASME, Journal of Engineering for Gas turbines and Power* 2005; 127, 425-436.

Guyan, R. J., Reduction of stiffness and mass matrices, *AIAA Journal* 1965; 3 (2), 280.

Hadjileontiadis, L. J., Douka, E., and Trochidis, A., Fractal dimension analysis for crack identification in beam structures, *Mechanical Systems and Signal Processing* 2005; 19, 659-674.

Han, J-G., Ren, W-X., and Sun, Z-S., Wavelet packet based damage identification of beam structures, *International Journal of Solids and Structures* 2005; 42, 6610-6627.

He, Y., Guo, D. and Chu, F., Using genetic algorithms and finite element methods to detect shaft crack rotor-bearing system, *Mathematics and Computers in Simulation* 2001; 57, 95-108.

Henry, H., Hasnaoui, F., and Verrier, P., Crack detectability using on-line vibration level shift monitoring: application to horizontal axis power generation turbines, in *Proceedings of 7th IFToMM-Conference on Rotor Dynamics, Vienna, Austria* 2006; Paper-ID 265.

Hilbert, H. M., Hughes, T. J. R., and Taylor, R. L., Improved numerical dissipation for time integration algorithms in structural dynamics, *Earthquake Engineering and Structural Dynamics* 1977; **5,** 283-292.

Hu, H-C., On some variational principles in the theory of elasticity and plasticity, *Scientia Sinica* 1955; 4, 33-55.

Hu, J, and Liang, R. Y., An integrated approach to detection of cracks using vibration characteristics, *Journal of the Franklin Institute* 1993; 330(5), 841-53.

Huang, S. C., Huang, Y. M., and Shieh, S. M., Vibration and stability of a rotating shaft containing a transverse crack, *Journal of Sound Vibration* 1993; 162(3), 387–401.

Huynh, D., He, J., and Tran, D., Damage location vector: A non-destructive structural damage detection technique, *Computers and Structures* 2005; 83, 2353-2367.

Imam, I., Azzaro, S. H., Bankert, R. J., and Scheibel, J., Developement of an on-line rotor crack detection and monitoring system, *ASME Journal of Vibration, Acoustics, Stress & Reliability in Design* 1989; 111, 241-250.

Inagaki, T., Kanki, H. and Shiraki, K., Transverse vibrations of a general cracked rotor bearing system, *Journal of Mechanical design* 1981; 104, 1–11.

Inman, D. J., *Engineering Vibration*, Prentice-Hall, Inc, 2001.

Jain, J. R. and Kundra, T. K., Model based online diagnosis of unbalance and transverse fatigue crack in rotor systems, *Mechanics Research Communications* 2004; 31(5), 557-568.

Jaishia, B., and Ren, W-X., Damage detection by finite element model updating using modal flexibility residual, *Journal of Sound and Vibration* 2006; 290, 369-387.

Kane, K., and Torby, B. J., The extended modal reduction method applied to rotor dynamic problems, *Transactions of ASME, Journal of Vibration and Acoustics* 1991; 113 (1), 79–84.

Khiem, N. T., and Lien, T. V., A simplified method for natural frequency analysis of a multiple cracked beam, *Journal of Sound and Vibration* 2001; 245(4), 737-751.

Khiem, N. T., and Lien, T.V., Multi-crack detection for beam by the natural frequencies, *Journal of Sound and Vibration* 2004; 273, 175-184.

Kim, J. T., and Stubbs, N., Crack detection in beam-type structures using frequency data, *Journal of Sound and Vibration* 2003; 259(1), 145-160.

Kim, K. O., Perturbation method condensation of eigen problems, *AIAA Journal* 1998; 36(9), 1757-1760.

Kim, K. O., and Choi, Y. J., Energy method for selection of degrees of freedom in condensation, *AIAA Journal* 2000; 38(7), 1253-1259.

Kisa, M., Brandon, J., and Topcu, M., Free vibration analysis of cracked beams by a combination of finite elements and component mode synthesis methods, *Computers and Structures* 1998; 67, 215-223.

Kisa, M., and Gurel, M. A., Modal analysis of multi-cracked beams with circular cross section, *Engineering Fracture Mechanics* 2006; 73, 963-977.

Kishen, J. M. C., and Kumar, A., Finite element analysis for fracture behavior of cracked beam-columns, *Finite Elements in Analysis and Design* 2004; 40, 1773-1789.

Kou, K. P., and Burdekin, F. M., Stress intensity factors for a wide range of long-deep semi-elliptical surface cracks, partly through-wall cracks and fully through-wall

cracks in tubular members, *Engineering Fracture Mechanics* 2006; 73, 1693-1710.

Law, S. S., and Lu, Z. R., Crack identification in beam from dynamic responses, *Journal of Sound and Vibration* 2005; 285, 967-987.

Le, K. N., Time-frequency distributions for crack detection in rotors-A fundamental note *Journal of Sound and Vibration* 2006; 294, 397-409.

Lee, C. W., Yun, J. S., and Jun, O. S., Modeling of a simple rotor with switching crack and its experimental verifications, *Transactions of ASME, Journal of Vibration and Acoustics* 1992; 114, 217-225.

Lee, C. W., and Kwon, K. S., Crack detection in rotating machinery by modal testing, *Institution of Mechanical Engineers* 2000; C576/031, 535-543.

Lee, Y-S., and Chung, M-J., A study on crack detection using eigen frequency test data, *Computers and Structures* 2000; 77, 327-342.

Lei, X., Zhang, G., Chen, J., Xigeng, S., and Dong, G., Simulation on the motion of crankshaft with a slant crack in crankpin, *Mechanical Systems and Signal Processing,* 2007; 21(1), 502-513.

Li, B., Chen, X. F., Ma, J. X., and He, Z. J., Detection of crack location and size in structures using wavelet finite element methods, *Journal of Sound and Vibration* 2005; 285, 767-782.

Liebowitz, H., Vanderveldt, H., and Harris, D. W., Carrying capacity of notched columns, *International Journal of Solids & Structures* 1967; 3(4), 489-500.

Liebowitz, H., and Claus, W. D., Failure of notched columns, *Engineering Fracture Mechanics* 1968; 1(2), 379-383.

Liu, J. K., and Yang, Q. W., A new structural damage identification method, *Journal of Sound and Vibration* 2006; 297, 694-703.

Loya, J. A., Rubio, L., and Fernandez-Saez, J., Natural frequencies for bending vibrations of Timoshenko cracked beams, *Journal of Sound and Vibration* 2006; 290, 640-653.

Maia, N. M. M., and Silva, J. M. M., (Eds.), Theoretical and Experimental Modal Analysis, *Engineering Dynamics Series, Research Studies Press Ltd., Hertfordshire,* 1997.

Mani, G., Quinn, D. D., and Kasarda, M., Active health monitoring in a rotating cracked shaft using active magnetic bearings as force actuators, *Journal of Sound and Vibration* 2006; 294, 454-465.

Mayes, I. W., and Davies, W. G. R., Analysis of the Response of a Multi-Rotor-Bearing System Containing a Transverse Crack in a Rotor, *Transactions of ASME Journal of Vibration, Acoustics, Stress & Reliability in Design*, 1984, 106, 139–145.

Meng, G., and Gasch, R., Stability and stability degree of a cracked flexible rotor supported on journal bearings, *Transactions of the ASME, Journal of Vibration and Acoustics* 2000; 122, 116-125.

Mei, C., Karpenko, Y., Moody, S., and Allen, D., Analytical approach to free and forced vibrations of axially loaded cracked Timoshenko beams, *Journal of Sound and Vibration* 2006; 291, 1041-1060.

Meirovitch, L., *Elements of vibration analysis*, McGraw-Hill Book Company, 1986.

Morassi, A., Crack-Induced changes in eigen parameters of beam structures, *Journal of Engg. Mech. ASCE* 1993; 119 (9), 1798-1803.

Murphy, K. D., and Zhang, Y., Vibration and stability of a cracked translating beam, *Journal of Sound and Vibration* 2000; 237(2), 319-335.

Musil, M., Localization and quantification of breathing crack, *Transactions of the ASME, Journal of Dynamic Systems, Measurement and Control*, 2006; 128, 458-462.

Nahvi, H. and Jabbari, M., Crack detection in beams using experimental modal data and finite element model, *International Journal of Mechanical Sciences* 2005; 47, 1477-1497.

Narkis, Y., and Elmalah, E., Crack identification in a cantilever beam under uncertain end conditions, *International Journal of Mechanical Sciences* 1996; 38(5), 499-507.

Nelson, H. D., A finite rotating shaft element using Timoshenko beam theory, *Engineering research center report ERC-R*-77023 1977, Sept., Arizona state university.

Nelson, H. D., and Nataraj, C., The dynamics of a rotor system with a cracked shaft, *Transactions of ASME Journal of Vibration, Acoustics, Stress & Reliability in Design* 1986; 108, 189-196.

Ngwangwa, H. M., Heyns. P. S., and Tonder, F. V., Assessment of structural damage using operational time responses and finite element simulation, *Journal of Sound and Vibration* 2006; 296, 23–45.

O'Callahan, J., A procedure for an improved reduced system (IRS) model, *Seventh International Modal Analysis Conference, Las Vegas* January 1989; 17-21.

Okamura, H., A cracked column under compression, *Engineering Fracture Mechanics* 1969; 1(3), 547.

Owolabi, G. M., Swamidas, A. S. J., and Seshadri, R., Crack detection in beams using changes in frequencies and amplitudes of frequency response functions, *Journal of Sound and Vibration* 2003; 265, 1-22.

Papadopoulos, C. A., and Dimarogonas, A. D., Coupling of bending and torsional vibration of a cracked Timoshenko shaft, *Ingenieur Archive* 1987; 57, 495–505.

Papadopoulos, C. A., and Dimarogonas, A. D., Coupled longitudinal and bending vibration of rotating shaft with an open crack, *Journal of Sound Vibration* 1987; 117, 81–93.

Papadopoulos, C. A., and Dimarogonas, A. D., Coupled longitudinal and bending vibrations of a cracked shaft, *Transactions of ASME Journal of Vibration, Acoustics, Stress & Reliability in Design* 1988; 110, 1-8.

Patil, D. P., and Maiti, S. K., Detection of multiple cracks using frequency measurements, *Engineering Fracture Mechanics* 2003; 70, 1553-1572.

Patil, D. P., and Maiti, S. K., Experimental verification of a method of detection of multiple cracks in beams based on frequency measurements, *Journal of Sound and Vibration* 2005; 281, 439–451.

Paz, M., Dynamic condensation, *AIAA Journal* 1984; 22 (5), 724-727.

Pennacchi, P., Bachschmid, N., and Vania, A., A model-based identification method of transverse cracks in rotating shafts suitable for industrial machines, *Mechanical Systems and Signal Processing* 2006; 20, 2112-2147.

Pu, Y. P., Chen, J., Zou, J., and Zhong, P., Quasi-periodic vibration of cracked rotor on flexible bearings, *Journal of Sound and Vibration* 2002; 251(5), 875-890.

Qian, G. L., Gu, S. N., and Jiang, J. S., The dynamic behaviour and crack detection of al beam with a crack, *Journal of Sound Vibration* 1990; 138, 233–243.

Raath, A. D., Structural dynamic response reconstruction in the time domain, *PhD Thesis, University of Pretoria* 1992.

Rajab, M. D., and Al-Sabeeh, Vibrational characteristics of cracked shafts, *Journal of Sound Vibration* 1991; 147, 465–473.

Rao, J. S., *Advanced Theory of Vibration*, Wiely Eastern Ltd. 1992.

Rao, J. S., *Rotor Dynamics*, New Age International Ltd., Publishers, 3rd ed. 1996.

Rizos, P., Aspragathos, N., and Dimarogonas, A. D., Identification of crack location and magnitude in a cantilever beam from the vibration modes, *Journal of Sound Vibration* 1990; 138, 381–388.

Rucka, M., and Wilde, K., Crack identification using wavelets on experimental static deflection profiles, *Engineering Structures* 2006; 28, 279-288.

Ruotolo, R., and Surace, C., Damage assessment of multiple cracked beams: numerical results and experimental validation, *Journal of Sound and Vibration* 1997; 206(4), 567-588.

Ruotolo, R., and Surace, C., Natural frequencies of a bar with multiple cracks, *Journal of Sound and Vibration* 2004; 272, 301-316.

Rytter, A., Vibration based inspection of civil engineering structures, *Ph. D. Dissertation, Department of Building Technology and Structural Engineering* 1993; Aalborg University, Denmark.

Saavedra, P. N., and Cuitiño, L. A., Crack detection and vibration behavior of cracked beams, *Computers & Structures* 2001; 79(16), 1451-1459.

Sabnavis, G., Kirk, R. G., Kasarda, M., and Quinn, D., Cracked shaft detection and diagnostics: A literature review, *Shock and Vibration Digest* 2004, 36(4), 287-296.

Salawu, O. S., Detection of structural damage through changes infrequencies: A review, *Engineering Structures* 1997; 19(9), 718-723.

Sekhar, A. S., and Prabhu, B. S., Crack detection and vibration characteristics of cracked shafts, *Journal of Sound and Vibration* 1992; 157(2), 375-381.

Sekhar, A. S., and Prasad, P. B., Dynamic analysis of a rotor system considering a slant crack in the shaft, *Journal of Sound and Vibration* 1997; 208(3), 457-474.

Sekhar, A. S., Vibration characteristics of a cracked rotor with two open cracks, *Journal of sound and vibration* 1999; 222(3), 409-423.

Sekhar, A. S., Crack identification in a rotor system: a model-based approach**,** *Journal of Sound and Vibration* 2004; 270(4-5), 887-902.

Sekhar, A. S., Model-based identification of two cracks in a rotor system, *Mechanical Systems and Signal Processing* 2004; 18(4), 977-983.

Sekhar, A. S., Detection and Monitoring of Cracks in a Coast-Down Rotor Supported on Fluid Film Bearings, *Tribology International* 2004; 37(3), 279–287.

Sekhar, A. S., Mohanty, A. R., and Prabhakar, S., Vibrations of cracked rotor system: transverse crack versus slant crack, *Journal of Sound and Vibration* 2005; 279, 1203-1217.

Shames, I. H., and Dym, C. L., *Energy and Finite Element Methods in Structural Mechanics*, New Age International Publishers Ltd., 1st ed. 1995.

Shen, M. H. H., and Pierre, C., Natural Modes of Bernoulli-Euler beams with symmetric crack, *Journal of Sound and Vibration* 1990; 138(1), 115-134.

Shifrin, E. I., and Ruotolo, R., Natural frequencies of a beam with an arbitrary number of cracks, *Journal of Sound and Vibration* 1999; 222(3), 409-423.

Shull, P. J., *Nondestructive evaluation - Theory, techniques, and applications*, Marcel Dekker, Inc., Newyork 2002.

Sinha, J. K., Friswell, M. I., and Edwards, S., Simplified models for the location of cracks in beam structures using measured vibration data, *Journal of Sound and Vibration* 2002; 251(1), 13-38.

Sinou, J-J., and Lees, A. W., The influence of cracks in rotating shafts, *Journal of Sound and Vibration* 2005; 285, 1015-1037.

Sinou, J-J., Lees, and A.W., A non-linear study of a cracked rotor, *European Journal of Mechanics A/Solids* 2007; 26, 152-170.

Solbeck, J. A., and Ray, L. R., Damage identification using sensitivity-enhancing control and identified models, *Transactions of the ASME, Journal of Vibration and Acoustics* 2006; 128, 210-220.

Stanbridge, A. B., and Ewins, D. J., Modal testing using a scanning laser Doppler vibrometer, *Mechanical Systems and Signal Processing* 1999; 13(2), 255-270.

Stoisser, C. M., Hasnaoui, F., and Henry, H., The resonance frequency shift in cracked rotors: numerical and experimental results, in *Proceedings of 7th IFToMM-Conference on Rotor Dynamics, Vienna, Austria* 2006; Paper-ID 266.

Suarez, L. E., and Singh, M. P., Dynamic condensation method for structural eigen value analysis, *AIAA Journal* 1992; 30(4), 1046-1054.

Sukumar, N., and Moes, N., Morn, B., and Belytschko, T., Extended finite element method for three-dimensional crack modeling, *International Journal for Numerical methods in Engineering* 2000; 48(11), 1549–1570.

Suresh, S., Omkar, S. N., Ganguli, R., and Mani, V., Identification of crack location and depth in a cantilever beam using a modular neural network approach, *Institute of Physics Publishing, Smart Materials and Structures* 2004; 13, 907-915.

Szolc, T., Bednarek, T., Marczewska, I., Marczewski, A., and Sosnowski, W., Fatigue analysis of the cracked rotor by means of the one- and three dimensional dynamical model, in *Proceedings of 7th IFToMM-Conference on Rotor Dynamics, Vienna, Austria* 2006; Paper-ID 241.

Tada, H., Paris, P. C., and Irwin, G. R., *The Stress Analysis of Cracks Handbook. 3rd ed*., New York: ASME 2000.

Tikhonov, A. N., and Arsenin, V. Y., *Solutions of Ill-Posed Problems*, Winston & Sons, Washington, D.C. 1977.

Tiwari, R., and Dharmaraju, N., Development of a condensation scheme for transverse rotational degrees of freedom elimination in identification of beam crack parameters, *Mechanical Systems and Signal Processing* 2006; 20(8), 2148-2170.

Tsai, T. C., and Wang, Y. Z., The vibration of a multi-crack rotor, *International Journal of Mechanical Sciences* 1997; 39(9), 1037-1053.

Viola, E., Federisi, L., and Nobile, L., Detection of crack location by cracked beam element method for structural analysis, *Theoretical and Applied Fracture Mechanics* 2001; 36, 23-35.

Vyas, N. S. and Satishkumar, D., Artificial neural network design for fault identification in a rotor-bearing system, *Mechanism and Machine Theory* 2001; 36, 157-175.

Wang, K., Inman, D. J., and Farrar, C. R., Modeling and analysis of a cracked composite cantilever beam vibrating in coupled bending and torsion, *Journal of Sound and Vibration* 2005; 284, 23-49.

Wauer, J., On the dynamics of cracked rotors: A literature survey, *Applied Mechanics Review* 1990; 43(1), 13–6.

Yang, B., Suh, C. S., and Chan, A. K., Characterization and Detection of Crack-induced Rotary Instability, *Transactions of the ASME, Journal of Vibration and Acoustics* 2002; 124, 40-48.

Yang, B., and Suh, C. S., Interpretation of crack-induced rotor non-linear response using instantaneous frequency, *Mechanical Systems and Signal Processing* 2004;18, 491-513.

Yang, Q. W., and Liu, J. K., A coupled method for structural damage identification, *Journal of Sound and Vibration* 2006; 296, 401-405.

Yang, X. F., Swamidas, A. S. J., and Seshadri, R., Crack identification in vibrating beams using the energy method, *Journal of Sound and Vibration* 2001; 244(2), 339-357.

Yokoyama, T., and Chen, M. C., Vibration analysis of edge-cracked beams using a line-spring model *Engineering Fracture Mechanics* 1998; 59(3), 403-409.

Yoon, H-I., and Son, I-S., Dynamic behavior of cracked simply supported pipe conveying fluid with moving mass, *Journal of Sound and Vibration* 2006; 292, 941-953.

Zheng, D. Y., and Fan, S. C., Natural frequency changes of a cracked Timoshenko beam by modified fourier series, *Journal of Sound and Vibration* 2001; 246(2), 297-317.

Zheng, D. Y. and Kessissoglou, N. J., Free vibration analysis of a cracked beam by finite element method, *Journal of Sound and Vibration* 2004; 273(3), 457-475.

Zou, J., and Chen, J., A comparative study on time-frequency feature of cracked rotor by Wigner-Ville distribution and wavelet transform, *Journal of Sound and Vibration* 2004; 276 (1-2), 1-11.

Zhou, T., Xu, J., and Sun, Z., Dynamic Analysis and Diagnosis of a Cracked Rotor, *Transactions of the ASME, Journal of Vibration and Acoustics* 2001; 123, 4, 539–543.

Zhou, T., Sun, Z., Xu, J., and Han, W., Experimental analysis of cracked rotor, *Transactions of the ASME, Journal of Dynamic Systems, Measurement and Control*, 2005; 127, 313-320.

Zhua, C., Robb, D. A., and Ewins, D. J., The dynamics of a cracked rotor with an active magnetic bearing, *Journal of Sound and Vibration* 2003; 265, 469-487.

Zimmerman, D. C., and Kaouk, M., Structural damage detection using a minimum rank update theory, *Transactions of the ASME*, *Journal of Vibration and Acoustics* 1994; 116 (2), 222–231.

LIST OF PUBLICATION

In Journals

[1] Karthikeyan, M., Tiwari, R., and Talukdar, S., Development of a technique to locate and quantify a beam crack based on modal parameters, *Transactions of ASME, Journal of Vibration and Acoustics* 2007; 129(3), 390-395.

[2] Karthikeyan, M., Tiwari, R., and Talukdar, S., Crack localization and sizing in a beam based on the free and forced response measurements, *Mechanical Systems and Signal Processing* 2007; 21(3), 1362-1385.

[3] Karthikeyan, M., Tiwari, R., and Talukdar, S., Development of a novel algorithm for a crack detection, localization and sizing in a beam based on forced response measurements, *Transactions of ASME, Journal of Vibration and Acoustics 2008*, 130(Published Online).

[4] Karthikeyan, M., Tiwari, R., and Talukdar, S., Experimental investigation of the algorithm for detection, localization and sizing of a flaw in a beam based on forced response measurements, *Journal of Sound and Vibration* (under review).

In Conference

[1] Karthikeyan, M., Tiwari, R., and Talukdar, S., Identification of crack model parameters in a beam from modal parameters, in *Proceedings of the Twelfth National Conference on Machines and Mechanisms, IIT Guwahati, India* 2005; 202-207.